

# Low-dimensional modelling and control of separated shear flows



Dirk Martin Luchtenburg

Department of Process Engineering

Berlin Institute of Technology

A thesis submitted for the degree of

*Doktor der Ingenieurwissenschaften*

Degree date: July 12, 2010

# **Low-dimensional modelling and control of separated shear flows**

vorgelegt von

**Dirk Martin Luchtenburg**

Von der Fakultät III – Prozesswissenschaften  
der Technischen Universität Berlin  
zur Erlangung des akademischen Grades  
Doktor der Ingenieurwissenschaften  
genehmigte Dissertation

Promotionsausschuss:

Vorsitzender: Prof. Dr.-Ing. Felix Ziegler  
Berichter: Prof. Dr.-Ing. Rudibert King  
Dr. rer. nat. Bernd R. Noack

Tag der wissenschaftliche Aussprache: 12.07.2010

Berlin 2010  
D 83

# Abstract

This thesis involves the modelling and control of separated shear flows. The emphasis is on the development of low-dimensional mean-field models that capture essential flow physics and are suitable for non-linear control design in simulation and experiment.

The concept of the mean-field model by [Noack \*et al.\* \(2003\)](#) has been generalized to include actuation mechanisms, which are incommensurable with the dominant frequency of the natural flow. This model describes how actuation-induced oscillations can interact with (and suppress) the instability at the natural frequency, only by indirect interaction via the varying mean flow.

The framework of mean-field modelling has been applied to three different configurations: the flow around a 2-D circular cylinder, the flow around a 2-D high-lift configuration, and the flow around a D-shaped body. The first two configurations are investigated in numerical simulations, whereas the latter is a windtunnel experiment.

For the circular cylinder, a parameterized proper orthogonal decomposition approach (POD) is used to extend the dynamic range of the standard POD. This parameterized model is used to optimize sensor locations. The model is demonstrated in a closed-loop control that targets wake suppression.

High frequency open-loop actuation can significantly reduce the separation that is caused by large flap angles of a high-lift configuration. The essence of this mechanism is captured by the generalized mean-field model. This model is used for a set-point control of the lift coefficient.

Finally, the generalized mean-field model is adapted for design of a nonlinear controller for set-point tracking of the base pressure coefficient of a bluff body. This illustrates the usefulness of mean-field models in experiment.

## Publications

Parts of this work have appeared previously:

- LUCHTENBURG, D.M., ALEKSIĆ, K., SCHLEGEL M., NOACK, B.R., KING, R., TADMOR, G., GÜNTHER, B. & THIELE, F. (2010). Turbulence control based on reduced-order models and nonlinear control design. In R. King, eds., *Active Flow Control II, Notes on Numerical Fluid Mechanics and Multidisciplinary Design*, 341–356, Springer.
- ALEKSIĆ, K., LUCHTENBURG, D.M., KING, R., NOACK, B.R. & PFEIFFER, J. (2010). Robust nonlinear control versus linear model predictive control of a bluff body wake. *AIAA Paper* 2010-4833.
- FREDERICH, O., SCOUTEN, J., LUCHTENBURG, D.M. & THIELE, F. (2009). Numerical simulation and analysis of the flow around a wall-mounted finite cylinder. In W. Nitsche & C. Dobriloff, eds., *Imaging Measurement Methods for Flow Analysis*, vol. 106 of *Notes on Numerical Fluid Mechanics and Multidisciplinary Design*, 207–216, Springer.
- FREDERICH O., SCOUTEN J., LUCHTENBURG D.M. & THIELE F. (2009). Large-scale dynamics in the flow around a finite cylinder with ground plate. In *Proceeding of the 6th International Symposium on Turbulence and Shear Flow Phenomena (TSFP-6)*.
- LACARELLE, A., FAUSTMANN, T., GREENBLATT, T., PASCHEREIT, C.O., LEHMANN, O., LUCHTENBURG, D.M. & NOACK, B.R. (2009). Spatio-temporal characterization of a conical swirler

flow field under strong forcing. *J. Eng. Gas Turbines Power*, **131**.

- LUCHTENBURG, D.M., GÜNTHER, B., NOACK, B.R., KING, R. & TADMOR, G. (2009). A generalized mean-field model of the natural and high-frequency actuated flow around a high-lift configuration. *J. Fluid Mech.*, **623**, 283–316.
- LUCHTENBURG, D.M., NOACK, B.R. & SCHLEGEL, M. (2009). An introduction to the POD Galerkin method for fluid flows with analytical examples and MATLAB source codes. Tech. Rep. 01/2009, Berlin Institute of Technology, Department for Fluid Dynamics and Engineering Acoustics, Chair in Reduced-Order Modelling for Flow Control.
- SCHLEGEL, M., NOACK, B.R., COMTE, P., KOLOMSKIY, D., SCHNEIDER, K., FARGE, M., SCOUTEN, J., LUCHTENBURG, D.M. & TADMOR, G. (2009). Reduced-order modelling of turbulent jets for noise control. In C. Brun, D. Juve, M. Manhart & C.D. Munz, eds., *Numerical Simulation of Turbulent Flows and Noise Generation*, vol. 104 of *Notes on Numerical Fluid Mechanics and Multidisciplinary Design*, 3–27, Springer.
- FREDERICH, O., SCOUTEN, J., LUCHTENBURG, D.M., THIELE, F., JENSCH, M., HÜTTMANN, F., BREDE, M. & LEDER, A. (2008). Joint numerical and experimental investigation of the flow around a finite wall-mounted cylinder at a Reynolds number of 200,000. In *Proceedings of the ERCOFTAC International Symposium on Engineering Turbulence Modelling and Measurements (ETMM7)*, 517–52.
- LACARELLE, A., LUCHTENBURG, D.M., BOTHIEN, M.R., PASCHEREIT, C.O. & NOACK, B.R. (2008). A combination of image post-processing tools to identify coherent structures of premixed flames. In *Proceedings of the 2nd International Conference on Jets, Wakes and Separated Flows (ICJWSF)*, (submitted to AIAA Journal).

- LUCHTENBURG, D.M., VITRAC, B. & ZENGL, M. (2008). Model reduction methods for flow control. In *ERCRAFT Bulletin 77, selected report of the 2nd Young ERCRAFT Workshop*, 21–25.
- FREDERICH, O., LUCHTENBURG, D.M., WASSEN, E. & THIELE, F. (2007). Analysis of the unsteady flow around a wall-mounted finite cylinder at  $Re=200,000$ . In J.M.L.M. Palma & A.S. Lopes, eds., *Advances in Turbulence XI*, vol. 117 of *Proceedings in Physics*, 85–87, Springer.
- FREDERICH, O., SCOUTEN, J., LUCHTENBURG, D.M. & THIELE, F. (2007). Database variation and structure identification via POD of the flow around a wall-mounted finite cylinder. In *Proceedings of 5th Conference on Bluff Body Wakes and Vortex Induced Vibrations (BBVIV5)*, 185–188.
- LEHMANN, O., LUCHTENBURG, D.M. & LOSSE, N. (2007). Calibration of model coefficients using the adjoint formulation. Tech. rep., 1st Young Ercraft Workshop, Montestigliano, Italy, March 26–30.
- TADMOR, G., CENTUORI, M.D., LUCHTENBURG, D.M., LEHMANN, O., NOACK, B.R. & MORZYŃSKI, M. (2007). Low order Galerkin models for the actuated flow around 2-D airfoils. *AIAA Paper* 2007–1313.
- LUCHTENBURG, D.M., TADMOR, G., LEHMANN, O., NOACK, B.R., KING, R. & MORZYŃSKI, M. (2006). Tuned POD Galerkin models for transient feedback regulation of the cylinder wake. *AIAA Paper* 2006–1407.
- LEHMANN, O., LUCHTENBURG, D.M., NOACK, B.R., KING, R., MORZYŃSKI, M. & TADMOR, G. (2005). Wake stabilization using POD Galerkin models with interpolated modes. In *Proceedings of 44th IEEE Conference on Decision and Control and European Control Conference (CDC-ECC)*, 500–505.

## Acknowledgements

This work summarizes a part of my research which was performed at the Technische Universität Berlin in the context of the collaborative research center SFB 557 financed by the German research foundation (DFG). The project that I worked on, was titled “Low-dimensional modelling and control of free and wall-bounded shear flows (generalization for complex geometries)”. I would like to thank all people who have contributed to my research and this thesis.

My advisor, Dr. Bernd Noack, contributed significantly to my knowledge of modelling of fluid flows during lectures and countless invitations to good restaurants! His best practices guided me while doing research and in writing publications. My supervisor, Prof. R. King, provided me with a good working environment as speaker of the collaborative research center. I thank him for his helpful comments and review of my research. Thanks to Prof. Gilead Tadmor for my stay at Northeastern University in 2005. In particular, I thank him for helping me with control theory, mathematics and writing publications.

Thanks to all colleagues in the “C5” reduced-order modelling for flow control group, the department of plant and process technology, computational fluid dynamics and aeroacoustics group and all other colleagues in the collaborative research center. Thanks to Bert Günther for the URANS simulations of the high-lift configuration; Oliver Lehmann for our mutual work on the circular cylinder wake; Prof. Marek Morzyński for his UNS3 code to simulate the cylinder wake flow; to Katarina Aleksić for designing nonlinear controllers based on mean-field models, which lead to successful implementation in numerical simulation and experiment; to Arnaud Lacarelle



and Prof. O. Paschereit for many interesting measurements of the burner configuration; to Martin Hecklau and Prof. W. Nitsche for time-resolved PIV measurements of the bluff body. I also like to thank Octavian Frederich for his interest in low-dimensional modelling and the fruitful application to his LES simulation data.

Finally I like to thank my colleague Dr. Michael Schlegel who contributed to my knowledge through lectures and by answering a lot of my questions; my office mate, Jon Scouten, for listening and continuously sharing new research ideas. Thanks to the system administrators Martin Franke and Lars Oergel who always helped out with computer trouble. I thank Steffi Stehr for taking care of all the administrivia. Last but not least I like to thank my family and friends who supported me through this time.

# Contents

<b>1</b>	<b>Introduction</b>	<b>1</b>
1.1	Motivation . . . . .	1
1.2	Active flow control . . . . .	2
1.3	Model reduction . . . . .	3
1.4	Outline . . . . .	4
<b>2</b>	<b>Reduced-order models and control</b>	<b>7</b>
2.1	Fluid flow model . . . . .	8
2.1.1	Basic equations of fluid dynamics . . . . .	8
2.1.2	Reynolds-averaged Navier-Stokes equation . . . . .	9
2.1.3	Transient behaviour and mean flow distortion . . . . .	11
2.2	Model reduction for fluid flows . . . . .	12
2.2.1	Proper orthogonal decomposition . . . . .	13
2.2.2	Dynamic mode decomposition . . . . .	18
2.2.3	Galerkin method . . . . .	20
2.2.4	Implementation of actuation . . . . .	21
2.3	Mean-field modelling . . . . .	24
2.3.1	Weakly nonlinear oscillator . . . . .	25
2.3.2	Mean-field model for single frequency . . . . .	28
2.3.3	Mean-field model for two frequencies . . . . .	34
2.3.4	Mean-field Galerkin model for two frequencies . . . . .	41
2.4	Control design . . . . .	43
2.4.1	Sliding mode control . . . . .	44

<b>3</b>	<b>Stabilization of the circular cylinder wake</b>	<b>46</b>
3.1	Abstract . . . . .	46
3.2	Introduction . . . . .	47
3.3	Numerical simulation . . . . .	48
3.3.1	Configuration . . . . .	48
3.3.2	Simulation . . . . .	49
3.4	Actuation strategy . . . . .	49
3.4.1	Physically motivated control . . . . .	50
3.4.2	Control design with a mean-field model . . . . .	50
3.5	Parameterized POD . . . . .	52
3.5.1	Motivation . . . . .	52
3.5.2	Collection of mode sets . . . . .	53
3.5.3	Full information control . . . . .	54
3.6	SISO control with parameterized POD . . . . .	57
3.6.1	Observer design . . . . .	58
3.6.2	A parameterized POD based look-up table . . . . .	61
3.6.3	Sensor optimization . . . . .	62
3.6.4	Results . . . . .	64
3.7	Conclusions . . . . .	66
<b>4</b>	<b>Separation control of the flow around a high-lift configuration</b>	<b>70</b>
4.1	Abstract . . . . .	70
4.2	Introduction . . . . .	70
4.3	Numerical simulation . . . . .	72
4.3.1	Configuration . . . . .	72
4.3.2	Unsteady Reynolds-averaged Navier-Stokes simulation . . . . .	74
4.3.3	Natural and periodically forced flow . . . . .	74
4.4	Phenomenological modelling . . . . .	75
4.5	Mean-field Galerkin model . . . . .	79
4.5.1	Simplification of the dynamical system . . . . .	84
4.5.2	Parameter identification . . . . .	86
4.6	Comparison of the Galerkin model with the URANS simulation . . . . .	87
4.6.1	Galerkin approximation of the transient simulation . . . . .	87

4.6.2	Least-order Galerkin model of the transient data . . . . .	88
4.6.3	Estimation of the lift coefficient . . . . .	91
4.6.4	Lift formula . . . . .	93
4.7	Set-point tracking of the lift coefficient . . . . .	96
4.8	Discussion . . . . .	98
4.8.1	Turbulence effects . . . . .	98
4.8.2	Non-equilibrium effects . . . . .	101
4.9	Conclusions . . . . .	101
<b>5</b>	<b>Stabilization of a bluff body wake</b>	<b>103</b>
5.1	Abstract . . . . .	103
5.2	Introduction . . . . .	103
5.3	Experimental setup . . . . .	105
5.4	Characterization of the flow field . . . . .	107
5.4.1	Natural flow . . . . .	107
5.4.2	Periodically forced flow . . . . .	110
5.5	A mean-field Galerkin model . . . . .	111
5.5.1	Amplitude model . . . . .	111
5.5.2	Conditions for the model coefficients . . . . .	114
5.5.3	Implementation of actuation . . . . .	115
5.6	Experimental results . . . . .	117
5.6.1	Model parameter identification . . . . .	117
5.6.2	Set-point tracking of base-pressure coefficient . . . . .	118
5.7	Conclusions . . . . .	121
<b>6</b>	<b>Conclusions</b>	<b>124</b>
<b>A</b>	<b>Proper Orthogonal Decomposition</b>	<b>127</b>
A.1	POD in the spatial domain . . . . .	127
A.2	POD in the temporal domain . . . . .	131
A.3	POD and its connection to SVD . . . . .	132

<b>B Window filters and structure of the Galerkin system</b>	<b>135</b>
B.1 Window filters . . . . .	135
B.2 Structure of the mean-field Galerkin model . . . . .	138
<b>References</b>	<b>150</b>

# List of Figures

2.1	Illustration of the method of averaging to the van der Pol equation	29
2.2	Polar representation and phase portrait of a mean-field model . .	34
2.3	Principle sketch of the generalized mean-field model . . . . .	40
3.1	Principal sketch of the actuated cylinder wake . . . . .	49
3.2	Comparison of the streamlines of a natural, moderately and ag- gressively forced flow field . . . . .	53
3.3	Parameterized POD: phase portrait of the mode amplitudes . . .	55
3.4	Orientation of the volume force . . . . .	55
3.5	Parametrization of the operating condition . . . . .	59
3.6	A sensed velocity trajectory and its dynamic estimate . . . . .	60
3.7	The estimated frequency and amplitude of a velocity signal . . . .	60
3.8	Performance of an optimal sensor . . . . .	64
3.9	Optimized sensor locations . . . . .	65
3.10	The phase difference between a sensor signal and the ideal actua- tion signal . . . . .	67
3.11	Actuation signal of a successful controller . . . . .	67
3.12	The elongation of the recirculation length for two successful simu- lations . . . . .	68
3.13	Illustration of the gain / phase problem . . . . .	68
3.14	A ‘ringing’ recirculation length . . . . .	69
4.1	Sketch of the high-lift configuration . . . . .	73
4.2	Comparison of a natural and actuated flow field . . . . .	76
4.3	Solution of a mean-field model problem . . . . .	78

## LIST OF FIGURES

---

4.4	Amplitude and lift dynamics for a transient . . . . .	79
4.5	The relation between the steady solution, the natural and actuated mean flows . . . . .	81
4.6	Principal sketch of the dynamics of the natural and actuated flow around a high-lift configuration . . . . .	83
4.7	The shift-mode amplitude obtained from projection . . . . .	88
4.8	Phase portraits of the URANS simulation and the least-order Galerkin model . . . . .	89
4.9	Comparison of the oscillation amplitudes of the URANS data and the least-order Galerkin model . . . . .	91
4.10	Phase portrait of the forced dynamics . . . . .	92
4.11	Comparison of the original and reconstructed lift coefficient . . . .	94
4.12	Comparison of the URANS, modal, and identified lift coefficient .	95
4.13	Evolution of the time-averaged lift coefficient under high-frequency actuation . . . . .	97
4.14	Reference tracking test of the lift-coefficient . . . . .	99
5.1	A sketch of the experimental setup with the D-shaped body . . .	105
5.2	Fluctuation pressure coefficients of a sensor at the upper- and lower edge; natural flow, $Re = 46\,000$ , and the spectrum of the lower sensor	108
5.3	DMD analysis of PIV snapshots of the natural flow field at $Re = 46\,000$ . . . . .	109
5.4	The time-averaged natural and in phase actuated flow at $Re = 46\,000$ ; $St^a = 0.15$ . . . . .	110
5.5	Fluctuation pressure coefficients of a sensor at the upper- and lower edge; actuated flow, $Re = 46\,000$ , $St^a = 0.15$ , and the spectrum of the lower sensor . . . . .	111
5.6	DMD analysis of PIV snapshots of the in phase actuated flow field at $Re = 46\,000$ ; $St^a = 0.15$ . . . . .	112
5.7	The relation between the loudspeaker voltage and the excitation momentum coefficient . . . . .	116
5.8	Stepwise increments of the actuation amplitude at $Re = 46\,000$ : loudspeaker voltage and base pressure coefficient . . . . .	116

## LIST OF FIGURES

---

5.9	The static relationship between the loudspeaker voltage and the base pressure coefficient, and the relation to the actuation input to the amplitude model . . . . .	117
5.10	The oscillation amplitudes of the model and the time-averaged base pressure coefficients as identified by the model . . . . .	118
5.11	Reference tracking test of the sliding mode controller; $Re = 46\,800$ , $St^a = 0.15$ . . . . .	120
5.12	Reference tracking test of the sliding mode controller under a changing Reynolds number; $Re = 46\,800$ , $St^a = 0.15$ . . . . .	122



# List of Tables

2.1	Derivation of the Galerkin system . . . . .	22
2.2	Derivation of the terms for the generalized Galerkin mean-field model	42
3.1	Quantities that highlight the differences between standard and in- terpolated models . . . . .	57
4.1	Identified parameters for the generalized mean-field model (1) . .	90
4.2	Identified parameters of the measurement equation for the lift co- efficient . . . . .	93
4.3	Identified parameters for the generalized mean-field model (2) . .	98

# Chapter 1

## Introduction

### 1.1 Motivation

Active flow control (AFC) is a fast growing multidisciplinary science and technology aimed at altering a natural flow state into a more desired state. Flow control is influencing all major areas of engineering: external aerodynamic performance, internal flows in propulsion systems, acoustic emission, combustion instabilities, transition and management of turbulence (King, 2007; Lu, 2009). In the last century, vast progress has been made in the aerodynamic design at the main operating condition, e.g. by shaping an airfoil for low drag cruise. Small passive devices, like turbulators or riblets, may improve flow performance further or stretch the operating regime. These techniques are predominantly based on a quasi-steady consideration. In contrast, active flow control devices, like zero-net-mass-flux actuators, synthetic jets, provide the designer with more freedom: the temporal dynamics can be directly controlled. This freedom can be exploited to: (i) extend the operating envelope, and (ii) to specifically target favourable instability mechanisms in the flow. In addition, if observations of the flow system are used for feedback, closed-loop control adds to these possibilities: (iii) modification of the system dynamics (e.g. stabilization), and (iv) reduction of the flow sensitivity (to external disturbances or parameter variations).

For the purpose of active closed-loop flow control a model of the flow is necessary for systematic feedback control design. To be useful for feedback design, the model must be sufficiently simple for feasible, real-time implementation, and

robustly represent the natural and actuated dynamics. Therefore, the first step in model development is to identify the key physical phenomena in the flow field. These key mechanisms are then absorbed in a so-called low-dimensional model of the flow field, typically in the form of a system of ordinary differential equations. The goal is not to describe every detail of the flow, but rather to eliminate all unimportant details, and obtain the simplest possible mathematical model (least-order), while retaining just enough of the details to describe the flow features of interest. In the specific case of separated flows, it is often desirable to suppress the main flow instability and thus change the mean-flow to improve aerodynamic performance. This implies that the base-flow change is an important physical phenomena that is to be included in the model. The term mean-field model<sup>1</sup> has been attributed to flow models that include this behaviour (Noack *et al.*, 2003). In this study, the focus is on the development of (generalized) mean-field models for flow control. The usefulness of the model approach is illustrated by nonlinear separation control.

## 1.2 Active flow control

In this section, some active flow control concepts are reviewed which are relevant for the current work. For a detailed overview of flow control in general, the following books are recommended: Gad-el-Hak (2000); Lu (2009). Surveys of passive methods can be found in Choi *et al.* (2008); Hucho (2002).

Active flow control changes a natural flow field by active means to achieve a desired state. Typically the flow is influenced by a blowing and/or suction device or acoustic actuation. In Fiedler & Fernholz (1990); Greenblatt & Wygnanski (2000) it is shown that periodic excitation is more effective and efficient in suppressing separated flows than steady actuation. This is a benefit common to most modern flow control techniques: they are able to achieve large-scale effects with small control inputs. It is however, to date, an art to design the right frequency and amplitude range of an actuator that triggers the instabilities which bring about the desired changes to the flow field. In particular, periodic actuation

---

<sup>1</sup>This definition is different from the one used in physics, which is used to describe a lumping procedure to simplify a problem.

can be used to delay separation of the flow over airfoils at high angles of attack (Amitay & Glezer, 2002; Becker *et al.*, 2007; Collis *et al.*, 2004; Seifert *et al.*, 1996).

Most studies in the area of active flow control focus on open-loop control. As discussed above, closed-loop control can significantly improve the performance of a flow control system. Moreover, in certain applications, closed-loop control is indispensable. As an example, the wake of a bluff body is considered. The adverse effects of flow separation, such as large pressure drag, oscillations, can be reduced by direct opposition control of the vortices in the wake (Gerhard *et al.*, 2003; Siegel *et al.*, 2003; Tadmor *et al.*, 2004). Indeed, this type of control only works if the actuator provides a force that directly counteracts the movement of the vortices. Another type of control that targets suppression of the wake instability is phase control, see Pastoor *et al.* (2008). This control uses a pressure sensor at the upper or lower edge at the stern of the body to detect a vortex. An actuator at the opposite edge provides an actuation signal that is exactly out of phase with the pressure measurement, thus yielding a simultaneous shedding of vortices. This leads to a decoupling of the alternating vortex formation in the shear layers and the wake by synchronizing the roll-up of upper and lower shear layers. The same effect can be achieved with open-loop control, where the actuators at both opposite edges are operated in phase, albeit at an increased actuation cost.

## 1.3 Model reduction

The main motivation for model reduction is to obtain models which are tractable for control design and real-time flow control. To obtain low-dimensional models, we will use the proper orthogonal decomposition (POD) in conjunction with the Galerkin projection. The Galerkin projection is a method for obtaining approximations to a high-dimensional dynamical system by projecting the dynamics onto a low-dimensional subspace. In the present case, the low-dimensional basis is spanned by POD modes.

Proper orthogonal decomposition is a method which extracts a low-dimensional basis from simulation or experimental data, which is optimal in a certain sense.

The POD method was initially only used to identify so-called coherent structures in turbulent flows (Holmes *et al.*, 1998). Along similar lines, the dynamic mode decomposition (DMD) will be used in this thesis to find the structures corresponding to dominant frequencies in the velocity field from snapshots of the flow.

More recently, the POD method has been used to construct low-dimensional models by Galerkin projection of the dynamic system onto the dominant POD modes. Examples include: boundary layer flow (Aubry *et al.*, 1988), turbulent channel flow (Lee *et al.*, 2001), flow past a cylinder (Noack *et al.*, 2003), cavity flow (Rowley & Juttijudata, 2005), transitional channel flow (Ilak & Rowley, 2008) and flow past a high-lift configuration (Luchtenburg *et al.*, 2009a).

The standard POD-Galerkin model often fails to capture important aspects of the dynamics of the original system. In the present work, this deficiency is addressed by the introduction of shift modes (Noack *et al.*, 2003). These shift modes incorporate the change of the base-flow during transients. Other techniques for improvement of the performance of POD models are discussed by Gordeyev & Thomas (2010); Siegel *et al.* (2008). A detailed discussion of the described methods is provided in the next chapter.

## 1.4 Outline

The main contributions of this work are: the application of a parameterized mean-field model for the optimization of sensor locations, and the implementation of a single-input single-output (SISO) opposition control for suppression of the wake instability of a circular cylinder; the development of a generalized mean-field model, and the application of this model to describe the flow around a high-lift configuration in a 2-D simulation; and a simplified mean-field model, which is tuned to describe the flow around a D-shaped bluff body in experiment. The usefulness of these models is demonstrated by implementation of a set-point controller in both simulation and experiment.

The contributions of each chapter are outlined below:

**Chapter 2.** The main methods, which are used in this thesis, are described in this chapter. It starts with a short introduction to reduced-order modelling and control. The fluid flow model, the derived Reynolds-averaged Navier-Stokes equations and their implications for modelling are discussed in § 2.1. In § 2.2 techniques for obtaining low-dimensional models are outlined. In particular we describe: the POD method in § 2.2.1, the DMD method in § 2.2.2, and the Galerkin method (GM) in § 2.2.3. The mean-field model approach is described in § 2.3. First the model approach is introduced with a simple example in § 2.3.1. Subsequently, a mean-field model for a single frequency (§ 2.3.2) and a generalized mean-field model for two frequencies (§ 2.3.3) are derived. The chapter concludes with a description of control design using a sliding mode controller (SMC) in § 2.4. This controller is used for set-point tracking based on the derived generalized mean-field model

**Chapter 3.** A mean-field POD-GM model (for a single frequency) is employed for the flow around a circular cylinder, describing natural vortex shedding and changes of the mean flow. The POD-GM model is parameterized for multiple operating conditions. This parameterized representation is used to optimize sensor locations. An observer which tracks the state of the system (the actual operating condition) is utilized in a single-input single-output (SISO) opposition control to suppress the wake instability.

**Chapter 4.** A mean-field POD-GM model (for two frequencies) is employed for the flow around a high-lift configuration. The model describes natural vortex shedding, the high-frequency actuated flow with increased lift, and transients between both states. The form of the dynamical system is highlighted from a phenomenological perspective in § 4.4. The mean-field model results are compared with the simulation results in § 4.6. Set-point tracking of the lift coefficient, based on the mean-field model, is described in § 4.7.

**Chapter 5.** A (simplified) mean-field model is employed to describe flow around a D-shaped bluff body in an experiment. The model describes natural vortex shedding, the low-frequency actuated flow with reduced drag and transients between both states. A DMD analysis of the flow field reveals

the dominant coherent structures in the natural and actuated flow (§ 5.4). Experimental data are used to identify the model parameters. The model is used for set-point tracking of the base pressure coefficient in § 5.6.2.

**Chapter 6.** The conclusions of this work and possible directions for future work are outlined in the final chapter.

## Chapter 2

# Reduced-order models and control

Feedback flow control strategies in experiment require models which are sufficiently simple for feasible, real-time implementation, and robust enough to cope with uncertainties. In this chapter, reduced-order models are outlined that capture key physical phenomena of the flow. These models are used as a base for nonlinear control design.

A common method for obtaining a low-dimensional basis of a system is the proper orthogonal decomposition (POD). By Galerkin projection onto the low-dimensional POD subspace, a reduced-order description of the system is obtained (Holmes *et al.*, 1998). This standard Galerkin system is over-optimized for one particular reference condition. Hence, transient behaviour is not (adequately) captured. In mean-field theory (Noack *et al.*, 2003) a so-called shift-mode is added to the basis. This shift-mode represents the effect of a changing base flow and significantly improves the resolution of the transient dynamics.

The mean-field theory was originally motivated by extending the concept of linear stability theory (Stuart, 1958). A flow cannot grow without bound and hence there must be a nonlinear saturation mechanism. The Reynolds-averaged Navier-Stokes equation hints at the most important correction. The mean-flow is quadratically dependent on the fluctuation velocities (Reynolds stresses). Therefore, a shift-mode, which describes the mean-field correction, is added to the basis of linear stability modes. In the case of one dominant frequency, this approach



leads to the single frequency mean-field model by Noack *et al.* (2003). Shift-modes can be included for each dominant frequency of the system under consideration. In this chapter, the mean-field model is generalized to multiple frequencies.

The mean-field models are used for nonlinear controller design. One particular control, namely sliding mode control (SMC), is summarized in this chapter.

## 2.1 Fluid flow model

The flow equations governing the motion of a fluid follow from physical conservation laws (Batchelor, 1967). In this work, incompressible Newtonian fluids are considered. The flow is described in a Cartesian coordinate system  $\mathbf{x} = (x, y, z)$ , with the  $x$ -axis parallel to the streamwise direction, the  $y$ -axis in lateral direction, and the  $z$ -axis in spanwise direction. The unit vectors in positive  $x$ -,  $y$ - and  $z$ -direction are denoted by  $\mathbf{e}_x$ ,  $\mathbf{e}_y$  and  $\mathbf{e}_z$ . In the following, the standard symbols are used for denotation of velocity ( $\mathbf{u} = (u, v, w)^T$ ), pressure ( $p$ ) and time ( $t$ ). All physical variables are assumed to be nondimensionalized with respect to a characteristic length  $L$ , a velocity  $U$  and a constant density  $\rho$ . In § 2.1.1 the basic equations of fluid dynamics are recapitulated. The Reynolds-averaged Navier-Stokes (RANS) equation is recapitulated in § 2.1.2. Transient behaviour and implied mean-field deformation is discussed in § 2.1.3.

### 2.1.1 Basic equations of fluid dynamics

The continuity equation represents the conservation of mass

$$\nabla \cdot \mathbf{u} = 0, \quad (2.1)$$

and the Navier-Stokes equation the conservation of momentum

$$\frac{\partial \mathbf{u}}{\partial t} + \nabla \cdot (\mathbf{u} \otimes \mathbf{u}) = \mathbf{g}^a - \nabla p + \frac{1}{Re} \Delta \mathbf{u}, \quad (2.2)$$

where  $\otimes$  defines the dyadic product between two vectors, i.e. the components  $Q_{ij}$  of the dyadic product  $\mathbf{Q} = \mathbf{u} \otimes \mathbf{v}$  are defined by  $Q_{ij} = u_i v_j$ ,  $\mathbf{g}^a$  is a volume force and  $Re = UL/\nu$  the Reynolds number. The Navier-Stokes (NS) equation is only a function of the velocity field, since the pressure field  $p$  is a function of the

velocity field — modulo a constant. Together with suitable initial and boundary conditions, (2.1) and (2.2) govern the motion of an incompressible Newtonian fluid. Practically, these equations can only be solved for moderate Reynolds numbers. This model free computation of turbulence is called direct numerical simulation (DNS).

### 2.1.2 Reynolds-averaged Navier-Stokes equation

In engineering practice, turbulent flows are generally modelled by the (unsteady) Reynolds-averaged Navier-Stokes equation (RANS), in order to achieve computer time and memory requirements that are feasible for (industrial) applications (Wesseling, 2000). Before presenting the RANS equations, the prerequisites are discussed.

Following the original idea of Reynolds (1895), a quantity  $f(\mathbf{x}, t)$  is decomposed into a mean value  $\overline{f}$  and a fluctuation  $f'$  as follows:

$$f = \overline{f} + f', \quad (2.3)$$

where the bar indicates an averaging operator. This operator is required to fulfill the Reynolds conditions (Monin & Yaglom, 2007)

$$\overline{f + g} = \overline{f} + \overline{g} \quad (2.4a)$$

$$\overline{af} = a\overline{f}, \quad a \in \mathbb{R} \quad (2.4b)$$

$$\overline{a} = a, \quad a \in \mathbb{R} \quad (2.4c)$$

$$\overline{\frac{\partial f}{\partial s}} = \frac{\partial \overline{f}}{\partial s} \quad (2.4d)$$

$$\overline{\overline{f}g} = \overline{f}\overline{g}. \quad (2.4e)$$

Properties (2.4a)–(2.4c) imply the linearity of the operator. In addition, the following consequences can be derived

$$\overline{\overline{f}} = \overline{f}, \quad \overline{f'} = 0, \quad \overline{\overline{f}g} = \overline{f}\overline{g}, \quad \overline{\overline{f}g'} = 0. \quad (2.5)$$

In order to interpret the Reynolds assumptions, the averaging operator must be explicitly defined. The three most pertinent forms in turbulence model research

are the time average, the spatial average and the ensemble average. The running time average

$$\bar{f}(\mathbf{x}, t) = \frac{1}{T} \int_{-\frac{T}{2}}^{\frac{T}{2}} f(\mathbf{x}, t + \tau) d\tau \quad (2.6)$$

satisfies the linearity condition and commutes with the derivative. However, equation (2.4e) will in general not be satisfied exactly for any finite choice of  $T$

$$\begin{aligned} \frac{1}{T} \int_{-\frac{T}{2}}^{\frac{T}{2}} \left\{ \left( \frac{1}{T} \int_{-\frac{T}{2}}^{\frac{T}{2}} f(\mathbf{x}, t + \tau) d\tau \right) g(\mathbf{x}, t + \tilde{\tau}) \right\} d\tilde{\tau} \neq \\ \left( \frac{1}{T} \int_{-\frac{T}{2}}^{\frac{T}{2}} f(\mathbf{x}, t + \tau) d\tau \right) \left( \frac{1}{T} \int_{-\frac{T}{2}}^{\frac{T}{2}} g(\mathbf{x}, t + \tau) d\tau \right). \end{aligned}$$

Condition (2.4e) is usually relaxed to the spectral gap requirement, which implies that  $T$  is large compared to the time scale of turbulent fluctuations  $T_1$ , but small compared to the time scale of other time-dependent features of the flow  $T_2$ , i.e.  $T_1 \ll T \ll T_2$ . The averaging window may be chosen in such a way that (2.4e) is satisfied approximately. Reynolds confined himself to this type of argument. In the case of stationary turbulence,  $T \rightarrow \infty$ , all conditions are met.

More general space time averaging operators can be defined (Monin & Yaglom, 2007) that also fulfill conditions (2.4a)–(2.4d). The more complex condition (2.4e) is, as above, not satisfied. Difficulties that can arise are described in Galmarini & Thunis (1999).

A third and more universal possibility is to define the averaging operator as an average over a statistical ensemble

$$\bar{f}(\mathbf{x}, t) = \lim_{N \rightarrow \infty} \frac{1}{N} \sum_{i=1}^N f(\mathbf{x}, t_i). \quad (2.7)$$

This definition fulfills all Reynolds conditions since it does not involve space nor time. The probability approach to the theory of turbulence is pursued in modern books.

The continuity equation for the mean flow follows from averaging of (2.1)

$$\nabla \cdot \bar{\mathbf{u}} = 0. \quad (2.8)$$

Taking the mean of (2.2) gives the Reynolds-averaged Navier-Stokes equation

$$\frac{\partial \bar{\mathbf{u}}}{\partial t} + \nabla \cdot (\bar{\mathbf{u}} \otimes \bar{\mathbf{u}}) = \bar{\mathbf{g}}^a - \nabla \bar{p} + \frac{1}{Re} \Delta \bar{\mathbf{u}} - \nabla \cdot \overline{(\mathbf{u}' \otimes \mathbf{u}')}. \quad (2.9)$$

The last term on the right hand side comprises the so-called Reynolds stresses. These have to be related to the mean motion itself before the equations (2.8) and (2.9) can be solved, since the number of unknowns and number of equations must be equal. The absence of these additional equations is often referred to as the closure problem.

In practice semi empirical relations are introduced leading to eddy viscosity models or Reynolds stress models. The eddy viscosity depends on certain quantities that obey partial differential equations. In Chapter 4, a  $k$ - $\omega$  eddy viscosity model will be used. This model includes two transport equations to represent the turbulent kinetic energy  $k$  and the dissipation per unit turbulence kinetic energy  $\omega$  of the flow. The eddy viscosity is determined from these two quantities (Wilcox, 1994).

### 2.1.3 Transient behaviour and mean flow distortion

The coupling between fluctuations and base flow velocities is communicated by the RANS equation (2.9). During transients the mean flow  $\bar{\mathbf{u}}$  is distorted by finite disturbances  $\mathbf{u}'$ . In practice, usually only snapshots from a converged trajectory of the attractor dynamics are available. These snapshots contain the equilibrium solution  $\bar{\mathbf{u}} = \bar{\mathbf{u}}(\mathbf{x})$ . Consider as a special case the steady solution for  $\mathbf{g}^a = 0$ , where  $\bar{\mathbf{u}} = \mathbf{u}_s$  is obtained by setting the time derivative in the RANS equation equal to zero

$$\nabla \cdot (\mathbf{u}_s \otimes \mathbf{u}_s) = -\nabla p_s + \frac{1}{Re} \Delta \mathbf{u}_s. \quad (2.10)$$

There is no corresponding equation for the fluctuations, since they equal zero.

In linear stability theory, infinitesimal disturbances with respect to the steady solution are considered. The Navier-Stokes equation is linearized around a steady solution  $(\mathbf{u}_s, p_s)$  with perturbation  $(\mathbf{u}_s + \mathbf{u}', p_s + p')$ , yielding the following distur-

bance equations

$$\nabla \cdot \mathbf{u}' = 0, \quad (2.11)$$

$$\frac{\partial \mathbf{u}'}{\partial t} + \nabla \cdot (\mathbf{u}' \otimes \mathbf{u}_s) + \nabla \cdot (\mathbf{u}_s \otimes \mathbf{u}') = -\nabla p' + \frac{1}{Re} \Delta \mathbf{u}'. \quad (2.12)$$

These equations can be solved with a normal mode ansatz, i.e.  $\mathbf{u}' = \mathbf{u}(\mathbf{x}) \exp(\lambda t)$ ,  $p' = p(\mathbf{x}) \exp(\lambda t)$ . Substitution of this ansatz leads to an eigenproblem. The growth rate of mode  $i$  is given by  $\sigma_i = \Re(\lambda_i)$  and its frequency by  $\omega_i = \Im(\lambda_i)$ . This basis is similar to the ensemble snapshots of a converged attractor in the sense that only a very local part of the solution is described.

Initially an unstable disturbance to the steady solution ( $\sigma_i > 0$ ) grows exponentially with time, but eventually it reaches such a size that the transport of momentum by the finite fluctuations is appreciable. This causes the Reynolds stress  $\nabla \cdot (\overline{\mathbf{u}' \otimes \mathbf{u}'})$  in (2.9) to change the mean flow. Vice versa, the mean flow distortion modifies the rate of transfer of energy from the mean flow to the disturbance. In this case, the flow interactions are strongly nonlinear and can no longer be described by linear equations. A first order approximation of the base-flow change or mean-field correction can be obtained by subtracting the steady state solution from the mean-flow at the attractor:

$$\delta \mathbf{u} = \bar{\mathbf{u}} - \mathbf{u}_s$$

Setting  $\mathbf{g}^a = 0$ , substituting  $\bar{\mathbf{u}} = \mathbf{u}_s + \delta \mathbf{u}$ ,  $\bar{p} = p_s + \delta p$ , into the RANS equation (2.9), and subtracting (2.10) yields

$$\frac{\partial \delta \mathbf{u}}{\partial t} + \nabla \cdot (\mathbf{u}_s \otimes \delta \mathbf{u}) + \nabla \cdot (\delta \mathbf{u} \otimes \mathbf{u}_s) = -\nabla \delta p + \frac{1}{Re} \Delta \delta \mathbf{u} - \nabla \cdot (\overline{\mathbf{u}' \otimes \mathbf{u}'} + O(\delta \mathbf{u}^2), \quad (2.13)$$

which shows that the mean-field correction  $\delta \mathbf{u}$  quadratically depends on the fluctuation amplitude (Noack, 2006). This form is the starting point for mean-field theory. The basis for the local solution is not necessarily given by linear stability modes. In fact, we will be using the POD as a local basis. This expansion is enriched by adding mean-field corrections, leading to a mean-field model (see § 2.3).

## 2.2 Model reduction for fluid flows

In this section, techniques for obtaining reduced-order models of fluid flows are described. An overview of the basic tools, the proper orthogonal decomposition (§ 2.2.1), the dynamic mode decomposition (§ 2.2.2) and the Galerkin method (§ 2.2.3) is provided. The implementation of actuation in Galerkin models is described in § 2.2.4.

### 2.2.1 Proper orthogonal decomposition

The main objective in proper orthogonal decomposition (POD) is to obtain an optimal low-dimensional basis for representing an ensemble of high-dimensional experimental or simulation data. This low-dimensional basis can in turn be used to formulate reduced-order models of complex flows. POD decomposes a given (fluctuating) flow field  $\mathbf{u}'(\mathbf{x}, t)$ <sup>1</sup> into an orthonormal system of spatial modes  $\mathbf{u}_i(\mathbf{x})$  and corresponding (orthogonal) temporal coefficients or mode amplitudes  $a_i(t)$

$$\mathbf{u}'(\mathbf{x}, t) = \sum_{i=1}^M a_i(t) \mathbf{u}_i(\mathbf{x}). \quad (2.14)$$

This basis is optimal in the sense that a truncated series expansion of the data in this basis has a smaller mean square truncation error than a representation by any other basis. The POD provides a natural ordering of the spatial modes by measure of their mean square temporal coefficients (i.e. their kinetic energy). In conjunction with the Galerkin method a system of ordinary differential equations, called the Galerkin system (GS), can be derived for the temporal evolution of the mode amplitudes.

The term proper orthogonal decomposition was introduced by Lumley (1998) as an objective definition of coherent structures. The POD is also known as the Karhunen-Loève expansion. Its discrete relatives are called principal component analysis (PCA) and singular value decomposition (SVD). The reader is referred to Wu *et al.* (2003) for the relations. Tutorials on the discrete and continuous formulations of POD have been presented by Chatterjee (2000); Cordier & Bergmann

---

<sup>1</sup>The prime is suppressed in the following.

(1999); Luchtenburg *et al.* (2009b). For a thorough treatment of the continuous version of POD see Astrid (2004); Holmes *et al.* (1998); Rowley (2002).

### POD basis problem

First some definitions are introduced. The velocity field on the spatial domain  $\Omega$  is formally embedded in a mathematical space. Let  $H$  be a suitable Hilbert space with the following inner product<sup>1</sup> between two vector fields  $\mathbf{f}$ ,  $\mathbf{g}$ ,

$$(\mathbf{f}, \mathbf{g})_{\Omega} = \int_{\Omega} \mathbf{f} \cdot \mathbf{g} \, d\mathbf{x}, \quad (2.15)$$

and the induced norm

$$\|\mathbf{f}\| = \sqrt{(\mathbf{f}, \mathbf{f})}. \quad (2.16)$$

The time averaging operator is defined as

$$\bar{a} = \frac{1}{T} \int_0^T a(t) \, dt. \quad (2.17)$$

Premise for the POD is spatial correlation (coherence) of the velocity flow field. The optimal modes  $\mathbf{u}_i$  are defined as the eigenfunctions of the Fredholm equation (see Appendix A.1 for the derivation)

$$\int_{\Omega} \mathbf{R}(\mathbf{x}, \mathbf{y}) \mathbf{u}_i(\mathbf{y}) \, d\mathbf{y} = \lambda_i \mathbf{u}_i(\mathbf{x}). \quad (2.18)$$

Here,  $\mathbf{R}(\mathbf{x}, \mathbf{y})$  is the two-point autocorrelation tensor for the flow field, defined by

$$\mathbf{R}(\mathbf{x}, \mathbf{y}) = \overline{\mathbf{u}(\mathbf{x}, t) \otimes \mathbf{u}(\mathbf{y}, t)}, \quad (2.19)$$

or in index notation

$$R_{ij} = \overline{u_i(\mathbf{x}, t) u_j(\mathbf{y}, t)}, \quad (2.20)$$

where the indices  $ij$  refer to the velocity components, i.e. in three dimensions  $\mathbf{u} = (u_1, u_2, u_3)$ . The modes are ordered with respect to the decreasing real

---

<sup>1</sup>This definition of the inner product constrains the Hilbert space to the  $\mathcal{L}_2(\Omega)$  space of square-integrable functions, with the standard inner product. More generally the notion of a Hilbert space with a suitable inner product suffices.

## 2.2 Model reduction for fluid flows

positive eigenvalues  $\lambda_1 \geq \lambda_2 \geq \lambda_3 \geq \dots > 0$ . The kinetic energy contained in mode  $i$  is measured by the eigenvalue  $\lambda_i$ , and the sum of the eigenvalues is equal to the total energy in the snapshots. Note that zero eigenvalues are not considered since they do not contribute to the energy. Using the orthonormality of the modes, the time-dependent amplitudes follow from the projection

$$a_i(t) = (\mathbf{u}(\mathbf{x}, t), \mathbf{u}_i(\mathbf{x}))_{\Omega}. \quad (2.21)$$

In practice, data is available at discrete points and the integral problem is approximated using a suitable quadrature rule for the time average. Let an ensemble of  $M$  snapshots be given  $\{\mathbf{u}(\mathbf{x}_i, t_j)\}$ , where  $i = 1, \dots, K$  and  $j = 1, \dots, M$ . The approximation of the auto-correlation function (2.19) is given by

$$\mathbf{R}_{ij} = \sum_{k=1}^M w_k \mathbf{u}(\mathbf{x}_i, t_k) \cdot \mathbf{u}(\mathbf{x}_j, t_k), \quad (2.22)$$

where  $w_k$  are the quadrature weights such that  $\sum_{k=1}^M w_k = 1$  and ‘ $\cdot$ ’ denotes the standard Euclidean inner product. To simplify notation the snapshots are collected in a matrix

$$\mathbf{X} = \begin{bmatrix} \mathbf{u}^{(1)}(\mathbf{x}_1) & \mathbf{u}^{(2)}(\mathbf{x}_1) & \dots & \mathbf{u}^{(M)}(\mathbf{x}_1) \\ \mathbf{u}^{(1)}(\mathbf{x}_2) & \mathbf{u}^{(2)}(\mathbf{x}_2) & \dots & \mathbf{u}^{(M)}(\mathbf{x}_2) \\ \vdots & \vdots & & \vdots \\ \mathbf{u}^{(1)}(\mathbf{x}_K) & \mathbf{u}^{(2)}(\mathbf{x}_K) & \dots & \mathbf{u}^{(M)}(\mathbf{x}_K) \end{bmatrix} = [\mathbf{u}^{(1)} \quad \mathbf{u}^{(2)} \quad \dots \quad \mathbf{u}^{(M)}], \quad (2.23)$$

where  $\mathbf{u}^{(i)}(\mathbf{x}_j) = \mathbf{u}(\mathbf{x}_i, t_j)$ . The row-direction of  $\mathbf{X}$  corresponds with the discrete spatial domain and the columns contain the snapshots. In complete analogy to (2.18), the (discrete) POD modes are computed as the eigenvectors of the eigenvalue problem

$$\mathbf{X}\mathbf{W}\mathbf{X}^T = \mathbf{U}\mathbf{\Lambda}, \quad (2.24)$$

where  $\mathbf{W} = \text{diag}(w_1, \dots, w_M)$ . The POD modes are the columns of  $\mathbf{U}$ . This method is known as the direct method (or computation in the spatial domain). If time-averaging is approximated by the ensemble average,  $w_k = 1/M$ , the eigenproblem simplifies to

$$\frac{1}{M}\mathbf{X}\mathbf{X}^T = \mathbf{U}\mathbf{\Lambda}. \quad (2.25)$$



This shows that the POD modes correspond to the left singular vectors of the matrix  $\mathbf{X}$ . Thus, there is a direct connection between the POD and the singular value decomposition (SVD) of the snapshot matrix

$$\mathbf{X} = \mathbf{U}\mathbf{\Sigma}\mathbf{V}^T. \quad (2.26)$$

The matrices  $\mathbf{U}$ ,  $\mathbf{V}$  are orthonormal and  $\mathbf{\Sigma}$  is a diagonal matrix (padded with zeros) that contains the singular values. Using the SVD, it is straightforward to show that the POD modes can also be computed by

$$\mathbf{U} = \mathbf{X}\mathbf{V}, \quad (2.27)$$

where the weights  $\mathbf{V}$  are the scaled temporal coefficients that are calculated from the eigenproblem

$$\frac{1}{M} (\mathbf{X}^T \mathbf{X}) \mathbf{V} = \mathbf{V} \mathbf{\Sigma}. \quad (2.28)$$

This method of computing the POD is called the method of snapshots ([Sirovich, 1987](#)) or discretization in the temporal domain. The method of snapshots can also be directly derived from the continuous formulation of the POD method (see [Appendix A.2](#) for the derivation). In this case the results are slightly different, since the quadrature weights are based on an approximation of a spatial integral.

Note that the method of snapshots yields a correlation matrix with size  $M \times M$ , whereas discretization in the three dimensional spatial domain yields a matrix with size  $3K \times 3K$ . The method of snapshots makes it possible to compute POD modes for high-dimensional systems, where the number of snapshots is significantly lower than the number of grid points. The direct method can be advantageous for long time samples of few experimental sensor measurements, i.e.  $M \gg 3K$ .

### Discussion

The POD method extracts modes from an ensemble of snapshots that are sorted with respect to energy content. In this sense the method often provides clues about the physics of a flow field. The optimality property also implies that important dynamic information characterized by low energy may not be included in a low-dimensional POD approximation of the system. Secondly, since the

POD approach is data driven, information may simply not be captured by the snapshots. This lack of information can lead to problems if one uses this basis in conjunction with the Galerkin method to derive a dynamic system (see § 2.2.3). The POD/Galerkin model is often quite fragile: the models depend unpredictably on the number of modes kept and often a large number of modes is required to capture qualitatively reasonable dynamics (Rowley & Batten, 2009). Several suggestions have been proposed to address these problems:

- (i) The inclusion of multiple operating conditions in one snapshot ensemble (Khibnik *et al.*, 2000; Taylor & Glauser, 2004). An example is the flow around an airfoil. The velocity flow field is recorded for different angles of attack. All snapshots are included in one ensemble and the POD modes are computed. Another example is the chirp excitation of a cylinder wake by rotation of the cylinder (Bergmann *et al.*, 2004). This approach is known as global or ‘basket’-POD. This ansatz always includes bias towards certain flow conditions.
- (ii) A more refined variant of the above approach is Split POD (Camphouse *et al.*, 2008) where the POD of a baseline ensemble is expanded with POD modes from another ensemble (e.g. an open-loop forced flow). The information of the POD modes of the baseline ensemble is subtracted from the second ensemble. The added POD modes are obtained from the corrected snapshot ensemble. This approach guarantees orthonormality of the modes.
- (iii) A recursive or sequential POD procedure (Annaswamy *et al.*, 2002; Jørgensen *et al.*, 2003). The POD is recursively updated for new flow states.
- (iv) The inclusion of additional modes to the POD modes. In this manner, the accuracy of the POD modes for the reference condition is conserved and the additional modes extend the range of applicability and robustness of the POD-Galerkin model. An example is the mean-field model by Noack *et al.* (2003).
- (v) Parameterization of multiple operating conditions. Each operating condition is described by its own POD. This procedure is sometimes referred

to as conditional POD (Taylor & Glauser, 2004) or parameterized POD (Lehmann *et al.*, 2005).

- (vi) Similarly to the previous approach, multiple operating conditions are described, each by its own POD. If there is a smooth transition from one to another operating condition, the (qualitative) topology of the POD modes remains the same. Each topologically similar POD mode is described as a function of the operating condition. This ensemble can be expanded by POD as well. Hence, this approach is coined Double POD (DPOD, Siegel *et al.*, 2008).
- (vii) Inclusion of dynamic states of the system by computation of an approximate balanced truncation. This balanced truncation may be viewed as POD of a particular dataset, using the observability Gramian as an inner product (Rowley, 2005). This method is known as Balanced POD (BPOD). Note that this approach is limited to a linear (or adequately linearized) system.

### 2.2.2 Dynamic mode decomposition

The dynamic mode decomposition (DMD) provides, like POD, a basis for a snapshot ensemble. It provides an alternative to POD if an ensemble of *time-resolved* snapshots is available. The evolution of the snapshots is assumed to be governed by a linear dynamic system. As in linear stability analysis, the eigenvalues of the state matrix characterize the frequencies and the growth rates of the system. Hence, DMD can be viewed as a Laplace analysis of the snapshots.

The following description of the dynamic mode decomposition is adapted from Rowley *et al.* (2009). As above, see (2.23), let an ensemble of  $M$  snapshots be given and stack the first  $M - 1$  snapshots in a matrix  $\mathbf{X} = [\mathbf{u}^{(1)}, \dots, \mathbf{u}^{(M-1)}]$ . The basic premise of the method is that the snapshots are assumed to be generated by a linear dynamical system:

$$\mathbf{u}^{(k+1)} = \mathbf{A}\mathbf{u}^{(k)}. \quad (2.29)$$

The eigenvalues and eigenvectors of the matrix  $\mathbf{A}$  completely characterize the behaviour of the dynamical system. The DMD is a method to compute the

## 2.2 Model reduction for fluid flows

---

approximate eigenvectors or Ritz vectors of the system matrix. The Ritz vectors are called the Koopman or dynamic modes. Assume that the last snapshot in the ensemble can be expressed as a linear combination of the previous snapshots, i.e.

$$\mathbf{u}^{(M)} = \mathbf{A}\mathbf{u}^{(M-1)} = c_1\mathbf{u}^{(1)} + \dots + c_{M-1}\mathbf{u}^{(M-1)} = \mathbf{X}\mathbf{c}, \quad (2.30)$$

where  $\mathbf{c} = (c_1, \dots, c_{M-1})$ . In general, this equality is not satisfied and instead  $\mathbf{c}$  is computed as the least square approximation. The snapshots are related by the following matrix equation

$$\mathbf{A}\mathbf{X} = \mathbf{X}\mathbf{C}, \quad (2.31)$$

where  $\mathbf{C}$  is a companion matrix

$$\mathbf{C} = \begin{bmatrix} 0 & 0 & \dots & 0 & c_1 \\ 1 & 0 & & 0 & c_2 \\ 0 & 1 & & 0 & c_3 \\ \vdots & & \ddots & & \vdots \\ 0 & \dots & 0 & 1 & c_{M-1} \end{bmatrix}. \quad (2.32)$$

The eigenvalues and eigenvectors of  $\mathbf{C}$ , given by  $\mathbf{C}\mathbf{a} = \lambda\mathbf{a}$ , directly lead to (a subset of) the eigenvalues and eigenvectors of  $\mathbf{A}$ , since

$$\mathbf{A}(\mathbf{X}\mathbf{a}) = \mathbf{X}\mathbf{C}\mathbf{a} = \lambda(\mathbf{X}\mathbf{a}). \quad (2.33)$$

Thus, eigenvalues of  $\mathbf{C}$  are eigenvalues of  $\mathbf{A}$  and  $\mathbf{v} = \mathbf{X}\mathbf{a}$  is an eigenvector of  $\mathbf{A}$ . The spectral decomposition of  $\mathbf{C}$  can be written as

$$\mathbf{C} = \mathbf{T}^{-1}\mathbf{\Lambda}\mathbf{T}, \quad (2.34)$$

where the eigenvectors are columns of  $\mathbf{T}^{-1}$  and  $\mathbf{\Lambda} = \text{diag}(\lambda_1, \dots, \lambda_{M-1})$ . Using this notation, the Koopman modes are given by the columns of the following matrix

$$\mathbf{V} = \mathbf{X}\mathbf{T}^{-1}. \quad (2.35)$$

This leads to the connection between the snapshot matrix and the modal decomposition:  $\mathbf{X} = \mathbf{V}\mathbf{T}$ , where  $\mathbf{T}$  contains the mode amplitudes.

In contrast to POD, the mode amplitudes are usually normalized and the norm of a mode is considered as an indicator of an important flow feature. The

growth or decay rate of a mode can also be used as a selector to extract unstable or stable modes. Oscillatory modes and their amplitudes are found as complex conjugate pairs. The frequency  $\omega_j$  and growth rate  $\sigma_j$  of mode  $j$  are computed from the eigenvalues of  $\mathbf{C}$ :

$$\omega_j = \text{Im}\{\log(\lambda_j)\}/\Delta t, \quad (2.36a)$$

$$\sigma_j = \text{Re}\{\log(\lambda_j)\}/\Delta t, \quad (2.36b)$$

where  $\Delta t$  is the time step between two consecutive snapshots.

### Discussion

Unlike POD, the DMD requires a set of ordered (time resolved) snapshots, otherwise the mapping defined by (2.29) is not meaningful. The dynamic modes, by definition, have mode amplitudes with well defined frequencies. (If the snapshot matrix  $\mathbf{X}$  is transposed, the method can also be applied to reveal spatial wave-like structures). These modes can be ordered with respect to their norm, their frequency or growth rate.

On the contrary, the POD procedure can be interpreted as a purely statistical procedure. It involves a time-averaging (spatial-averaging) step and the modes are obtained from maximization of the variance over the ensemble of snapshots. The obtained modes are by definition statistically decorrelated, because of the bi-orthogonality of the modes and the mode amplitudes (see (2.26), (A.20) and (A.22)). This property does not hold for the DMD, i.e. the extracted basis is in general not orthogonal.

### 2.2.3 Galerkin method

In the previous sections, the procedure for obtaining a basis from an ensemble of snapshots was discussed. In the case of a low-dimensional approximation of the velocity flow field, this necessarily implies that the governing Navier-Stokes equation is not satisfied exactly. Here, the Galerkin method, see e.g. [Fletcher \(1984\)](#), is used to derive evolution equations for the approximate basis.

Starting point of the Galerkin method is the *Galerkin approximation*:

$$\mathbf{u}(\mathbf{x}, t) = \sum_{i=0}^N a_i(t) \mathbf{u}_i(\mathbf{x}), \quad (2.37)$$

where  $\mathbf{u}_0(\mathbf{x})$  is a steady base flow (e.g., the attractor mean or the steady solution of the Navier-Stokes equation) and  $\{\mathbf{u}_i\}_{i=1}^N \subset \mathcal{L}_2(\Omega)$  is an orthonormal (here: POD) basis. Time dependency is described by the mode amplitudes  $a_i$ . Following a notation of [Rempfer & Fasel \(1994\)](#),  $a_0 \equiv 1$  by definition. The incompressible Navier-Stokes equation (2.2) is rewritten in operator form

$$\mathcal{N}[\mathbf{u}] = \partial_t \mathbf{u} + \nabla \cdot (\mathbf{u} \otimes \mathbf{u}) + \nabla p - \nu \Delta \mathbf{u} - \mathbf{g}^a = 0, \quad (2.38)$$

where  $\nu = 1/Re$  is the reciprocal of the Reynolds number. An ordinary differential equation governing the evolution of the temporal coefficients  $a_i(t)$  is obtained by substituting (2.37) into the Navier-Stokes equation (2.38) <sup>1</sup>, and projecting onto the subspace spanned by the expansion modes:

$$(\mathcal{N}[\mathbf{u}(\mathbf{x}, t)], \mathbf{u}_i(\mathbf{x}))_\Omega = 0 \quad \text{for } i = 1, \dots, N. \quad (2.39)$$

This is the so-called Galerkin projection. The resulting *Galerkin system* is quadratically nonlinear

$$\frac{da_i}{dt} = \nu \sum_{j=0}^N l_{ij} a_j + \sum_{j,k=0}^N q_{ijk} a_j a_k \quad \text{for } i = 1, \dots, N. \quad (2.40)$$

Table 2.1 provides the definition of the coefficients  $l_{ij}$  and  $q_{ijk} = q_{ijk}^c + q_{ijk}^p$ . The contribution of the pressure term to the Galerkin system (last row in table 2.1) is neglected, since for absolutely unstable wake flows this term is relatively small (see e.g. [Noack et al., 2005](#)). Alternatively, since the pressure term does not change the model structure, it can be lumped in the other coefficients.

In vector notation, the system reads

$$\frac{d\mathbf{a}}{dt} = \mathbf{c} + \mathbf{L}(\mathbf{a}) + \mathbf{Q}(\mathbf{a}, \mathbf{a}), \quad (2.41)$$

where the vector notations denote  $\mathbf{a} = [a_1, \dots, a_N]^T$ ,  $\mathbf{c} = [c_1, \dots, c_N]^T$ , and

$$\mathbf{c}|_i = \nu l_{i0} + q_{i00}, \quad \mathbf{L}(\mathbf{a})|_i = \sum_{j=1}^N (\nu l_{ij} + q_{i0j} + q_{ij0}) a_j, \quad \mathbf{Q}(\mathbf{a}, \mathbf{a})|_i = \sum_{j,k=1}^N q_{ijk} a_j a_k.$$

NSE	NSE with $\mathbf{u} = \mathbf{u}_0 + \mathbf{u}'$	Galerkin projection	Galerkin system	Simplified nomenclature
$\partial_t \mathbf{u} =$	$\partial_t \mathbf{u}' =$	$(\mathbf{u}_i, \partial_t \mathbf{u}')_\Omega =$	$\frac{d}{dt} a_i =$	$\frac{d}{dt} a_i =$
$-\nabla \cdot [\mathbf{u} \otimes \mathbf{u}]$	$-\nabla \cdot [\mathbf{u}_0 \otimes \mathbf{u}_0]$ $-\nabla \cdot [\mathbf{u}' \otimes \mathbf{u}_0]$ $-\nabla \cdot [\mathbf{u}_0 \otimes \mathbf{u}']$ $-\nabla \cdot [\mathbf{u}' \otimes \mathbf{u}']$	$-(\mathbf{u}_i, \nabla \cdot [\mathbf{u}_0 \otimes \mathbf{u}_0])_\Omega$ $-(\mathbf{u}_i, \nabla \cdot [\mathbf{u}' \otimes \mathbf{u}_0])_\Omega$ $-(\mathbf{u}_i, \nabla \cdot [\mathbf{u}_0 \otimes \mathbf{u}'])_\Omega$ $-(\mathbf{u}_i, \nabla \cdot [\mathbf{u}' \otimes \mathbf{u}'])_\Omega$	$q_{i00}^c$ $+ \sum_{j=1}^N q_{ij0}^c a_j$ $+ \sum_{j=1}^N q_{i0j}^c a_j$ $+ \sum_{j,k=1}^N q_{ijk}^c a_j a_k$	$\sum_{j,k=0}^N q_{ijk}^c a_j a_k$
$+\nu \Delta \mathbf{u}$	$+\nu \Delta \mathbf{u}_0$ $+\nu \Delta \mathbf{u}'$	$+\nu (\mathbf{u}_i, \Delta \mathbf{u}_0)_\Omega$ $+\nu (\mathbf{u}_i, \Delta \mathbf{u}')_\Omega$	$+\nu l_{i0}$ $+\nu \sum_{j=1}^N l_{ij} a_j$	$+\nu \sum_{j=0}^N l_{ij} a_j$
$-\nabla p$	$-\nabla p_0$ $-\nabla p'$	$-(\mathbf{u}_i, \nabla p_0)_\Omega$ $-(\mathbf{u}_i, \nabla p')_\Omega$	$+q_{i00}^p$ $+ \sum_{\substack{j,k=0 \\ j+k>0}}^N q_{ijk}^p a_j a_k$	$+ \sum_{j,k=0}^N q_{ijk}^p a_j a_k$

Table 2.1: Derivation of the Galerkin system (GS). In each column terms or corresponding terms of the Navier-Stokes equation (NSE) are enlisted. The rows show the local acceleration, convective acceleration, viscous and pressure term. From left to right, the NSE is transformed into the GS in five steps: (1) NSE in its original form, (2) NSE after Reynolds decomposition, (3) Galerkin projection, (4) GS, and (5) a simplified nomenclature of the GS employing  $a_0 \equiv 1$ . The Galerkin projection of the pressure term is derived in [Noack \*et al.\* \(2005\)](#). This table is adapted from [Noack \(2006\)](#)

As discussed in § 2.2.1, truncation effects and numerical issues may result in substantial deviations of the predicted dynamics. Such distortions may be resolved by calibration methods (Galletti *et al.*, 2004; Tadmor *et al.*, 2004).

### 2.2.4 Implementation of actuation

For active flow control applications, the standard Galerkin model needs to be generalized to include the effects of actuation. For control purposes it is necessary to design a free control input to the model. If the actuation can be modelled as a volume force with finite support, a force term, say  $B(t)\mathbf{g}(\mathbf{x})$ , is simply added to the NS-equation. This leads to the following additional term in the Galerkin system

$$B(t)(\mathbf{g}(\mathbf{x}), \mathbf{u}_i(\mathbf{x}))_\Omega = B(t)g_i. \quad (2.42)$$

For (very) *local* periodic actuation, e.g. a zero-net-mass-flux actuator, the effect of actuation can be represented by an *equivalent* volume force term. The fluctuation part of the velocity field is decomposed into a boundary-imposed unsteadiness  $\mathbf{u}_{inhom}$  satisfying an inhomogeneous boundary condition and a flow response  $\mathbf{u}_{hom}$  satisfying a homogeneous boundary condition. The imposed unsteadiness  $\mathbf{u}_{inhom}$  is modelled by an actuation mode  $\mathbf{u}_{-1}(\mathbf{x})$  with amplitude  $a_{-1}(t)$  (Graham *et al.*, 1999) and the flow response, with homogeneous boundary conditions, by a linear combination of expansion modes (e.g., POD modes). This results in the Galerkin approximation

$$\mathbf{u}(\mathbf{x}, t) = \sum_{i=-1}^N a_i(t) \mathbf{u}_i(\mathbf{x}). \quad (2.43)$$

The choice of the actuation mode is a free design parameter, for which the literature offers many variants, see Kasnakoglu (2007) and the references therein. Here, a volume force term is considered that is consistent with an actuation mode ansatz under (nearly) periodic forcing. The actuation mode has two particularities: firstly, it is not necessarily orthogonal to the POD modes, and secondly, its amplitude is a control input. Substitution of (2.43) into the Navier-Stokes

---

<sup>1</sup>implementation of actuation is discussed below



equation and Galerkin projection onto the expansion modes yields (Noack *et al.*, 2004)

$$\dot{a}_i = -m_{i,-1} \dot{a}_{-1} + \nu \sum_{j=-1}^N l_{ij} a_j + \sum_{j,k=-1}^N q_{ijk} a_j a_k \quad \text{for } i = 1, \dots, N.$$

or, equivalently,

$$\begin{aligned} \dot{a}_i &= \nu \sum_{j=0}^N l_{ij} a_j + \sum_{j,k=0}^N q_{ijk} a_j a_k \\ &+ \left[ \nu l_{i,-1} + (q_{i,0,-1} + q_{i,-1,0}) + \sum_{j=1}^N (q_{i,j,-1} + q_{i,-1,j}) a_j \right] a_{-1} \\ &- m_{i,-1} \dot{a}_{-1}. \end{aligned} \quad (2.44)$$

Under non-actuated conditions,  $a_{-1} = \dot{a}_{-1} \equiv 0$ , the natural system is obtained.

For future reference, assume that a periodic actuator signal is given, where the velocity  $b = B \cos(\beta)$  satisfies  $d\beta/dt = \Omega^a$ , with a slowly varying amplitude  $B$  and phase shift  $\beta = \Omega^a t$ . The acceleration then reads  $db/dt = -\Omega^a B \sin(\beta)$ . The actuator command and its derivative are comprised in a vector

$$\mathbf{b} = \begin{bmatrix} b_1 \\ b_2 \end{bmatrix} = \begin{bmatrix} b \\ -\frac{db/dt}{\Omega^a} \end{bmatrix} = B \begin{bmatrix} \cos(\beta) \\ \sin(\beta) \end{bmatrix}. \quad (2.45)$$

The effect of the periodic actuation is modelled by an actuation mode  $\mathbf{u}_{-1}(\mathbf{x})$  with amplitude  $a_{-1}(t)$ , which yields an input matrix  $\mathbf{B}$  (see (2.44))

$$B_{i,1} = \nu l_{i,-1} + (q_{i,0,-1} + q_{i,-1,0}) + \sum_{j=1}^N (q_{i,j,-1} + q_{i,-1,j}) a_j, \quad (2.46a)$$

$$B_{i,2} = m_{i,-1} \Omega^a. \quad (2.46b)$$

Comparing (2.45) and (2.46) with (2.44) it follows that  $b_1 = a_{-1}$  and  $b_2 = -\dot{a}_{-1}/\Omega^a$ .

### Discussion

The design of actuation mode(s) generally is not without substantial difficulties. Firstly, in a POD of a forced flow field the effect of the actuation is hardwired

to the POD modes and hence cannot be freely chosen as input. Secondly, in the case of a very local actuation, the interaction between the local actuation and the globally dominant coherent structures is mediated by a succession of small structures and convective effects that the POD Galerkin framework is expressly designed to ignore (low energy events). The above approach addresses these problems by identifying the periodic actuation not with its immediate, local effect, but with locked-in forcing effects on globally synchronized coherent structures associated with dynamics at the actuation frequency (Tadmor *et al.*, 2004).

## 2.3 Mean-field modelling

Once a snapshot ensemble is available from a reference Navier-Stokes solution, the POD-Galerkin method can be applied to obtain a low-dimensional model of the flow field. Here, the standard POD basis is extended with so-called shift modes or mean-field corrections, that describe the change of the base flow (see § 2.1.3). This enriched basis is used to derive a Galerkin system governing the evolution of the temporal coefficients. The low-dimensional model that results is called the mean-field model.

The underlying ideas of mean-field theory trace back to Stuart (1958), and more recently, to Maurel *et al.* (1995); Sipp & Lebedev (2007) where the critical role of the time-varying base flow in nonlinear saturating instabilities is elaborated. For instance, when the Reynolds number is increased for the flow around a circular cylinder, the initially stable steady flow transitions to a von Kármán vortex street at  $Re \approx 47$ . This phenomenon can be mathematically described by a stable steady solution that becomes unstable and saturates in a stable limit cycle, see § 2.3.2. This transition is accompanied by a changed base flow and increased drag. Active flow control can be exploited to modify the base flow for the purpose of drag reduction or lift increasement (Luchtenburg *et al.*, 2009a; Pastoor *et al.*, 2008).

The mean-field model is derived by (1) considering an enriched Galerkin approximation (basis) that includes the mean-field correction, and (2) simplification of the Galerkin system to a weakly nonlinear form. The mechanics of the derivation of the latter are introduced by considering a weakly nonlinear oscillator in

§ 2.3.1. In § 2.3.2 a Galerkin mean-field model is derived for a system with one pronounced frequency, e.g. vortex shedding. The generalization to multiple frequencies is described in § 2.3.3.

### 2.3.1 Weakly nonlinear oscillator

Consider a weakly nonlinear oscillator of the following form (see e.g. Strogatz, 1994)

$$\ddot{x} + x + \epsilon h(x, \dot{x}, t) = 0, \quad (2.47)$$

where  $\dot{(\cdot)} = d/dt(\cdot)$ ,  $0 < \epsilon \ll 1$  and  $h(x, \dot{x}, t)$  is an arbitrary smooth function. Let  $y = -\dot{x}$ , then (2.47) can be rewritten as

$$\dot{x} = -y, \quad (2.48a)$$

$$\dot{y} = x + \epsilon h. \quad (2.48b)$$

When  $\epsilon = 0$ , the solution of (2.48) is

$$x(t) = A \cos(t + \psi), \quad (2.49a)$$

$$y(t) = A \sin(t + \psi). \quad (2.49b)$$

When  $0 < \epsilon \ll 1$ , the solution can still be expressed in the form (2.49) provided that  $A$  and  $\psi$  are slowly varying functions of  $t$ . Let

$$x(t) = A(t) \cos(t + \psi(t)), \quad (2.50a)$$

$$y(t) = A(t) \sin(t + \psi(t)), \quad (2.50b)$$

which requires the constraint

$$\dot{A} \cos(t + \psi) - A \dot{\psi} \sin(t + \psi) = 0, \quad (2.51)$$

determined by differentiation of (2.50a) and comparison of the result with (2.48a) and (2.50b). Differentiation of (2.50b) yields

$$\dot{y} = A[1 + \dot{\psi}] \cos(t + \psi) + \dot{A} \sin(t + \psi). \quad (2.52)$$

Substituting (2.52) and (2.50a) into (2.48b) and repeating constraint (2.51) gives the system

$$\begin{bmatrix} \sin(t + \psi) & \cos(t + \psi) \\ \cos(t + \psi) & -\sin(t + \psi) \end{bmatrix} \begin{bmatrix} \dot{A} \\ A\dot{\psi} \end{bmatrix} = \begin{bmatrix} \epsilon h \\ 0 \end{bmatrix}. \quad (2.53)$$

Solving for  $\dot{A}$  and  $A\dot{\psi}$  yields

$$\dot{A} = \epsilon h \sin(t + \psi), \quad (2.54a)$$

$$A\dot{\psi} = \epsilon h \cos(t + \psi). \quad (2.54b)$$

Hence  $A$  and  $\psi$  are slowly varying for  $0 < \epsilon \ll 1$ . Let the running average (see also (2.6)) be defined by

$$\bar{r}(t) = \frac{1}{T} \int_{t-T/2}^{t+T/2} r(\tau) d\tau, \quad (2.55)$$

where  $T$  is the period of one sinusoidal oscillation. Time averaging commutes with differentiation, i.e. Reynolds condition (2.4d) is satisfied

$$\frac{d\bar{r}}{dt} = \overline{\frac{dr}{dt}}. \quad (2.56)$$

Since  $A$  and  $\psi$  are slowly varying functions of the time, the system (2.54) is time-averaged

$$\overline{\dot{A}} = \overline{\epsilon h(A \cos(t + \psi), -A \sin(t + \psi), t) \sin(t + \psi)}, \quad (2.57a)$$

$$\overline{A\dot{\psi}} = \overline{\epsilon h(A \cos(t + \psi), -A \sin(t + \psi), t) \cos(t + \psi)}. \quad (2.57b)$$

Note that this result is exact, but not very helpful for solution of the problem. Therefore, the amplitude and phase are approximated by their time-averaged values. First, the amplitude is expanded in a Maclaurin series of  $\epsilon$

$$A(t, \epsilon) = A_0(t) + A_1(t)\epsilon + A_2(t)\epsilon^2 + \dots \quad (2.58)$$

Here  $A_0(t) = A(t, \epsilon = 0)$ , which means that  $A_0 = \bar{A}_0 = \text{const.}$  (compare with (2.54a)). Thus,

$$\begin{aligned} A(t) - \bar{A}(t) &= [A_0 - \bar{A}_0] + [A_1(t) - \bar{A}_1(t)]\epsilon + [A_2(t) - \bar{A}_2(t)]\epsilon^2 + \dots \\ &= 0 + O(\epsilon). \end{aligned} \quad (2.59)$$

Summarizing, we obtain the following approximation for  $A$  and  $\psi$

$$A(t) = \bar{A}(t) + O(\epsilon), \quad (2.60)$$

$$\psi(t) = \bar{\psi}(t) + O(\epsilon). \quad (2.61)$$

Now  $A$  and  $\psi$  are replaced by their time-averaged values

$$\dot{\bar{A}} = \overline{\epsilon h(\bar{A} \cos(t + \bar{\psi}), -\bar{A} \sin(t + \bar{\psi}), t) \sin(t + \bar{\psi})} + O(\epsilon^2), \quad (2.62a)$$

$$\bar{A} \dot{\bar{\psi}} = \overline{\epsilon h(\bar{A} \cos(t + \bar{\psi}), -\bar{A} \sin(t + \bar{\psi}), t) \cos(t + \bar{\psi})} + O(\epsilon^2), \quad (2.62b)$$

where the barred quantities are to be treated as constants inside the averages. It is customary to drop the overbars, since no distinction is normally made between slowly varying quantities and their averages. Equations (2.62) are the so-called averaged equations. The method is due to Kryloff & Bogoliuboff (1943) and is referred to as the method of averaging. The approximation can be improved by taking into account higher orders of  $\epsilon$ , which is done in the generalized method of averaging (Nayfeh, 1973).

### Van der Pol equation

As an example, the method of averaging is applied to the van der Pol equation (see e.g. Strogatz, 1994). This equation has for instance been used for vortex shedding modelling. The van der Pol equation is given by

$$\ddot{x} + x + \epsilon(x^2 - 1)\dot{x} = 0. \quad (2.63)$$

Comparison with (2.47) shows that  $h = (x^2 - 1)\dot{x} = (A^2 \cos^2 \theta - 1)(-A \sin \theta)$ , where  $\theta = t + \psi$ . Hence (2.62) becomes

$$\dot{\bar{A}} = \overline{\epsilon h \sin \theta} = \epsilon \left[ A \int_0^{2\pi} \sin^2 \theta d\theta - A^3 \int_0^{2\pi} \cos^2 \theta \sin^2 \theta d\theta \right] = \epsilon \left[ \frac{1}{2} A - \frac{1}{8} A^3 \right], \quad (2.64a)$$

$$A \dot{\bar{\psi}} = \overline{\epsilon h \cos \theta} = \epsilon \left[ A \int_0^{2\pi} \sin \theta \cos \theta d\theta - A^3 \int_0^{2\pi} \sin \theta \cos^3 \theta d\theta \right] = 0. \quad (2.64b)$$

Two numerical examples are now investigated. In figure 2.1(a) the exact solution (numerically obtained) for  $\epsilon = 0.1$  and initial conditions  $x(0) = 0.5$ ,

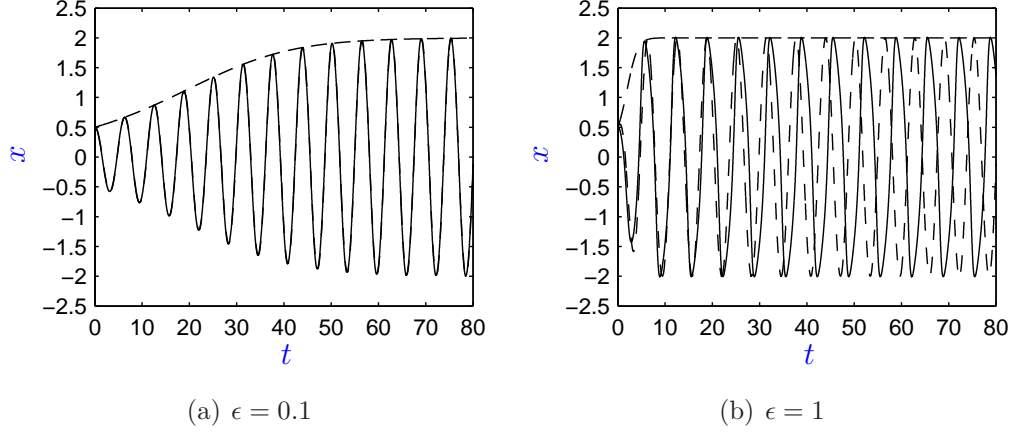


Figure 2.1: Comparison of the exact solution of the van der Pol equation (2.63) (—) with the approximate solution and the amplitude envelope (— · —) obtained by the method of averaging for different values of  $\epsilon$ .

$\dot{x}(0) = 0$  is compared with the result of the averaged equation (2.64a). The two curves are virtually indistinguishable and for comparison also the amplitude envelope predicted by (2.64a) is shown. In figure 2.1(b) the same result is shown, but now for  $\epsilon = 1$ . This case cannot be considered weakly-nonlinear and the rapid change in frequency is not described by (2.64b), although the amplitude envelope is reasonably described.

### 2.3.2 Mean-field model for single frequency

Using the same mechanics as in the previous section, the Galerkin mean-field model for a single frequency is derived from the Navier-Stokes equation. The reader is also referred to Noack *et al.* (2003) for an alternative derivation. The basis includes the steady solution  $\mathbf{u}_s$ , two modes that describe an oscillatory motion  $\{\mathbf{u}_{1,2}\}$  and a shift-mode  $\mathbf{u}_3$ , which represents the changing base flow. Thus, the Galerkin approximation is given by

$$\mathbf{u}(\mathbf{x}, t) = \mathbf{u}_s(\mathbf{x}) + a_1(t)\mathbf{u}_1(\mathbf{x}) + a_2(t)\mathbf{u}_2(\mathbf{x}) + a_3(t)\mathbf{u}_3(\mathbf{x}), \quad (2.65)$$

where  $\{a_{1,2}\}$  are the mode amplitudes of the oscillatory fluctuation and  $a_3$  is the amplitude of the shift mode. Substitution of expansion (2.65) in (2.38) and

application of the Galerkin projection (see § 2.2.3) yields the following form of the dynamic system for the amplitudes

$$\dot{a}_i = \nu \sum_{j=1}^3 l_{ij} a_j + \sum_{j=0}^3 \sum_{k=1}^3 q_{ijk} a_j a_k, \quad i = 1, 2, 3, \quad (2.66)$$

where:

$$l_{ij} = (\mathbf{u}_i, \Delta \mathbf{u}_j)_\Omega, \quad q_{ijk} = -(\mathbf{u}_i, \nabla \cdot (\mathbf{u}_j \otimes \mathbf{u}_k)), \quad i = 1, 2, 3, \quad j = 0, 1, 2, 3,$$

and  $\mathbf{u}_0 = \mathbf{u}_s$ . The system is split up in a linear and a nonlinear part

$$\dot{a}_1 = \sigma_1 a_1 - \omega_1 a_2 + \delta_1 a_3 + h_1(a_1, a_2, a_3), \quad (2.67a)$$

$$\dot{a}_2 = \omega_2 a_1 + \sigma_2 a_2 + \delta_2 a_3 + h_2(a_1, a_2, a_3), \quad (2.67b)$$

$$\dot{a}_3 = \rho_1 a_1 + \rho_2 a_2 + \sigma_3 a_3 + h_3(a_1, a_2, a_3), \quad (2.67c)$$

where the coefficients of the linear part are defined as

$$\sigma_i = \nu l_{ii} + q_{i0i} + q_{iii}, \quad i = 1, 2, 3, \quad (2.68a)$$

$$\omega_1 = \nu l_{12} + q_{102} + q_{120}, \quad \omega_2 = \nu l_{21} + q_{201} + q_{210}, \quad (2.68b)$$

$$\delta_i = \nu l_{i3} + q_{i03} + q_{i30}, \quad i = 1, 2, \quad (2.68c)$$

$$\rho_i = \nu l_{3i} + q_{3i0} + q_{30i}, \quad i = 1, 2, \quad (2.68d)$$

and the *weakly nonlinear* functions  $h_i$  are defined as

$$h_i = \sum_{j=1}^3 \sum_{k=1}^3 q_{ijk} a_j a_k. \quad (2.69)$$

Similarly to the weakly nonlinear oscillator in § 2.3.1, the solution is assumed to be given by

$$a_1 = A(t) \cos(\theta(t)), \quad (2.70a)$$

$$a_2 = A(t) \sin(\theta(t)), \quad (2.70b)$$

$$a_3 = D(t), \quad (2.70c)$$

## 2.3 Mean-field modelling

---

where the amplitudes  $A$ ,  $D$  and the phase  $\theta = \omega t + \psi(t)$  are slowly varying quantities. The time derivatives are

$$\dot{a}_1 = -A(\omega + \dot{\psi}) \sin(\theta) + \dot{A} \cos(\theta), \quad (2.71a)$$

$$\dot{a}_2 = A(\omega + \dot{\psi}) \cos(\theta) + \dot{A} \sin(\theta), \quad (2.71b)$$

$$\dot{a}_3 = \dot{D}. \quad (2.71c)$$

Substitution of (2.70) and (2.71) in (2.67a) and (2.67b) yields

$$\sin(\theta)[-A\omega - A\dot{\psi} - A\omega_1] + \cos(\theta)[\dot{A} - \sigma_1 A] = \delta_1 D + h_1, \quad (2.72a)$$

$$\sin(\theta)[\dot{A} - \sigma_2 A] + \cos(\theta)[A\omega + A\dot{\psi} - A\omega_2] = \delta_2 D + h_2. \quad (2.72b)$$

Equations (2.72a) and (2.72b) need to be consistent with each other. First consider the linear case without mean-field deformation, i.e.  $h_1 = h_2 \equiv 0$  and  $D \equiv 0$ . This implies that the frequency is constant  $\dot{\psi} \equiv 0$  and that the amplitude has a constant growth rate  $\sigma$ . Thus, for reasons of consistency

$$-\omega_1 = \omega_2 = \omega, \quad (2.73a)$$

$$\sigma_1 = \sigma_2 = \sigma. \quad (2.73b)$$

Note that these equations describe the *phase invariance* of a linear harmonic oscillator. Phase invariance requires that the system coefficients do not change under a rotation of the coordinate system.<sup>1</sup> Rewriting, (2.72) becomes

$$\begin{bmatrix} \cos(\theta) & -\sin(\theta) \\ \sin(\theta) & \cos(\theta) \end{bmatrix} \begin{bmatrix} \dot{A} - \sigma A \\ A\dot{\psi} \end{bmatrix} = \begin{bmatrix} \delta_1 D + h_1 \\ \delta_2 D + h_2 \end{bmatrix}. \quad (2.74)$$

Note that the matrix on the left-hand side is a rotation matrix. Solving (2.74) for  $\dot{A} - \sigma A$  and  $A\dot{\psi}$  yields

$$\dot{A} - \sigma A = [\delta_1 D + h_1] \cos(\theta) + [\delta_2 D + h_2] \sin(\theta) \quad (2.75a)$$

$$A\dot{\psi} = -[\delta_1 D + h_1] \sin(\theta) + [\delta_2 D + h_2] \cos(\theta). \quad (2.75b)$$

---

<sup>1</sup>Rewrite the system in operator notation:  $\mathcal{L}(\mathbf{a}) = \mathbf{0}$ , where  $\mathbf{a} = [a_1, a_2]^T$ . Then phase invariance implies that  $\mathcal{L}(\mathbf{R}\mathbf{a}) = \mathbf{0}$ , where  $\mathbf{R}$  is a rotation matrix with property  $\mathbf{R}^T \mathbf{R} = \mathbf{I}$ .



*Time-averaging* of (2.75) yields

$$\dot{\bar{A}} = \sigma \bar{A} + \overline{[\delta_1 D + h_1] \cos(\theta)} + \overline{[\delta_2 D + h_2] \sin(\theta)}, \quad (2.76a)$$

$$\overline{A \dot{\psi}} = -\overline{[\delta_1 D + h_1] \sin(\theta)} + \overline{[\delta_2 D + h_2] \cos(\theta)}. \quad (2.76b)$$

As above,  $A$ ,  $D$  and  $\psi$  are replaced by their time-averaged values. Substitution of (2.69) and (2.70) into (2.76) yields the simplified equations. As an example, the second term on the right hand side of (2.76a) is calculated:

$$\begin{aligned} \overline{[\delta_1 D + h_1] \cos(\theta)} &= \delta_1 \overline{D \cos(\theta)} + q_{111} \overline{A^2 \cos^3(\theta)} + q_{122} \overline{A^2 \sin^2(\theta) \cos(\theta)} \\ &\quad + q_{133} \overline{D^2 \cos(\theta)} + (q_{112} + q_{121}) \overline{A^2 \cos^2(\theta) \sin(\theta)} \\ &\quad + (q_{113} + q_{131}) \overline{AD \cos^2(\theta)} + (q_{123} + q_{132}) \overline{AD \sin(\theta) \cos(\theta)} \\ &= \frac{1}{2} (q_{113} + q_{131}). \end{aligned}$$

In summary, the simplified system (neglecting the bar for slowly varying quantities) reads as follows

$$\dot{A} = \sigma A - \beta AD, \quad (2.77a)$$

$$\dot{\psi} = \gamma D, \quad (2.77b)$$

where the coefficients are given by

$$\beta = -\frac{1}{2} (q_{113} + q_{131} + q_{223} + q_{232}), \quad (2.78a)$$

$$\gamma = \frac{1}{2} (-q_{123} - q_{132} + q_{213} + q_{231}). \quad (2.78b)$$

Similarly, substitution of (2.70) and (2.71) in (2.67c) and averaging yields

$$\dot{D} = \sigma_3 D + \alpha A^2 + \kappa D^2, \quad (2.79)$$

where the coefficients are given by

$$\alpha = \frac{1}{2} (q_{311} + q_{322}), \quad (2.80a)$$

$$\kappa = \frac{1}{2} q_{333}. \quad (2.80b)$$

The term of order  $D^2$  is neglected in the following (*linearized Reynolds equation*).

Summarizing, the time-averaged dynamic system in polar form reads

$$\dot{A} = \sigma A - \beta AD, \quad (2.81a)$$

$$\dot{\psi} = \gamma D, \quad (2.81b)$$

$$\dot{D} = -\mu D + \alpha A^2, \quad (2.81c)$$

where  $\mu = -\sigma_3$ . The corresponding Galerkin form of the model is given by

$$\dot{a}_1 = (\sigma - \beta a_3)a_1 - (\omega + \gamma a_3)a_2, \quad (2.82a)$$

$$\dot{a}_2 = (\omega + \gamma a_3)a_1 + (\sigma - \beta a_3)a_2, \quad (2.82b)$$

$$\dot{a}_3 = -\mu a_3 + \alpha(a_1^2 + a_2^2), \quad (2.82c)$$

where the system coefficients are defined by

$$\sigma = \frac{1}{2}(\nu l_{11} + q_{101} + q_{110}) + \frac{1}{2}(\nu l_{22} + q_{202} + q_{220}), \quad (2.83a)$$

$$\omega = -\frac{1}{2}(\nu l_{12} + q_{102} + q_{120}) + \frac{1}{2}(\nu l_{21} + q_{201} + q_{210}), \quad (2.83b)$$

$$\beta = -\frac{1}{2}(q_{113} + q_{131}) - \frac{1}{2}(q_{223} + q_{232}), \quad (2.83c)$$

$$\gamma = -\frac{1}{2}(q_{123} + q_{132}) + \frac{1}{2}(q_{213} + q_{231}), \quad (2.83d)$$

$$\mu = -(\nu l_{33} + q_{330} + q_{303}), \quad (2.83e)$$

$$\alpha = \frac{1}{2}(q_{311} + q_{322}). \quad (2.83f)$$

For the nonlinear part of the system, *phase invariance* is also required. This results in the following conditions on the coefficients

$$q_{113} + q_{131} = q_{223} + q_{232}, \quad (2.84a)$$

$$-q_{123} - q_{132} = q_{213} + q_{231}. \quad (2.84b)$$

Alternatively, the structure of the dynamic system (2.82) could have been derived from the polar formulation. Note that for this specific case the complete structure of the dynamical system (2.82) also solely follows from the requirement of phase invariance.

When the decay rate  $\mu$  in (2.81c) is about an order of magnitude greater than the growth rate  $\sigma$  in (2.81a), equation (2.81c) can be slaved to the latter (see e.g.

Haken, 1983), i.e. set  $\dot{D} = 0$ , solve for  $D$  and then substitute the result in (2.81a). This procedure yields the Landau (amplitude) equation

$$\dot{A} = \sigma A - \tilde{\beta} A^3, \quad (2.85)$$

where  $\tilde{\beta} = \beta\alpha/\mu$ . The corresponding evolution equation for the phase is given by

$$\dot{\psi} = \tilde{\gamma} A^2, \quad (2.86)$$

where  $\tilde{\gamma} = \gamma\alpha/\mu$ . Similarly, the slaved Galerkin model is of the form

$$\dot{a}_1 = (\sigma - \tilde{\beta}(a_1^2 + a_2^2))a_1 - (\omega + \tilde{\gamma}(a_1^2 + a_2^2))a_2, \quad (2.87a)$$

$$\dot{a}_2 = (\omega + \tilde{\gamma}(a_1^2 + a_2^2))a_1 + (\sigma - \tilde{\beta}(a_1^2 + a_2^2))a_2. \quad (2.87b)$$

In figure 2.2, a typical result obtained by integration of equations (2.81) and (2.82) is shown. The model coefficients are taken from Tadmor *et al.* (2004). This mean-field Galerkin model represents a least-order approximation of a natural transient leading to vortex shedding behind a circular cylinder. In the top plot of subfigure (a) the amplitude obtained by integration of the Landau equation (2.85) is shown for comparison (dashed line). The slaving principle yields a reasonable approximation. The bottom plot of subfigure (a) shows a change in frequency of about 30%.

### Discussion

The addition of the mean field correction to the standard basis, leads to a nonlinear coupling with the base flow in the averaged Galerkin system. These nonlinear terms effectuate a nonlinear saturation of the amplitude, which is clearly demonstrated by the example above. There are two steady solutions for this model: (1) an unstable fixed point at the origin and (2) a stable limit cycle given by  $A = \sqrt{\sigma\rho/\alpha\beta}$  and  $D = \sigma/\beta$ . This shows that the system (eventually) goes into oscillation of fixed amplitude and frequency, irrespective of the initial state. In contrast, if the mean-field correction is neglected, the oscillation amplitude is dependent on the initial conditions and small perturbations cause the system to depart.

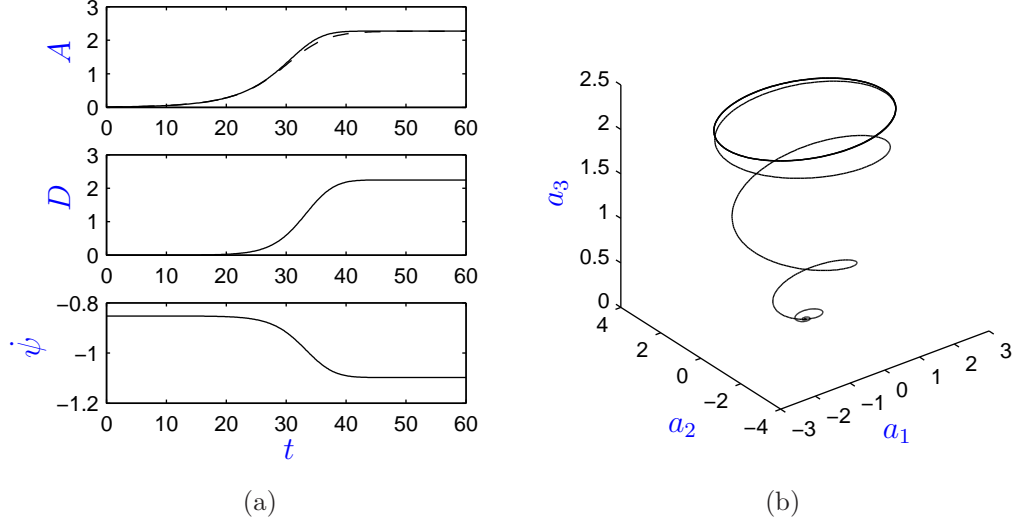


Figure 2.2: Integration of a mean-field model, see (2.81) and (2.82): the system in polar representation (a) and the phase space of the system in Galerkin form (b). The model coefficients are taken from Tadmor *et al.* (2004).

### 2.3.3 Mean-field model for two frequencies

In this section, a mean-field model for two frequencies is derived in an axiomatic fashion, starting from the Navier-Stokes equation. Here, we specifically target active flow control applications. It is assumed that a dominant periodic phenomenon associated with large coherent structures, like vortex shedding, can be suppressed or diminished by flow control. The actuator introduces new coherent structures that lock-in on the actuation frequency. The presence of a natural and (different) actuation frequency leads to a six state mean-field model with two shift modes. The axiomatic approach lends itself readily to the application of similar flow systems with multiple frequencies.

As a first element of mean-field theory, the ensemble average is introduced, see (2.3) and (2.4). As discussed above, an approximation of this Reynolds average may be the running average over a time period  $T$ ,

$$\bar{\mathbf{u}}(t) = \frac{1}{T} \int_{-\frac{T}{2}}^{\frac{T}{2}} \mathbf{u}(t + \tau) d\tau. \quad (2.88)$$

A discussion of this computation is provided in Appendix B.1.

It is assumed that the flow in its natural state is characterized by one dominant frequency. This frequency is associated with large coherent structures that typically correspond to vortex shedding in the wake of a body. By means of oscillatory actuation the flow is perturbed and after a (short) transient the flow locks in onto the actuation frequency and the coherent structures of the natural state diminish, i.e. flow control is effective in suppressing the natural instability. New structures appear that result from the periodic forcing and are accompanied by a modification of the mean flow. Hence, the following simplifying assumption is made.

**Assumption NSE 1 (A generalized Krylov-Bogoliubov ansatz)** *The velocity field is dominated by the sum of a slowly varying base flow and two oscillatory components which are nearly pure harmonics at the natural and the actuation frequency. Other temporal harmonics are negligible. Thus,*

$$\mathbf{u}(\mathbf{x}, t) = \mathbf{u}^B(\mathbf{x}, t) + \mathbf{u}^n(\mathbf{x}, t) + \mathbf{u}^a(\mathbf{x}, t), \quad (2.89)$$

where the superscripts  $B$ ,  $n$  and  $a$  are respectively used to denote terms related to the slowly varying base flow component, to oscillations at the natural shedding frequency, and to oscillations at the actuation frequency. Here,  $\mathbf{u}^B$  satisfies the steady, inhomogeneous boundary conditions,  $\mathbf{u}^n$  the homogenized version, and  $\mathbf{u}^a$  accounts for the residual to the unsteady boundary conditions, in particular, those associated with the actuation.

This ansatz implies — in analogy to the Reynolds decomposition — that the fluctuations have vanishing ensemble averages (compare with (2.3) and (2.4))

$$\overline{\mathbf{u}^B} = \mathbf{u}^B, \quad \overline{\mathbf{u}^n} = 0, \quad \overline{\mathbf{u}^a} = 0. \quad (2.90)$$

Following Dušek *et al.* (1994), the assumed slow variation of the mean flow and the oscillation amplitudes, frequencies and phase shifts can be formalized by introducing a small parameter  $\epsilon \ll 1$  and slowly varying amplitude functions  $\mathbf{u}_0^B$ ,  $\mathbf{u}_{1,2}^n$ ,  $\mathbf{u}_{1,2}^a$ , such that

$$\mathbf{u}^B(\mathbf{x}, t) = \mathbf{u}_0^B(\mathbf{x}, \epsilon t), \quad (2.91a)$$

$$\mathbf{u}^n(\mathbf{x}, t) = \mathbf{u}_1^n(\mathbf{x}, \epsilon t) \cos(\Omega^n t) + \mathbf{u}_2^n(\mathbf{x}, \epsilon t) \sin(\Omega^n t), \quad (2.91b)$$

$$\mathbf{u}^a(\mathbf{x}, t) = \mathbf{u}_1^a(\mathbf{x}, \epsilon t) \cos(\Omega^a t) + \mathbf{u}_2^a(\mathbf{x}, \epsilon t) \sin(\Omega^a t), \quad (2.91c)$$

where the angular frequency is defined as  $\Omega = 2\pi St$  with applicable superscripts ‘ $n$ ’ and ‘ $a$ ’ and the normalized frequency as Strouhal number  $St = f L/U_\infty$ , where  $f$  is the frequency,  $L$  a characteristic length and  $U_\infty$  the incoming flow velocity. The reciprocal of the small parameter, i.e.  $1/\epsilon$ , is assumed to be the characteristic time scale on which the amplitude functions change. This ansatz implies, for instance, that time derivatives of the amplitude functions are of order  $O(\epsilon)$ , which shall be neglected in the present discussion.

A second simplifying assumption is

**Assumption NSE 2 (A non-commensurability ansatz)** *There is no direct interaction between  $\mathbf{u}^n$  and  $\mathbf{u}^a$  via the quadratic Navier-Stokes term  $\nabla \cdot (\mathbf{u} \otimes \mathbf{u})$ .*

This assumption is based on the fact that the natural and actuated oscillations are not harmonically related by integral or half-integral ratios, i.e. they are not harmonics or subharmonics of each other. Also, on each of the two respective attractors, fluctuations in the other frequency are negligible.

The Krylov-Bogoliubov ansatz NSE 1 is substituted into the Navier-Stokes equation and the terms are sorted by the 0-th harmonic and the first harmonics at frequency  $St^n$  and  $St^a$ . Employing the above approximations yields

$$0 = \nabla \cdot (\mathbf{u}^B \otimes \mathbf{u}^B) + \nabla \cdot (\overline{\mathbf{u}^n \otimes \mathbf{u}^n}) + \nabla \cdot (\overline{\mathbf{u}^a \otimes \mathbf{u}^a}) + \nabla p^B - \nu \Delta \mathbf{u}^B, \quad (2.92a)$$

$$\partial_t \mathbf{u}^n = -\nabla \cdot (\mathbf{u}^n \otimes \mathbf{u}^B) - \nabla \cdot (\mathbf{u}^B \otimes \mathbf{u}^n) - \nabla p^n + \nu \Delta \mathbf{u}^n, \quad (2.92b)$$

$$\partial_t \mathbf{u}^a = -\nabla \cdot (\mathbf{u}^a \otimes \mathbf{u}^B) - \nabla \cdot (\mathbf{u}^B \otimes \mathbf{u}^a) - \nabla p^a + \nu \Delta \mathbf{u}^a + \mathbf{g}^a. \quad (2.92c)$$

Note that mixed quadratic terms such as  $\nabla \cdot (\mathbf{u}^a \otimes \mathbf{u}^n)$  are eliminated in all equations. In equation (2.92a), that elimination does not require assumption NSE 2 and can be obtained for  $St^n \neq St^a$  by the projection (B.1a), as explained in the Appendix.

In equations (2.92b, 2.92c), the simplifying assumption NSE 2 is invoked. The temporal behaviours of the quadratic terms  $\nabla \cdot (\mathbf{u}^B \otimes \mathbf{u}^B)$ ,  $\nabla \cdot (\mathbf{u}^n \otimes \mathbf{u}^n)$  and  $\nabla \cdot (\mathbf{u}^a \otimes \mathbf{u}^a)$  are characterized by the zero and respective second harmonics of the two frequencies. These terms are filtered out by the Krylov-Bogoliubov ansatz or can be filtered out by the windowed projections (B.1b) and (B.1c) in the Appendix. This explains the absence of these terms from (2.92b) and (2.92c).

The terms  $(\mathbf{u}^n \otimes \mathbf{u}^B)$ ,  $(\mathbf{u}^B \otimes \mathbf{u}^n)$ ,  $(\mathbf{u}^a \otimes \mathbf{u}^B)$  and  $(\mathbf{u}^B \otimes \mathbf{u}^a)$  are associated with time oscillations at the natural and actuated frequencies, and are therefore invariant under the respective projections.

Together, the three coupled equations (2.92) constitute mean-field equations at the Navier-Stokes equation level. Contrary to the original mean-field theory of Stuart (1958), weakly-nonlinear instability and closeness to the steady Navier-Stokes solution is not assumed.

The next two assumptions are made in preparation for the presentation of the reduced-order Galerkin model.

**Assumption NSE 3 (Phase invariance)** *The decomposition (2.89) is phase invariant. This means that the simplified dynamics (2.92) remains valid when  $\mathbf{u}^n(\mathbf{x}, t)$ ,  $\mathbf{u}^a(\mathbf{x}, t)$  and the actuation command  $b(t)$  are substituted by  $\mathbf{u}^n(\mathbf{x}, t + \tau_n)$ ,  $\mathbf{u}^a(\mathbf{x}, t + \tau_a)$  and  $b(t + \tau_a)$  for arbitrary time shifts  $\tau_n$  and  $\tau_a$ . The actuation command may be the amplitude of the volume force  $\mathbf{g}^a$  or the employed boundary actuator.*

Note that only relative time shifts between the three components are significant. Hence, there is no added generality if time shift also is allowed in the base flow (i.e. such a time shift can be factored out by shifting the entire time axis). This hypothesis is called *phase invariance* since time shifts are immediately translated to independent phase shifts of oscillations in the respective two frequencies. Arbitrary phase shifts between the actuation  $b$  and  $\mathbf{u}^a$  are not assumed, since  $\mathbf{u}^a$  is interacting with, and eventually locked in, onto the actuation. The phase invariance hypothesis is feasible due to the lack of direct, phase-dependent interactions between the two oscillatory flow components. It is often a reasonable approximation in POD models for vortex shedding phenomena. Phase-invariance assures that the averaging procedure implied in the simplified dynamics (2.92) yields meaningful results. Counter examples of non-phase-invariant systems are provided in Noack & Copeland (2000).

**Assumption NSE 4 (Linearized Reynolds equation)** *It is assumed that the Reynolds equation (2.92a) can be linearized around the steady solution  $\mathbf{u}^s$ . Let  $\mathbf{u}^B = \mathbf{u}^s + \mathbf{u}^\Delta$ . The linearized Reynolds equation for the mean-field correction*

$\mathbf{u}^\Delta$  is obtained by substitution into (2.92a), subtracting the steady Navier-Stokes equation and neglecting quadratic terms in  $\mathbf{u}^\Delta$ :

$$0 = \nabla \cdot (\mathbf{u}^s \otimes \mathbf{u}^\Delta) + \nabla \cdot (\mathbf{u}^\Delta \otimes \mathbf{u}^s) + \nabla \cdot \overline{(\mathbf{u}^n \otimes \mathbf{u}^n)} + \nabla \cdot \overline{(\mathbf{u}^a \otimes \mathbf{u}^a)} + \nabla p^\Delta - \nu \Delta \mathbf{u}^\Delta. \quad (2.93)$$

This assumption implies that there is a linear relationship between the Reynolds stresses and the mean-field correction. The mere purpose of this assumption is to simplify expressions in the Galerkin model that is presented in § 2.3.4. It is stressed that the results readily extend to the more general case, where the nonlinear Reynolds equation in its original form is considered. The price paid for that generality is the inclusion of higher-order terms in the expression for the mean-field correction.

### Discussion

Some significant observations associated with the mean-field equations (2.92) are highlighted in the following.

- (i) The dynamic base flow is effected by two independent Reynolds stresses (hence vector field orientations) yielding the volume forces  $\nabla \cdot \overline{(\mathbf{u}^n \otimes \mathbf{u}^n)}$  and  $\nabla \cdot \overline{(\mathbf{u}^a \otimes \mathbf{u}^a)}$ .
- (ii) In the un-actuated, natural flow,  $\mathbf{u}^a$  is negligible. In that case, the mean-field model highlights the dynamic interactions and energy exchange between the base flow  $\mathbf{u}^B$  and the periodic fluctuation  $\mathbf{u}' = \mathbf{u}^n$ . The latter induces a mean-field change  $\mathbf{u}^\Delta$  via the respective Reynolds stress term, whereas the former acts as either a stabilizing agent for high-level fluctuations or a destabilizing agent for a nearly steady flow, via the terms  $\nabla \cdot (\mathbf{u}^n \otimes \mathbf{u}^B + \mathbf{u}^B \otimes \mathbf{u}^n)$ . Over the attractor, the flow balances this two-way energy exchange with dissipation. This is the essence of the traditional mean-field model and the basis for the development of the mean-field Galerkin model by Noack *et al.* (2003).
- (iii) The mechanism by which  $\mathbf{u}^a$  interacts with the mean-field is structured in complete analogy to the natural instability. However, the fact that  $\mathbf{u}^a$  is



negligible without actuation suggests that the total power related to  $\mathbf{u}^a$  from production, dissipation, and convection alone acts as a sink and that actuation power is required to maintain the lock-in oscillation. In particular, the Reynolds stress due to  $\mathbf{u}^a$  gives rise to base flow changes that do not change this stabilizing, energy absorbing effect on  $\mathbf{u}^a$ .

- (iv) Of the three equations (2.92a), (2.92b) and (2.92c), the actuated unsteady boundary condition as well as volume force actuator effects directly only (2.92c). The actuation-induced oscillations in  $\mathbf{u}^a$  can interact with (and suppress) the instability at the natural frequency, only by using the varying base flow  $\mathbf{u}^B$  as a mediating agent. The Reynolds stress due to the excited  $\mathbf{u}^a$  changes  $\mathbf{u}^B$ , and the change in  $\mathbf{u}^B$  has a stabilizing effect on  $\mathbf{u}^n$ , despite the counter-acting effect of  $\mathbf{u}^n$  on  $\mathbf{u}^B$ , via its own Reynolds-stress contribution. This key observation therefore provides the sought mechanism for cross-frequency actuation. In particular, it explains the phase-independence of this stabilizing effect, hence the ability to suppress shedding with open-loop actuation.
- (v) It is straightforward to include more frequencies if the assumptions in § 2.3.3 hold correspondingly. From figure 2.3, this can be conceptualized by including a row that describes an additional ‘flow operating condition’ with corresponding oscillatory and shift-modes.
- (vi) The generalized mean-field model is a corollary of a more general framework predicting the first and second moments for a reduced-order model. This closure utilizes a finite-time thermodynamics formalism (Noack *et al.*, 2008) explaining a long-sought link to statistical physics.

The decomposition of the flow field into a base flow and two non-commensurable frequency contributions is formally very similar to the triple decomposition in Reynolds & Hussain (1972) into the base flow, the coherent-structure contribution and the stochastic contribution. Not surprisingly, the balance equations for the triple decomposition are equivalent at steady state condition.

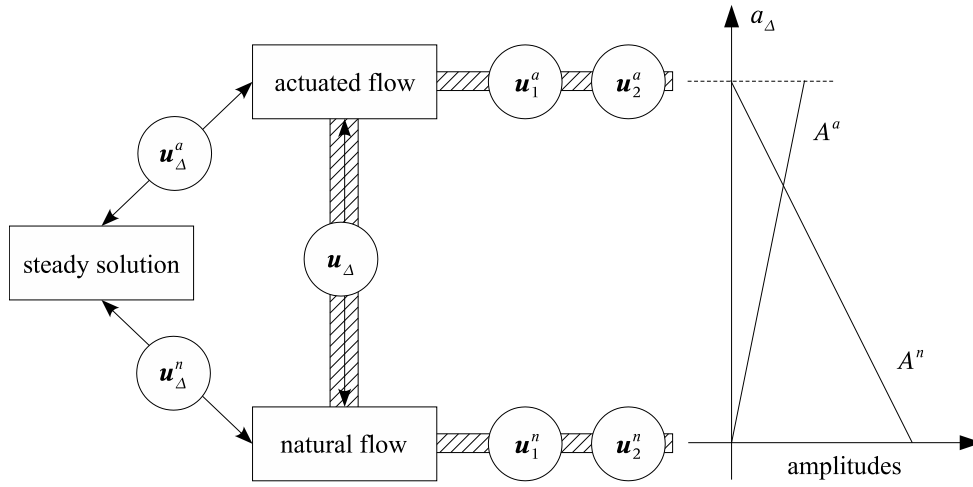


Figure 2.3: Principle sketch of the generalized mean-field model. The considered equilibrium flow states include the steady solution, natural and actuated flow (rectangles). The transitions are denoted by double arrows. The required Galerkin modes for each state are indicated by the circles. The hatched rectangles connect the modes employed for the transients between the natural and actuated flow. The amplitudes for slowly varying transition between both states are depicted in the right diagram.

### 2.3.4 Mean-field Galerkin model for two frequencies

In this section, the corresponding Galerkin model for the two-frequency mean-field model in § 2.3.3 is described. In accordance to the previous section, the flow is partitioned in a steady solution  $\mathbf{u}_s$ , 2 modes  $\{\mathbf{u}_1, \mathbf{u}_2\}$  resolving natural shedding at frequency  $\Omega^n$ , 2 modes  $\{\mathbf{u}_3, \mathbf{u}_4\}$  for the actuated state at frequency  $\Omega^a$ , and 2 shift modes  $\{\mathbf{u}_5, \mathbf{u}_6\}$  describing mean-field deformations due to both frequencies. The effect of actuation is modelled by a single actuation mode  $\mathbf{u}_{-1}$  (see § 2.2.4), which only directly influences modes 3 and 4. Thus, the Galerkin approximation reads

$$\mathbf{u}(\mathbf{x}, t) = a_{-1}(t)\mathbf{u}_{-1}(\mathbf{x}) + \underbrace{\sum_{i=1}^2 a_i(t)\mathbf{u}_i(\mathbf{x})}_{\mathbf{u}^n(\mathbf{u}, t)} + \underbrace{\sum_{i=3}^4 a_i(t)\mathbf{u}_i(\mathbf{x})}_{\mathbf{u}^a(\mathbf{u}, t)} + \underbrace{\sum_{i=5}^6 a_i(t)\mathbf{u}_i(\mathbf{x})}_{\mathbf{u}^B(\mathbf{u}, t)} + \mathbf{u}_s(\mathbf{x}). \quad (2.94)$$

The least-order Galerkin system is obtained by substitution of this approximation into the mean-field Navier-Stokes equations (2.92b), (2.92c), (2.93), followed by a Galerkin projection of these equations onto the expansion modes. Table 2.2 illustrates the derivation of the Galerkin system. In particular, the Galerkin system corresponding to the mean-field equation (2.92b) is presented in table 2.2. The remaining four equations are derived in a similar fashion.

The complete Galerkin system can be summarized in vector notation,

$$\frac{d}{dt}\mathbf{a}^n = \mathbf{L}(\mathbf{a}^n) + \mathbf{Q}(\mathbf{a}^B, \mathbf{a}^n) + \mathbf{Q}(\mathbf{a}^n, \mathbf{a}^B), \quad (2.95a)$$

$$\frac{d}{dt}\mathbf{a}^a = \mathbf{L}(\mathbf{a}^a) + \mathbf{Q}(\mathbf{a}^B, \mathbf{a}^a) + \mathbf{Q}(\mathbf{a}^a, \mathbf{a}^B) + \mathbf{B} \mathbf{b}, \quad (2.95b)$$

$$0 = \mathbf{L}(\mathbf{a}^B) + \overline{\mathbf{Q}(\mathbf{a}^n, \mathbf{a}^n)} + \overline{\mathbf{Q}(\mathbf{a}^a, \mathbf{a}^a)}, \quad (2.95c)$$

where  $\mathbf{a}^n = [a_1, a_2]^T$ ,  $\mathbf{a}^a = [a_3, a_4]^T$ ,  $\mathbf{a}^B = [a_5, a_6]^T$ ,  $\mathbf{B}$  is a  $2 \times 2$  matrix defined by (2.46) and  $\mathbf{b}$  a vector containing the actuator signal and its derivative, see (2.45).

In Appendix B.2 it is shown that under the current assumptions and the assumption of phase invariance (NSE 3) the mean-field Galerkin system has the

NSE (2.92b)	GS
$\partial_t \mathbf{u}^n =$	$\frac{d}{dt} a_i =$ <span style="float: right;"><math>i \in \mathcal{J}</math></span>
$-\nabla \cdot [\mathbf{u}^n \otimes \mathbf{u}^B]$	$\sum_{j \in \mathcal{J}} \sum_{k \in \mathcal{K}} q_{ijk} a_j a_k$
$-\nabla \cdot [\mathbf{u}^B \otimes \mathbf{u}^n]$	$+ \sum_{j \in \mathcal{K}} \sum_{k \in \mathcal{J}} q_{ijk} a_j a_k$
$+\nu \Delta \mathbf{u}^n$	$+ \nu \sum_{j=1}^2 l_{ij} a_j$
$-\nabla p^n$	$+ 0$

Table 2.2: Projection of the mean-field Navier-Stokes equation (2.92b) (NSE) to form the Galerkin system (GS) using the least-order approximation (2.94). In the first column the terms of the NSE are provided and in the second one the corresponding GS counterparts. The employed index sets are  $\mathcal{J} = \{1, 2\}$  and  $\mathcal{K} = \{5, 6\}$ .

following structure:

$$\frac{d}{dt} \begin{bmatrix} a_1 \\ a_2 \\ a_3 \\ a_4 \end{bmatrix} = \begin{bmatrix} \tilde{\sigma}^n & -\tilde{\omega}^n & 0 & 0 \\ \tilde{\omega}^n & \tilde{\sigma}^n & 0 & 0 \\ 0 & 0 & \tilde{\sigma}^a & -\tilde{\omega}^a \\ 0 & 0 & \tilde{\omega}^a & \tilde{\sigma}^a \end{bmatrix} \begin{bmatrix} a_1 \\ a_2 \\ a_3 \\ a_4 \end{bmatrix} + \begin{bmatrix} 0 & 0 \\ 0 & 0 \\ \kappa & -\lambda \\ \lambda & \kappa \end{bmatrix} \mathbf{b}, \quad (2.96)$$

where the state dependent coefficients are of the form

$$\begin{aligned} \tilde{\sigma}^n &= \sigma^n - \sigma^{n,n} (A^n)^2 - \sigma^{n,a} (A^a)^2, \\ \tilde{\omega}^n &= \omega^n + \omega^{n,n} (A^n)^2 + \omega^{n,a} (A^a)^2, \\ \tilde{\sigma}^a &= \sigma^a - \sigma^{a,n} (A^n)^2 - \sigma^{a,a} (A^a)^2, \\ \tilde{\omega}^a &= \omega^a + \omega^{a,n} (A^n)^2 + \omega^{a,a} (A^a)^2, \end{aligned} \quad (2.97)$$

and  $A^n = \|\mathbf{a}^n\|$  and  $A^a = \|\mathbf{a}^a\|$  are the respective oscillation amplitudes. Without the linearization assumption NSE 4, the parameters are represented by a Taylor series in  $(A^n)^2$  and  $(A^a)^2$ .

Alternatively, the mean-field model (2.96) can be formulated in polar coordinates. The natural fluctuation  $\mathbf{a}^n$  is characterized by the amplitude  $A^n$  and phase  $\alpha^n$ . Similarly, polar coordinates of the forced fluctuation  $\mathbf{a}^a$  are the amplitude  $A^a$  and phase  $\alpha^a$ . Thus,

$$\begin{aligned} \mathbf{a}^n &= A^n [\cos(\alpha^n) \mathbf{e}_1 + \sin(\alpha^n) \mathbf{e}_2], \\ \mathbf{a}^a &= A^a [\cos(\alpha^a) \mathbf{e}_3 + \sin(\alpha^a) \mathbf{e}_4], \end{aligned} \quad (2.98)$$

where  $\mathbf{e}_i \stackrel{\text{def}}{=} [\delta_{i,1}, \dots, \delta_{i,N}]^T$  is a unit vector in the  $i$ -th direction. The control command  $\mathbf{b}$  acts in the evolution equation (2.95b) only on the forced fluctuation, hence

$$\mathbf{b} = B [\cos(\beta) \mathbf{e}_3 + \sin(\beta) \mathbf{e}_4].$$

Finally, by Observation B.2.3 in the Appendix, the matrix  $\mathbf{B}$  can be written in the form

$$\mathbf{B} = g \begin{bmatrix} \cos(\theta) & -\sin(\theta) \\ \sin(\theta) & \cos(\theta) \end{bmatrix}. \quad (2.99)$$

Using these notations, the polar form of (2.96) is given by

$$\frac{dA^n}{dt} = \tilde{\sigma}^n A^n, \quad (2.100a)$$

$$\frac{d\alpha^n}{dt} = \tilde{\omega}^n, \quad (2.100b)$$

$$\frac{dA^a}{dt} = \tilde{\sigma}^a A^a + gB \cos(\beta + \theta - \alpha^a), \quad (2.100c)$$

$$\frac{d\alpha^a}{dt} = \tilde{\omega}^a + \frac{gB}{A^a} \sin(\beta + \theta - \alpha^a), \quad (2.100d)$$

where the state dependencies of  $\tilde{\sigma}^n$ ,  $\tilde{\sigma}^a$ ,  $\tilde{\omega}^n$  and  $\tilde{\omega}^a$  are defined in (2.97).

## 2.4 Control design

Targeting active flow control, the generalized mean-field model for two frequencies (2.100) is used to design a controller. The control goal in the current work is set-point tracking of a scalar, like drag or lift. The form of the goal functional is based on (2.93) and (2.95c) and provides an approximation for the time-averaged force:

$$y = y_0 + c_1(A^n)^2 + c_2(A^a)^2. \quad (2.101)$$

The control problem is to design a controller  $B = B(t)$ , such that  $y$  tracks a reference signal  $y_{ref}$ . In the following section, the sliding mode control approach is described that can be used to this end.

### 2.4.1 Sliding mode control

Sliding mode control (SMC) is a nonlinear control method and a special case of variable structure control. This control method is an appropriate robust method for systems, in which model inaccuracies, parameter variations and disturbances are present. The idea is to force the trajectory of the states toward a designed attractor, the so-called sliding surface, and once reached, the states are forced to remain on that surface and approach the steady state. The reader is referred to Slotine & Li (1991) for more detailed information on SMC. Below, a simplified version of SMC is considered.

The control goal in the current study is set-point tracking of a scalar. Therefore, the sliding surface  $s = 0$  is chosen such that the deviation from the set-point equals zero, i.e.

$$s = y - y_{ref}. \quad (2.102)$$

Suppose that the sliding surface is reached, then the trajectories are forced to slide along this surface, which implies that  $ds/dt = 0$ . From this requirement the equivalent control law is derived. Using (2.101), with  $y_{ref} = \text{const.}$ , the dynamic system (2.100), and setting  $ds/dt = 0$  yields

$$0 = c_1 A^n \frac{dA^n}{dt} + c_2 A^a \frac{dA^a}{dt} = c_1 \tilde{\sigma}^n (A^n)^2 + c_2 A^a (\tilde{\sigma}^a A^a + gB \cos(\beta + \theta - \alpha^a)). \quad (2.103)$$

Thus, the equivalent control law that holds the trajectory at the manifold  $s = 0$  is

$$B_{eq} = \frac{-1}{g \cos(\beta + \theta - \alpha^a)} \left( \frac{c_1 \tilde{\sigma}^n (A^n)^2}{c_2 A^a} + \tilde{\sigma}^a A^a \right). \quad (2.104)$$

To guarantee stability of the sliding surface, a corrective control must be added that will bring the system back to  $s = 0$  whenever  $s \neq 0$ . Consider the Lyapunov function  $V = (1/2)s^2$ . For stability it is required that  $dV/dt = s\dot{s} < 0$ . This stability can be achieved by adding a switch term to the equivalent control law. Hence, the complete control law is given by

$$B_{sm} = B_{eq} - K \text{sign}(s), \quad (2.105)$$

where  $K > 0$  and  $\text{sign}$  is the sign function

$$\text{sign}(s) = \begin{cases} 1 & \text{if } s > 0 \\ 0 & \text{if } s = 0 \\ -1 & \text{if } s < 0. \end{cases}$$

Because of imperfections in switching devices and delays, SMC may exhibit high frequency oscillations due to the sign function. This is called chattering. Therefore, in practice, the sign function is replaced by a saturation function with boundary layer width  $\psi$

$$\text{sat}\left(\frac{s}{\psi}\right) = \begin{cases} 1 & \text{if } s > \psi \\ \frac{s}{\psi} & \text{if } |s| \leq \psi \\ -1 & \text{if } s < -\psi. \end{cases}$$

In this case the control law changes to

$$B_{sm} = B_{eq} - K \text{sat}\left(\frac{s}{\psi}\right). \quad (2.106)$$

This amounts to a reduction of the control gain inside the boundary layer and results in a smoother control signal.

# Chapter 3

## Stabilization of the circular cylinder wake

### 3.1 Abstract

Low-dimensional models are crucial enablers for practical flow control. The proper orthogonal decomposition (POD) is commonly used for this purpose. Traditionally, POD modes are obtained at one operating condition. While the kinematics of the reference simulation are resolved by this model, the dynamic envelope is limited. Parameterized POD (pPOD) extends the POD procedure by employing PODs at several operating conditions. The result is a collection of mode sets. The flow is described in dependence of a parameter that relates the current flow state to an indexed (or interpolated) mode set. Knowledge of the flow state is crucial for control. The parameterized POD is also used to optimize the sensor positions such that an even performance throughout the entire dynamic range is assured. These concepts are demonstrated in the benchmark of stabilization of the wake flow behind a circular cylinder.

---

Published in: [Lehmann \*et al.\* \(2005\)](#); [Luchtenburg \*et al.\* \(2006\)](#).



## 3.2 Introduction

POD-Galerkin models (Holmes *et al.*, 1998) provide efficient approximations of flow data, but are typically fragile away from the reference attractor or orbit (see also the discussion in § 2.2.1). This is particularly detrimental for control design, where representation of transients is essential

A key challenge for the representation of transient dynamics, away from a single reference orbit, is that dominant flow structures tend to change significantly as the system traverses such trajectories. Referring to the driving example of this study, the 2D laminar cylinder wake, characteristics of such changes include a substantial shortening of the recirculation bubble of the mean flow, shorter vortex shedding periods and spatial wave length of the von Kármán vortices, as the system transitions from the unstable steady flow to the natural vortex shedding limit cycle (Noack *et al.*, 2003). A second challenge is posed by the generation of flow structures that are not present in the natural flow, which are introduced by actuation, especially under higher gains. This is reflected by the need to include up to 40 modes in a Galerkin model used for optimal control of this system (Bergmann *et al.*, 2004), whereas only three modes suffice for a least-order representation of natural transients (Noack *et al.*, 2003).

Here, the goal is to retain low dimension in flow models without losing the necessary dynamic range. Under (low gain) actuation the wake flow changes continuously, while the POD model at intermediate attractors often maintains both the same small number of leading modes, their main topological features and key dynamic properties of the local Galerkin system. Therefore, the idea of parameterized or interpolating models is employed. The flow is described in dependence of a (tuning) parameter that relates the current flow state to an indexed mode set. The interpretation of the dynamic state of the Galerkin system as a vector of temporal coefficients of a fixed set of expansion modes is thus adjusted as the system traverses transient trajectories and moves from the domain of one local model to the next. This framework maintains high model fidelity along transients by allowing the Galerkin system to benefit from a large number (ideally, a continuum) of expansion modes, while preserving a local low order. Following previous work (Noack *et al.*, 2003; Tadmor *et al.*, 2004), the flow

is described by a three state mean-field model. The model resolves changes in the mean flow and von Kármán vortex shedding. This mean-field model is described in more detail in § 2.3.2.

The advantage of the interpolated model over the standard POD model is demonstrated with respect to closed-loop flow control. The parameterized model is also used to assure an even performance of the sensors throughout the transient range, rather than in a narrow neighbourhood of the natural attractor.

## 3.3 Numerical simulation

In this section, the benchmark simulation of the flow around a circular cylinder is outlined, including the configuration (§ 3.3.1) and the simulation (§ 3.3.2).

### 3.3.1 Configuration

We study the laminar two-dimensional flow in the circular cylinder wake. The wake is characterized by a laminar instability at  $Re \approx 47$  (based on the cylinder diameter  $D$ ). At this Reynolds number the recirculation bubble, formed by a symmetric pair of vortices, cannot longer be sustained and the vortices break away, leading to the so-called von Kármán vortex street. Here, the flow is considered at  $Re = 100$ . A common design objective (Detemple-Laake & Eckelmann, 1989; Roussopoulos, 1993; Strykowski & Sreenivasan, 1990; Unal & Rockwell, 1987) is to suppress the wake instability which causes mechanical vibrations and increased drag. Figure 3.1 provides a schematic of the configuration. The streamlines represent the natural flow.

Actuation is implemented by a vertical volume-force in the wake. The support of this volume force is defined by

$$S = \{\mathbf{x} \in \Omega : \|\mathbf{x} - \mathbf{x}_{vf}\|^2 \leq D^2\}, \quad (3.1)$$

where  $\mathbf{x}_{vf} = (2D, 0)$  is at the center of the supporting disk and  $\Omega \subset \mathbb{R}^2$  denotes the computational domain defined in § 3.3.2. The volume force is given by

$$\mathbf{F}_{vf}(\mathbf{x}, t) = B(t)\mathbf{g}(\mathbf{x}), \quad (3.2)$$

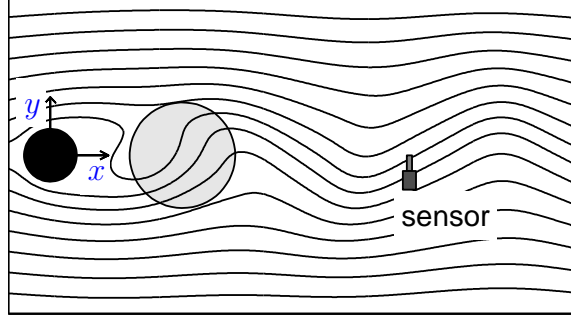


Figure 3.1: Principal sketch of the actuated cylinder wake. The cylinder is represented by the black disk. The location of the volume-force actuator is indicated by a grey circle. Streamlines represent the natural flow. The figure includes a vertical velocity sensor at  $(x, y) = (6.8D, 0)$ .

where  $B(t)$  is the time-dependent amplitude and

$$\mathbf{g}(\mathbf{x}) = \begin{bmatrix} 0 \\ 1 \end{bmatrix}, \quad \mathbf{x} \in S. \quad (3.3)$$

The sketch also includes a vertical velocity sensor at  $(x, y) = (6.8D, 0)$ .

### 3.3.2 Simulation

The two-dimensional laminar flow around the circular cylinder is computed by direct numerical simulation (DNS) of the Navier-Stokes equation. The finite-element Navier-Stokes solver is third-order accurate in space and time and is based on a pseudo-pressure formulation. The numerical data used here have been obtained with the numerical code *UNS3* developed by Prof. M. Morzyński at the Poznan University of Technology (Morzyński, 1987). The computational domain  $\Omega$  for the flow is the exterior of the cylinder  $x^2 + y^2 \geq (D/2)^2$  in the rectangle  $-5D \leq x \leq 15D$ ,  $-5D \leq y \leq 5D$ . The flow is discretized as finite elements on a triangular mesh (8712 points). The average lengths of the triangular mesh elements are  $0.058D$  near the cylinder,  $0.066D$  on the wake centerline  $x > 0.5D$ ,  $y = 0D$ , and  $0.104D$  in the whole domain. Each mesh element is subdivided in four similar subtriangles the vertices of which serve as nodes for the flow variables. For more details, see Noack *et al.* (2003) and the references therein.

## 3.4 Actuation strategy

The objective in the current study is suppression of the wake instability. The design problem is how to adjust the amplitude  $B(t)$  of the volume force  $B(t)\mathbf{g}(\mathbf{x})$  such that the wake is stabilized (as good as possible). The controller is physically motivated in § 3.4.1 and derived from a mean-field model in § 3.4.2.

### 3.4.1 Physically motivated control

A simple, physically motivated control policy is to apply actuation as a dissipative deceleration force. This strategy amounts to minimization of the kinetic energy of the fluctuations. The kinetic energy rate due to the volume force is given by

$$E_{vf}(t) = B(t) \int_{\Omega} \mathbf{g}(\mathbf{x}) \cdot \mathbf{u}'(\mathbf{x}, t) dV = B(t) (\mathbf{g}, \mathbf{u}')_{\Omega}(t). \quad (3.4)$$

The controller always extracts energy if

$$B(t) = -k (\mathbf{g}, \mathbf{u}')_{\Omega}(t), \quad (3.5)$$

with  $k > 0$ . The actuation force then reads

$$\mathbf{F}_{vf}(\mathbf{x}, t) = -k (\mathbf{g}, \mathbf{u}')_{\Omega}(t) \mathbf{g}(\mathbf{x}). \quad (3.6)$$

This form directly shows the nature of the force: it acts as an opposition control. The weighted vertical velocity on the support of the volume force is counteracted by the volume force.

The projection  $(\mathbf{g}, \mathbf{u}')_{\Omega}(t)$  is approximately proportional to  $v_{vf}(t)$ , where  $v_{vf}$  is the velocity at the center of the volume-force (§ 3.3.1). Thus a sensor in the center of the volume force can be used as a surrogate quantity to approximate the projection. In this case, the control amplitude is given by

$$B(t) = -\tilde{k} v_{vf}(t), \quad (3.7)$$

where  $\tilde{k} > 0$ .

### 3.4.2 Control design with a mean-field model

The actuation strategy can also be deduced from the mean-field Galerkin model of the natural flow. This model is described in § 2.3.2. It is a three state model that describes the periodic vortex shedding and changes in the mean flow. For the sake of convenience, the Galerkin approximation is repeated:

$$\mathbf{u}(\mathbf{x}, t) = \mathbf{u}_s(\mathbf{x}) + a_1(t)\mathbf{u}_1(\mathbf{x}) + a_2(t)\mathbf{u}_2(\mathbf{x}) + a_3(t)\mathbf{u}_3(\mathbf{x}), \quad (3.8)$$

where  $\mathbf{u}_s$  is the steady solution,  $\{\mathbf{u}_{1,2}\}$  are two POD modes that describe the oscillatory motion, and  $\mathbf{u}_3$  is a shift-mode, which represents the changing mean flow. The shift mode is defined as

$$\mathbf{u}_3 = (\mathbf{u}_0 - \mathbf{u}_s) / \|\mathbf{u}_0 - \mathbf{u}_s\|_\Omega, \quad (3.9)$$

where  $\mathbf{u}_0$  is the time-averaged velocity field of the natural flow. Time dependency of the periodic oscillation is described by the pair of amplitudes  $(a_1, a_2)$  and of the mean field by  $a_3$ . Incorporation of the volume  $B(t)\mathbf{g}(\mathbf{x})$  into the Navier-Stokes equation leads to additional terms of the form  $B(t)g_i$  in the Galerkin system (see (2.42)). Hence, the Galerkin system is given by

$$\dot{a}_1 = (\sigma - \beta a_3)a_1 - (\omega + \gamma a_3)a_2 + Bg_1, \quad (3.10a)$$

$$\dot{a}_2 = (\omega + \gamma a_3)a_1 + (\sigma - \beta a_3)a_2 + Bg_2, \quad (3.10b)$$

$$\dot{a}_3 = -\rho a_3 + \alpha(a_1^2 + a_2^2) + Bg_3, \quad (3.10c)$$

where  $g_i = (\mathbf{g}, \mathbf{u}_i)_\Omega$  and  $g_3 = 0$  because of the symmetry of the shift mode. In polar coordinates, the system is given by

$$\begin{bmatrix} \dot{A} \\ \dot{a}_3 \end{bmatrix} = \begin{bmatrix} \sigma & -\beta A \\ \alpha A & -\rho \end{bmatrix} \begin{bmatrix} A \\ a_3 \end{bmatrix} + b \begin{bmatrix} \cos(\theta - \phi) \\ 0 \end{bmatrix} B, \quad (3.11a)$$

$$\dot{\phi} = \omega + \gamma a_3 + \frac{b}{A} \sin(\theta - \phi) B, \quad (3.11b)$$

where  $\phi = \arg(a_1 + \imath a_2)$ ,  $\theta = \arg(g_1 + \imath g_2)$  and  $b = \sqrt{g_1^2 + g_2^2}$ . The actuation effect on the radius  $A$  and phase  $\phi$  is most easily inferred by considering the average effect over one period  $T$  of the system:

$$\frac{b}{T} \int_0^T \cos(\theta - \phi) B(t) dt, \quad \frac{b}{AT} \int_0^T \sin(\theta - \phi) B(t) dt.$$

This reveals that the actuation force that reduces the amplitude of the oscillation and has negligible effect on the oscillation frequency must be in phase with  $-\cos(\theta - \phi)$  (Tadmor *et al.*, 2003). Thus, the actuation amplitude is

$$B(t) = -k \cos(\theta - \phi), \quad (3.12)$$

where  $k > 0$ . Using the Galerkin approximation for the fluctuating velocity field

$$\mathbf{u}'(\mathbf{x}, t) = a_1(t)\mathbf{u}_1(\mathbf{x}) + a_2(t)\mathbf{u}_2(\mathbf{x}), \quad (3.13)$$

it follows that the energy extraction rate of the actuator can be approximated as

$$B(t) (\mathbf{g}, \mathbf{u}')_{\Omega}(t) \approx B(t) (a_1 g_1 + a_2 g_2) = B(t) bA \cos(\theta - \phi). \quad (3.14)$$

Indeed, this expression is of the same form as in (3.11a). This result together with (3.12) imply that any admissible control policy is bound to (roughly) imitate the simple physics based, dissipative policy suggested in § 3.4.1.

## 3.5 Parameterized POD

In this section, the parameterized POD procedure is outlined. The approach is motivated in § 3.5.1. The collection of POD mode sets is discussed in § 3.5.2. Full information control based on a parameterized POD model is shown in § 3.5.3.

### 3.5.1 Motivation

To understand the limitation on the effectiveness of the POD based control, it is useful to consider figure 3.2. The plots in that figure are based on results of three simulations, represented by the three rows. The top row displays the natural flow and the middle and bottom row show the result of two controlled flows that are obtained by the dissipative control discussed in § 3.4.1, with a moderate and a more aggressive feedback gain, respectively. For each simulation the figure includes, from left to right, the mean flow field and the first oscillatory POD mode. While the topological characteristics of all three flow conditions are similar, they exhibit significant mutual deformations: the recirculation bubble is gradually elongated and the vortical structures are pushed downstream as the

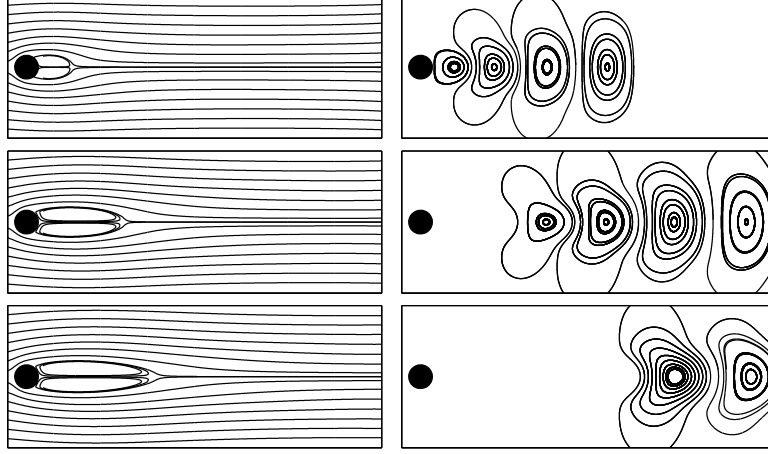


Figure 3.2: Comparison of the streamlines of a natural (top row), moderately forced (middle row) and aggressively forced (bottom row) flow field. Left: time-averaged flow and right: first POD mode.

flow is stabilized. In the context of opposition control, the changes in the values of  $g_i = (\mathbf{g}, \mathbf{u}_i)_\Omega$ , hence of the angle  $\theta = \arg(g_1 + \imath g_2)$  are critical. This change reflects the dynamic impact of the volume force. In addition, the definition of the flow phase  $\phi(t) = \arg(a_1(t) + \imath a_2(t))$  in terms of the leading POD modes changes. When only the POD modes of the natural attractor are employed, both the value of  $\theta$  and the definition of  $\phi(t)$  that are used to determine the actuation signal become increasingly wrong as vortex shedding is attenuated. Eventually, these errors reach a level at which the actuation  $B \propto \cos(\theta - \phi)$  is so out of phase that it loses its effectiveness. A model providing an effective solution to this problem must therefore account for the change in dominant modes along transients (Lehmann *et al.*, 2005).

### 3.5.2 Collection of mode sets

As discussed above, there is topological similarity between the natural flow and forced flow fields (see figure 3.2). This observation suggests that the similarity can be exploited for a parameterized representation of the flow field. First, velocity snapshots of the natural flow are computed. These snapshots are used to calculate the decomposition (3.8) for the natural flow. Second, velocity snapshots are

computed using feedback control. The feedback control law is defined by (3.7):  $B(t_{k+1}) = -kv_{vf}(t_k)$ , i.e. the control input at time  $t_{k+1}$  is proportional to the vertical velocity at the center of the volume force at the previous time step  $t_k$ . For several escalated values of the gain  $k$ , snapshot ensembles are calculated. Once the actuated flow is locked-in, the snapshots are post-processed to extract the first two POD modes. This procedure yields two (local) POD modes for each separate reference simulation. These POD mode sets can be parameterized by an index parameter  $p$  (parameterized POD). In the following, we will use the index  $p = 1$  for the natural flow and higher indices  $p = 2, \dots$  for mode sets obtained from feedback controlled flows, where a higher index indicates a higher value of the gain  $k$  in the control law.

The phase portraits corresponding to the parameterized POD (pPOD) mode sets are shown in figure 3.3 by lightly dotted circles. Controlled transients, with *slow* changes in the perturbation level, progress along the manifold connecting these cycles. The dynamics near each of the cycles is dominated by the shift mode  $\mathbf{u}_3$  and two locally extracted oscillatory modes  $\{\mathbf{u}_1, \mathbf{u}_2\}$ . The Galerkin systems obtained by projecting the NSE (2.2) onto these local modes are each of the form (3.11), albeit with different coefficients. The local values of the Galerkin system coefficients are functions of the characteristic value of a parameter representing the instantaneous flow condition. Examples of this parameter include the dominant frequency of the flow or the oscillation amplitude measured by a sensor (see § 3.6.1). The Galerkin model retains the form (3.11), with parameterized coefficients, and the expansion (3.8) is interpreted with respect to the local expansion modes, associated with the present parameter value. This model is valid for slow vertical transitions along the dynamic manifold in figure 3.3 (which prevents the need to include the dynamics of mode deformation).

The key relevant fact for control design is that the local model provides the appropriate value for the orientation of the volume force  $\theta$  and appropriate local concepts of the instantaneous phase  $\phi$  and amplitude  $A$  of the flow. Indeed, these are the three key quantities needed for effective (opposition) control. In figure 3.4 it is shown how the orientation of the volume force  $\theta = \arg(g_1 + \imath g_2)$  changes as the flow traverses from its natural state (operating condition 1) towards the stabilized state (increasing operating condition index  $p$ ).



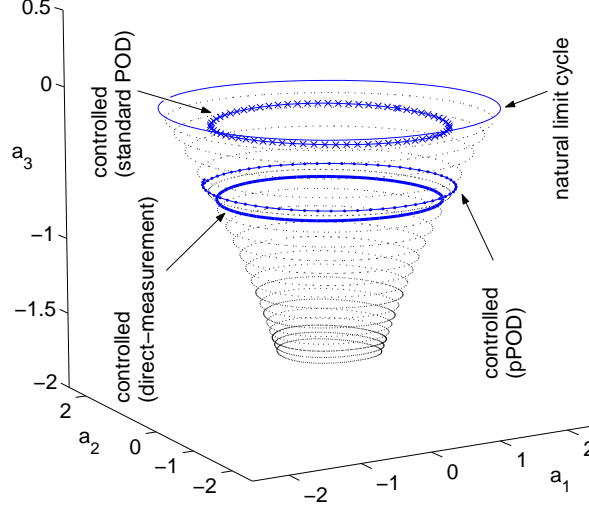


Figure 3.3: Phase space of the first three temporal amplitudes  $a_1$ ,  $a_2$  and  $a_3$ , obtained by projection of the snapshots onto the respective POD modes. The top limit cycle (—) corresponds to the natural flow. The lightly dotted circles ( $\cdots$ ) correspond to the phase portraits of the pPOD mode sets (see § 3.5.2). The remaining limit cycles are described in § 3.5.3 and highlight control results with feedback amplitude  $G = -0.3v_{vf}$  obtained with standard POD ( $- \times -$ ), pPOD ( $- \cdot -$ ) and direct flow measurement (—).

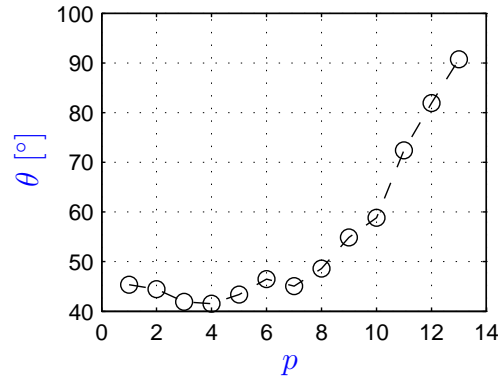


Figure 3.4: Orientation of the volume force  $\theta$  in dependence of the operating condition  $p$ .

### 3.5.3 Full information control

A Galerkin model-based version of the dissipative feedback  $B = -\tilde{k}v_{vf}$  (see (3.7)) is used for stabilization of the cylinder wake. The vertical velocity in the center of the volume force is approximated by the vertical component of the Galerkin expansion (2.65)

$$v_{vf}(t) \approx a_1(t)v_1(\mathbf{x}_{vf}) + a_2(t)v_2(\mathbf{x}_{vf}), \quad (3.15)$$

where  $v_{1,2}(\mathbf{x}_{vf})$  are the vertical components of POD modes 1 and 2 at the center of the volume force. At each time step the temporal coefficients  $a_i$  can be obtained by the projection (2.21)

$$a_i(t) = (\mathbf{u}(\mathbf{x}, t), \mathbf{u}_i(\mathbf{x}))_{\Omega}.$$

Equations (3.7), (3.15) and (2.21) establish a full information control based on the POD or Galerkin approximation of the flow field.

For feedback flow control based on parameterized POD, the reconstruction of  $v_{vf}$  in (3.15) depends on the employed mode set. A given snapshot can be reconstructed with (3.8) for all parameterized mode sets. The optimal index  $p = \tilde{p}$  is determined from the requirement that the error between the given and reconstructed snapshot is minimal:

$$\tilde{p} = \arg \min_p \|\mathbf{u}(\mathbf{x}, t) - (\mathbf{u}_s(\mathbf{x}) + a_1(t)\mathbf{u}_1(\mathbf{x}, p) + a_2(t)\mathbf{u}_2(\mathbf{x}, p) + a_3(t)\mathbf{u}_3(\mathbf{x}))\|.$$

In this section, the employed mode set  $\tilde{p}$  is computed for each snapshot using the above criterium. Subsequently, the vertical velocity in the center of the volume force is computed with (3.15) using the index  $\tilde{p}$ .

Figure 3.3 compares the natural attractor with limit cycles obtained by feedback control with a POD model extracted from the natural flow, control using the parameterized POD (pPOD) model and, as a benchmark, control with direct flow measurement. In all cases, the feedback gain is identical:  $k = 0.3$ . It should be noted that with this gain complete attenuation cannot be achieved. As can be seen, the attenuation achieved with the standard POD model is much inferior to what is attained with the interpolated model, which, in turn is close to the response with direct flow measurement. The POD model of the natural flow is only valid in a narrow neighbourhood of the natural flow. This implies that the

### 3.6 SISO control with parameterized POD

---

	Natural Flow	Standard POD	Parameterized POD	Complete Information
$v_{vf \max}$	0.520	0.312	0.189	0.137
$x_{\text{rec}}$	2.35	2.89	3.56	3.73
$TKE$	2.43	2.24	1.86	1.75

Table 3.1: Quantities that highlight the differences between standard and interpolated models. The following quantities are tabulated: (i) the oscillation amplitude of the vertical velocity  $v_{vf}$  at the center of the volume force, denoted  $v_{vf \max}$ , (ii) the average length of the recirculation bubble  $x_{\text{rec}}$ , and (iii) the perturbation (= turbulent kinetic) energy (TKE) in each limit cycle.

controller does not provide the actuator with an optimal signal as the flow deviates more and more from its natural state. Hence the volume force does not directly counteract the vortices, and the flow settles close to the natural attractor. The result of the pPOD model is close to the direct-measurement, since the parameterization of the flow is fine enough, and the vortices are almost optimally opposed.

In table 3.1 several quantities are tabulated that show the performance of the standard model and the interpolated model. As in figure 3.3, results for the natural flow, feedback control with a POD model extracted from the natural flow, control using the parameterized POD and control with direct flow measurement are summarized.

## 3.6 SISO control with parameterized POD

In contrast to the previous section, where full information control was considered, the focus is now on a single-input single-output type controller. A dynamic observer (§ 3.6.1) estimates the state of the flow by appropriate processing of the sensor signal. Using the state estimation, a pPOD based look-up table (§ 3.6.2) provides the optimal actuation signal (the single output) to oppose the vortex street. The sensor location (the single output) is optimized in § 3.6.3. The success of the SISO controller is demonstrated in § 3.6.4.

### 3.6.1 Observer design

In this section, an observer is designed in order to provide an estimate of the flow state. This observer is a crucial part of the SISO controller which is described in § 3.6.4. A full state observer, based on the Galerkin system (3.10) in a fixed (no tuning) empirical GM is discussed in Gerhard *et al.* (2003). Here, a simpler alternative is employed that, among other advantages, bypasses the need to address the parameter and time dependence of the expansion modes. Like the parameterized model, the observer exploits the timescale separation between the periodic oscillations and the transition between operating points. This separation is represented schematically by motion in the horizontal cross sections of the manifold in figure 3.3, and by the vertical component of motion respectively. The latter, i.e. the mean flow change, is responsible for slow changes in the oscillation frequency and amplitude. It is stipulated that the controller may not violate the assumption of a slowly changing system.

For simplicity, the case of a single (vertical) velocity sensor at a point  $\mathbf{x}_s$  is considered, although the ideas are extendable to the utilization of multiple sensors. The ideal sensor signal is of the form

$$s = v_0(\mathbf{x}_s) + a_1 v_1(\mathbf{x}_s) + a_2 v_2(\mathbf{x}_s) = A_0 + A_1 \cos(\theta), \quad (3.16a)$$

$$\dot{\theta} = \omega, \quad (3.16b)$$

where  $v_i$  are the vertical components of the POD modes  $\mathbf{u}_i$  and parameter dependence notations ( $p$ ) are suppressed, and  $\omega$  is interpreted as the instantaneous vortex shedding frequency (i.e., the quantity  $\omega + \gamma a_3$  in (3.11b)), and where both the unknown  $A_0$ ,  $A_1$  and the frequency  $\omega$  are slowly varying. Time variation is due to actuation which suppresses vortex shedding, and hence changes the associated dominant velocity fields. The formulation (3.16) is used to dynamically track slow changes in the coefficients  $A_0$ ,  $A_1$  and the frequency  $\omega$  and the nearly linear growth in  $\theta$  as explained below. The estimated  $A_0$ ,  $A_1$  and  $\omega$  can be used to parameterize the operating conditions (and their associated indexed mode sets). As an example, the operating condition is parameterized by the frequency or the amplitude of a vertical velocity sensor at  $(x, y) = (6.8D, 0)$ , see figure 3.5.

### 3.6 SISO control with parameterized POD

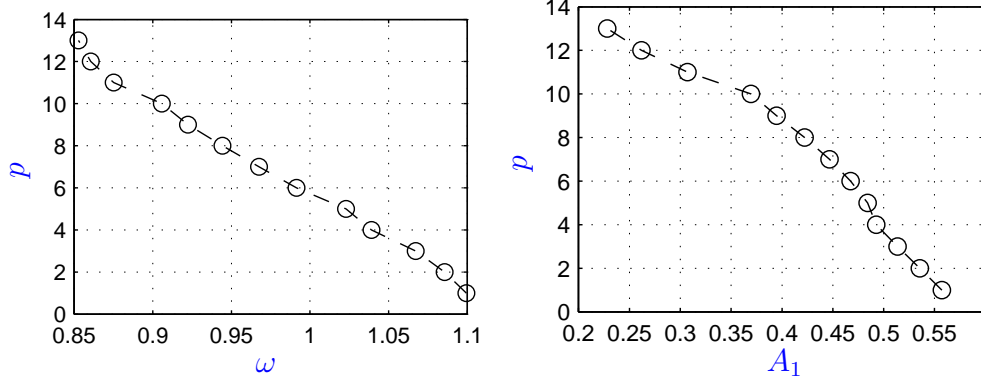


Figure 3.5: Parameterization of the operating condition  $p$ . Left: frequency as parameter. Right: amplitude of a vertical velocity sensor at  $(x, y) = (6.8D, 0)$  as parameter.

The assumption that the quantities  $A_0$ ,  $A_1$ ,  $\omega$  are subject to slow changes leads to a nominal discrete time dynamic model

$$\begin{bmatrix} A_0 \\ A_1 \\ \omega \\ \theta \end{bmatrix} (t_{k+1}) = \begin{bmatrix} 1 & 0 & 0 & 0 \\ 0 & 1 & 0 & 0 \\ 0 & 0 & 1 & 0 \\ 0 & 0 & \Delta t & 1 \end{bmatrix} \begin{bmatrix} A_0 \\ A_1 \\ \omega \\ \theta \end{bmatrix} (t_k), \quad (3.17a)$$

$$s(t_k) = A_0(t_k) + A_1(t_k) \cos(\theta(t_k)), \quad (3.17b)$$

where  $\Delta t$  is the time step. This framework is, in fact, a simpler variant of the dynamic phasor approximation used in [Tadmor \(2004\)](#), and readily lends itself to state estimation by an extended Kalman filter (EKF), where the emphasis is on conservative, hence slow tracking.

Model (3.17) forms a (slow) narrow banded low-pass filter for reconstruction of the sensor signal. The plots in figure 3.6 demonstrate the dynamic reconstruction of a sensor signal at  $(x, y) = (6.8D, 0)$ . The zoom on the right side in figure 3.6 shows that the observer can track the sensor signal well during relatively slow transients. The corresponding estimated frequency and amplitude of the sensor signal are shown in figure 3.7. The initialization time of the EKF is about 16 time units. The measurement noise covariance  $\mathbf{R}$  and the process noise covariance  $\mathbf{Q}$  matrices are respectively set to:  $\mathbf{R} = 1$  and  $\mathbf{Q} = \text{diag}(1.0 \times 10^{-4}, 1.0 \times 10^{-3}, 8.0 \times 10^{-4}, 1.0 \times 10^{-5})$ .

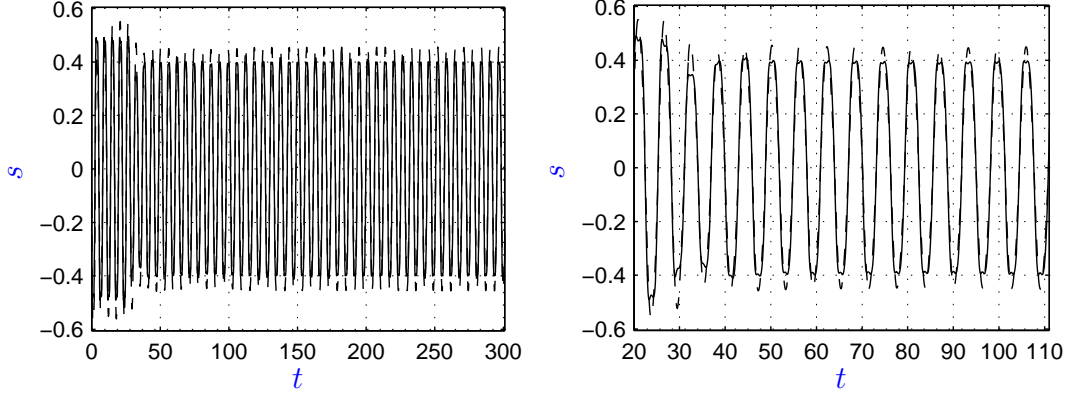


Figure 3.6: The sensed velocity trajectory (—) of a vertical velocity sensor at  $(x, y) = (6.8D, 0)$  and its dynamic estimate (---). Both the entire trajectory (left) and a zoom on the changing transient (right) are displayed.

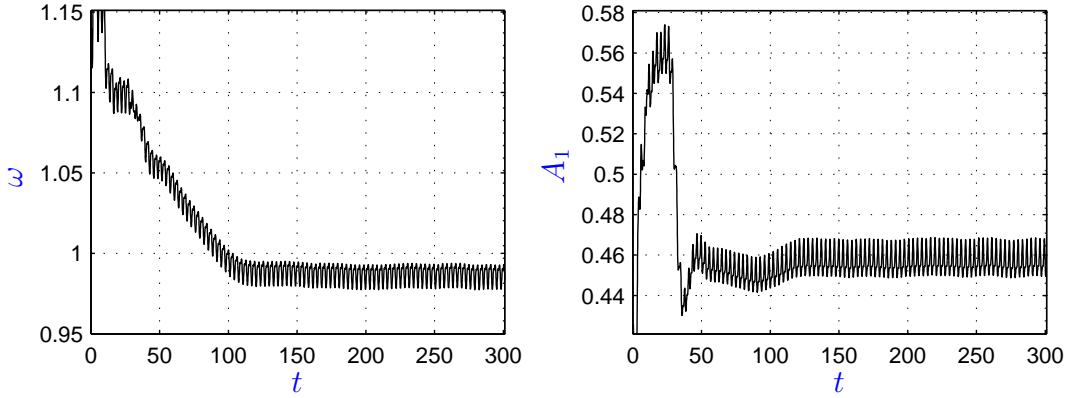


Figure 3.7: The estimated frequency (left) and amplitude (right) of a vertical velocity sensor at  $(x, y) = (6.8D, 0)$ .

### 3.6.2 A parameterized POD based look-up table

As noted before the only admissible control policy is the physics based, dissipative policy described in § 3.3.1. The goal here is to relate the ideal actuation signal (3.5) to the dynamically estimated signal (3.17b). Therefore (3.5) is written as follows:

$$-k(t) \int_{\Omega} g(\mathbf{x}) \cdot \mathbf{u}'(\mathbf{x}, t) dV = -\hat{k}(t) \cos(\theta_s(t) - \Delta\phi(t)) \quad (3.18)$$

where  $\hat{k}$  is the amplitude of the actuation signal,  $\theta_s$  the phase of the sensor signal and  $\Delta\phi$  the phase difference between the sensor signal and the ideal actuation signal, (i.e. the phase of the signal on the left hand side of the equation). These phase relationships can be conveniently approximated by the parameterized POD. Decomposition of the left hand side of (3.18) yields

$$-k(t) (a_1 g_1 + a_2 g_2) = -k(t) A b \cos(\theta - \phi), \quad (3.19)$$

where  $\theta = \arg(g_1 + \imath g_2)$  and  $\phi = \arg(a_1 + \imath a_2)$ . For other notations, see § 3.4.2. Decomposition of the fluctuating part of the sensor signal yields

$$s - A_0 = A_1 \cos(\theta_s) = a_1 v_1(\mathbf{x}_s) + a_2 v_2(\mathbf{x}_s) = A v_s \cos(\tilde{\theta}_s - \phi), \quad (3.20)$$

where  $v_{1,2}(\mathbf{x}_s)$  are the vertical components of POD modes 1 and 2 at the sensor location, and  $v_s = \sqrt{v_1(\mathbf{x}_s)^2 + v_2(\mathbf{x}_s)^2}$ . The angle  $\tilde{\theta}_s$  is defined by  $\tilde{\theta}_s = \arg(v_1(\mathbf{x}_s) + \imath v_2(\mathbf{x}_s))$ . Comparing (3.18), (3.19) and (3.20), the (approximate) phase difference between the ideal actuation signal and a sensor at  $\mathbf{x}_s$  is given by

$$\Delta\phi = \tilde{\theta}_s - \theta. \quad (3.21)$$

This phase difference can be stored in a look-up table in dependence of the operating condition. For a sensor at  $(x, y) = (6.8D, 0)$ , the phase difference  $\Delta\phi$  as function of the frequency is shown in figure 3.10. Note that for this sensor the changes in phase difference are significant over the simulated trajectories (about  $50^\circ$ ).

### 3.6.3 Sensor optimization

In this section, the parameterized POD mode sets are used to find efficient locations of sensors. For the optimization of the sensor location, it is assumed that the dynamics around each local operating condition is governed by a linear dynamic system. This assumption allows us to borrow the concept of observability Gramian, which determines whether a system is observable. The inverted observability Gramian of a linear (time varying) system defines a measure of the sensitivity of an output signal to state changes. The smallest singular value of the Gramian therefore provides a systematic quantification of the dynamic effectiveness of the sensor (Lim, 1992) and yields a meaningful cost index for model based optimization. In a nonlinear system, Gramians defined by linearizations along representative trajectories are the natural substitute. When the system is nearly periodic, the Gramians associated with a single period and normalized by the period length are natural candidates. As may well be expected and as is illustrated in the cylinder wake flow, below, changes in dominant modes as the system transitions between operating points are reflected by changes in the sensitivity of sensors to state dynamics. A meaningful optimization criterion would therefore be to maximize the worst sensor performance over the entire transient range.

Consider now the cylinder wake flow with one sensor. For notational simplicity it is assumed that this sensor measures the vertical velocity (i.e., the ‘ $v$ ’ component of the velocity field) at point  $\mathbf{x}_1$ . The focus is on the short term sensitivity of the sensor to the phase and amplitude of the mode amplitudes  $a_1$  and  $a_2$ . In a simplified continuous time model one can thus assume a fixed frequency. Invoking the appropriately adjusted notations of (3.16) and denoting the model tuning parameter by ‘ $p$ ’ (e.g.,  $p = \omega$ ), the sensing problem is defined by the state-space system

$$\frac{d}{dt} \begin{bmatrix} a_1 \\ a_2 \end{bmatrix} = \mathbf{A}(p) \begin{bmatrix} a_1 \\ a_2 \end{bmatrix}, \quad (3.22a)$$

$$s' = s - A_0 = \mathbf{C}(\bar{\mathbf{x}}, p) \begin{bmatrix} a_1 \\ a_2 \end{bmatrix}, \quad (3.22b)$$



### 3.6 SISO control with parameterized POD

---

where  $\bar{\mathbf{x}} = \{\mathbf{x}_k, k = 1 : \dots, K\}$ , and where

$$\mathbf{A}(p) = \begin{bmatrix} 0 & -\omega(p) \\ \omega(p) & 0 \end{bmatrix} \quad \text{and} \quad \mathbf{C}(\bar{\mathbf{x}}, p) = \begin{bmatrix} v_1(\bar{\mathbf{x}}, p) & v_2(\bar{\mathbf{x}}, p) \end{bmatrix}. \quad (3.23)$$

The state matrix  $\mathbf{A}$  describes the periodic oscillation. The output matrix  $\mathbf{C}$  follows from the Galerkin approximation:  $\mathbf{u}'(\mathbf{x}, t) = a_1(t)\mathbf{u}_1(\mathbf{x}, t) + a_2(t)\mathbf{u}_2(\mathbf{x}, t)$  at the sensor location. The normalized single period observability Gramian of the system is given by

$$\bar{\mathbf{G}}_o = \frac{1}{T} \int_0^T e^{\mathbf{A}(p)'t} \mathbf{C}(\bar{\mathbf{x}}, p)' \mathbf{C}(\bar{\mathbf{x}}, p) e^{\mathbf{A}(p)t} dt = 0.5 \|C(\bar{\mathbf{x}}, p)\|_F^2 \mathbf{I}_2, \quad (3.24)$$

where the explicit form of the matrix exponential is used,

$$e^{\mathbf{A}t} = \begin{bmatrix} \cos(\omega t) & -\sin(\omega t) \\ \sin(\omega t) & \cos(\omega t) \end{bmatrix},$$

the subscript  $F$  indicates the Frobenius norm, and  $\mathbf{I}_2$  is the  $2 \times 2$  identity matrix. The optimal sensor location is therefore determined as the solution of the optimization problem

$$\max_{\bar{\mathbf{x}}} \min_p \|C(\bar{\mathbf{x}}, p)\|_F. \quad (3.25)$$

The optimum is computed over all grid points  $\bar{\mathbf{x}}$ . For one sensor, the squared Frobenius norm of the output matrix is given by

$$\|C(\bar{\mathbf{x}}, p)\|_F^2 = v_1(\bar{\mathbf{x}}_1, p)^2 + v_2(\bar{\mathbf{x}}_1, p)^2, \quad (3.26)$$

which simply is proportional to the averaged kinetic energy resolved by the vertical velocity component. Addition of a sensor, which measures the horizontal component at the same location, yields the measure of kinetic energy in that point. By definition of the Frobenius norm (the square root of the sum of all squared elements of a matrix), this observation extends to multiple sensors.

In figure 3.8 plots are shown of  $\|C(\bar{\mathbf{x}}, p)\|_F$  as a function of the operating condition  $p$ , where the sensor location  $\bar{\mathbf{x}}_*$  was optimized with respect to the first 1, 5, and 13 operating conditions out of 13. In the left plot, the result is shown for a single  $u$ -velocity sensor and in the right for a single  $v$ -velocity sensor. As is clearly observed, the predicted performance of a sensor that is optimized for a single parameter value (i.e., only for the natural attractor) is higher close to

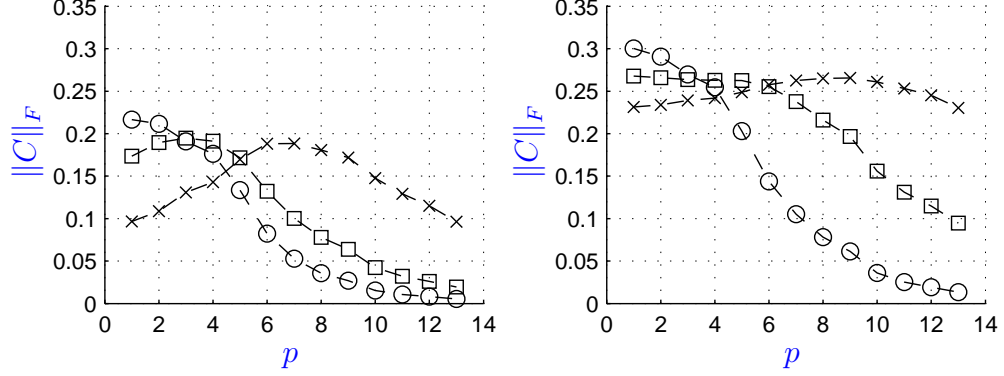


Figure 3.8: Performance of an optimal sensor by measure of the Frobenius norm  $\|C(\bar{\mathbf{x}}_*, p)\|_F$  as a function of the operating condition  $p$ . Left: performance for a single  $u$ -velocity sensor, right: performance for a single  $v$ -velocity sensor. The sensor location  $\bar{\mathbf{x}}_*$  (see figure 3.9) is optimized for the first 1 ( $\circ$ ), 5 ( $\square$ ), and 13 ( $\times$ ) out of 13 equally spaced operating points.

the natural state ( $p = 1$ ) but deteriorates rapidly with the change of  $p$ , while those optimized over a wider range maintain an increasingly even performance during transitions. The corresponding locations of the sensor are shown in figure 3.9. As the wake is more stabilized, the vortex street is pushed downstream and the associated maximum fluctuations as well. This implies that favourable sensor locations also move downstream during the stabilization of the wake. As can be inferred from the right plot in figure 3.9 the best vertical velocity sensors lay on the equator. The best horizontal velocity sensors lay on a slightly angled line that starts at about  $(x, y) = (0.5D, 2.5D)$  and ends at  $(x, y) = (5.3D, 0.75D)$  (left plot of figure 3.9). By symmetry of the first two POD modes, the mirrored locations along the equator yield equally good locations. Finally, it is noted that adding more sensors can improve both the relative flatness (peak-to-peak ratio) of the performance measure and increase the minimal value. One can for instance add more sensors along the lines in figure 3.9.

### 3.6.4 Results

The SISO control that is employed here, uses a measurement of the vertical velocity component at  $(x, y) = (6.8D, 0)$ . This location is obtained as solution

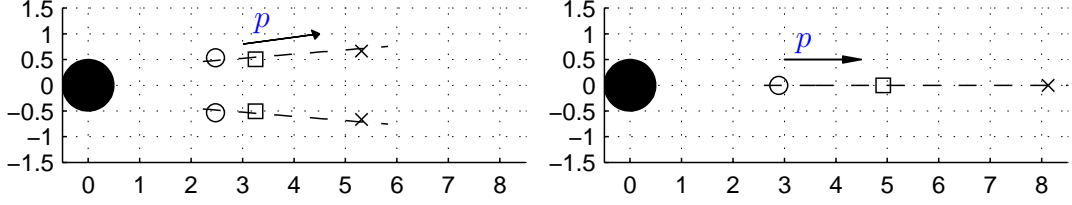


Figure 3.9: Optimized sensor location  $\bar{\mathbf{x}}_*$  for the first 1 ( $\circ$ ), 5 ( $\square$ ), and 13 ( $\times$ ) out of 13 equally spaced operating points. The direction of the arrow indicates that the optimal sensor location moves downstream as more operating points are taken into account. Left:  $u$ -velocity sensor (locations are mirrored around the horizontal symmetry axis), right:  $v$ -velocity sensor.

of (3.25) for optimization over the first 10 operating conditions (compare with figure 3.8, right plot). The dynamic observer, discussed in § 3.6.1, estimates the amplitude, frequency and phase of this sensor signal. The frequency is used as an indicator for the flow state and provides via the look-up table the desired phase difference  $\Delta\phi$  for the actuation signal, see (3.18).

An example of SISO control is shown in figure 3.11. Here the scaled projection of the velocity field onto volume force,  $0.2(\mathbf{u}, \mathbf{g})_\Omega$ , and the actuation signal  $G$  are plotted. The controller starts at  $t = 22.8$ . Ideally these two signals should be  $180^\circ$  out of phase all the time, which is (approximately) the case. The goal in this simulation was to stabilize the flow at a fluctuation level that corresponds to an amplitude of  $(\mathbf{u}, \mathbf{g})_\Omega$  which equals 0.45 ( $t \approx 110$ ). As can be clearly observed, the fluctuation level is decreased to the desired level and settles there. The corresponding elongation of the recirculation bubble length, that is where the  $u$ -velocity changes sign on the equator, is shown in the left plot of figure 3.12. The estimated frequency and amplitude obtained by the observer are shown in figure 3.7. The frequency settles at  $\omega \approx 0.98$ . Comparing this value with figure 3.10, the maximum phase difference  $\Delta\phi$  is about  $10^\circ$ . The result of another simulation, where a recirculation length of about  $x_{rec} \approx 3.8$  is achieved is shown in the right plot of 3.12. This plot clearly demonstrates an overshoot effect, which is closely connected to the physics of the system: the required actuator input to stabilize the wake beyond a recirculation length  $x_{rec} = 3.6$  suddenly decreases and because of the sensor lag (the sensor is relatively far downstream) the recirculation length

overshoots. The wake is in a suppressed state already and only a small amount of energy is needed to stabilize it further.

With the current setup of sensor, observer and look-up table, the unstable wake can hardly be further stabilized. Again, this is mainly due to the relatively large distance between the center of the volume force actuator and the sensor ( $l = 4.3D$ ). This results in time delays of about two shedding cycles. In the regime where the frequency has decreased to less than 0.95, see figure 3.10, the time lag becomes detrimental for the prediction of the phase difference  $\Delta\phi$ . This situation might be resolved by sophisticated gain control, where the actuation amplitude is very slowly adapted. Still this approach will be difficult, since close to the fully stabilized wake the required gain to maintain the fluctuation level suddenly drops, see figure 3.13, which is not anticipated by the current controller. Time lag of the observer and phenomena not described by the look-up table cause the typical ringing behaviour of the recirculation length shown in figure 3.14. Physically speaking, the wake is relatively quickly suppressed, but since the response of the controller is too slow, the actuation signal is so out of phase that the volume force actually strengthens the vortex street till the controller catches it again. As shown in Tadmor *et al.* (2004) for a similar configuration where the wake is suppressed using a translating cylinder instead of a volume force, there are stable and unstable limit cycles under closed-loop control. It is assumed that this is also the case here. The fluctuation level is brought down to the desired level, but since this level corresponds to an unstable limit cycle it is not possible to maintain the flow there (at least under the control policy used here).

## 3.7 Conclusions

A framework of interpolated Galerkin models for fluid flow systems strikes a balance between the need for higher number of modes to represent actuation and transients and the desire to maintain model simplicity. This in turn minimizes the number of dynamic variables that need to be estimated in real time feedback implementation. Advantages over standard POD models have been illustrated in the context of vortex shedding suppression behind a circular cylinder, and are manifest by improved ability to suppress vortex shedding and an improved

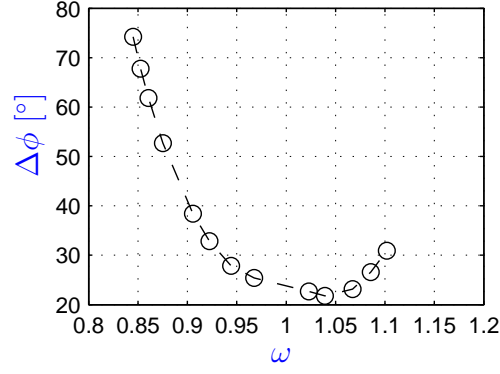


Figure 3.10: The phase difference  $\Delta\phi$  between the sensor signal of a vertical velocity sensor at  $(x, y) = (6.8D, 0)$  and the ideal actuation signal as function of the frequency.

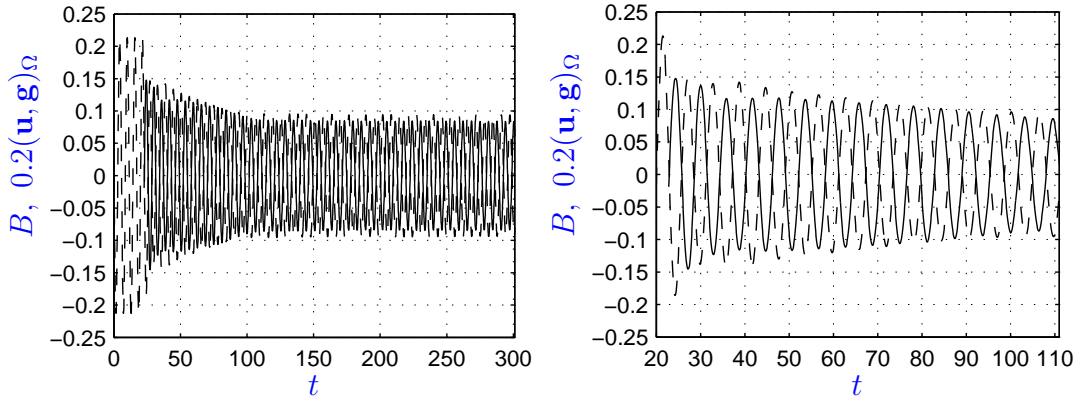


Figure 3.11: Actuation signal  $B$  (—) of a successful controller and the scaled projection of the velocity field onto the volume force:  $0.2(\mathbf{u}, \mathbf{g})_\Omega$  (---) versus time. The controller starts at  $t = 22.8$ .

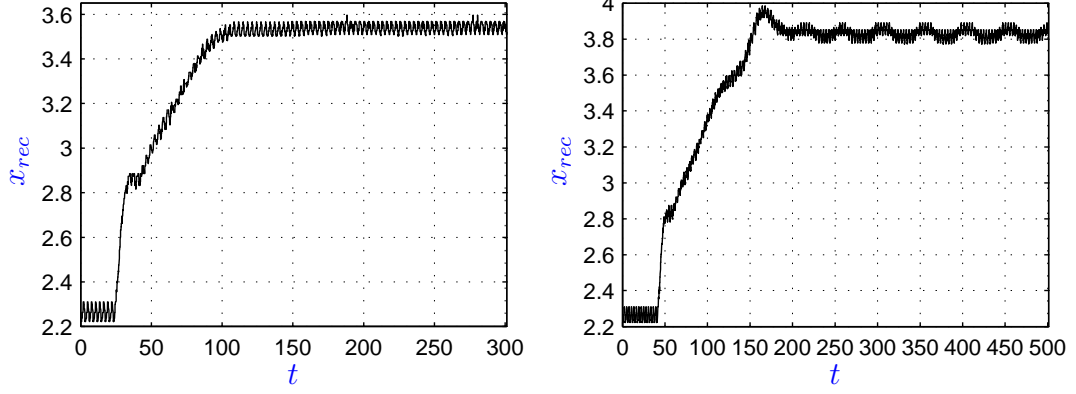


Figure 3.12: The elongation of the recirculation length as a function of time for two successful simulations. Left: a monotonous increase corresponding to the actuation signal in figure 3.11. Right: an illustration of overshoot.

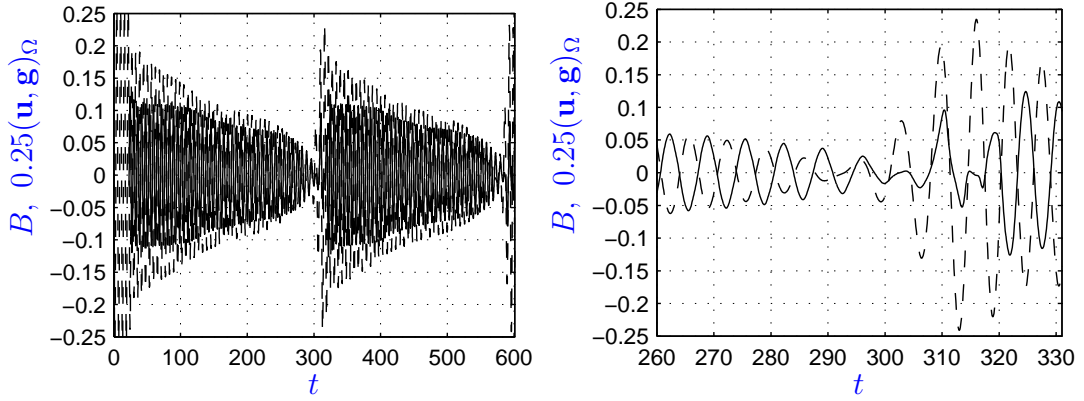


Figure 3.13: Illustration of the gain / phase problem. Left: a plot of the actuation signal  $B$  (—) and the scaled projection of the velocity field onto the volume force:  $0.25(\mathbf{u}, \mathbf{g})_\Omega$  (---) versus time, right: a zoom that illustrates the problem around the desired state. The controller starts at  $t = 22.8$ .

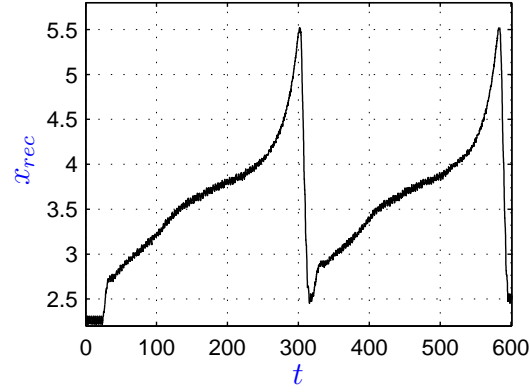


Figure 3.14: A ‘ringing’ recirculation length as a function of time, corresponding to the actuation signal in figure 3.13

sensor performance over a wider transients range. Due to intrinsic instabilities it is difficult to fully stabilize the wake using SISO control with interpolated models.

# Chapter 4

## Separation control of the flow around a high-lift configuration

### 4.1 Abstract

A mean-field Galerkin model is employed for the flow around a high-lift configuration, describing natural vortex shedding, the high-frequency actuated flow with increased lift, and transients between both states. The form of the dynamical system follows from a generalized mean-field consideration. Steady state and transient URANS simulation data are used to derive the expansion modes and to calibrate the system parameters. The model identifies the mean field as the mediator between the high-frequency actuation and the low-frequency natural shedding instability. A sliding mode controller, based on the mean-field model, is implemented for set-point tracking of the lift coefficient.

### 4.2 Introduction

Periodic excitation is one of the fundamental tools of active flow control, see for example [Gad-el-Hak \(2000\)](#). In particular, separation of the flow over airfoils at high angles of attack can be delayed using periodic actuation ([Amitay & Glezer, 2002](#); [Becker \*et al.\*, 2007](#); [Collis \*et al.\*, 2004](#); [Raju & Mittal, 2002](#); [Seifert \*et al.\*,](#)

---

Published in: [Luchtenburg \*et al.\* \(2009a, 2010\)](#).



1996). Effective options include high-frequency forcing using synthetic jets and plasma actuators. A flow model of the actuated system is desirable as a test-bed for physical understanding and is necessary for systematic feedback control design. To be useful for feedback design, the model must be both sufficiently simple for feasible, real-time implementation, and yet robustly represent the natural and actuated dynamics. In particular, models must be capable of representing the cross-frequency interaction between high-frequency actuation and low-frequency instabilities, and do so with the least feasible number of modes. The current chapter proposes a framework for such models. Separation control of the flow around a high-lift configuration with high-frequency actuation serves as a benchmark for the development of a least-order design model using proper orthogonal decomposition (POD) and shift-modes (Noack *et al.*, 2003).

The high-lift configuration plays an essential role in the takeoff and landing performance of large commercial aircrafts, allowing lower landing and takeoff speeds and thus shorter runways. Conventionally, such a configuration consists of complex, heavy and expensive multi-element high-lift devices. Active separation control is currently studied as a means for more compact and less heavy configurations or alternatively, shorter takeoff and landing runs. In Günther *et al.* (2007) the authors present an experimental and numerical investigation, showing that the mean aerodynamic lift of a traditional three element high-lift configuration can be significantly enhanced by means of open-loop periodic excitation. As recently shown by Pastoor *et al.* (2006, 2008), the efficiency and efficacy of periodic actuation can be significantly improved by closing the loop in flow control using sensor measurements. Building on these results, the modelling framework suggested here is intended as an enabler for subsequent model-based optimization and closed-loop design.

Typically, the actuation frequency is not harmonically related to the shear-layer frequency, and is higher than the vortex-shedding frequency (Günther *et al.*, 2007; Raju & Mittal, 2002). A low-dimensional model representing each of the leading harmonics by a mode pair naturally accommodates amplitude and phase manipulations. Quadratic nonlinearity allows to enrich this repertoire with frequency doubling and time variations. Yet, very low order models, based, e.g. on POD analysis of natural and actuated attractors, are incapable of capturing the

energy transfer between mode pairs that represent unrelated frequencies. Even more so, the phase-independent open-loop stabilizing effect of high-frequency actuation cannot be explained by direct mode interactions — even when the actuation and the instability frequencies are harmonically related. This difficulty is sharpened in the fairly common case, encountered in the current discussion, where dominant coherent structures associated with different frequencies do not have significant spatial overlap. The mean-field model, described in § 2.3.3, § 2.3.4, accommodates these multi-frequency fluctuations.

The mean-field model with two mean-field modes captures energy exchanges between mean flow structures and the fluctuations at the natural and the actuated frequencies. The fact that fluctuations at the actuated frequency are naturally stable reflects, in this context, a higher stabilizing effect of the mean-field changes induced at that frequency, than those due to the natural instability. Consequently, the forced amplification of the fluctuations at the actuated frequency, and of entailed base flow changes, lead to the desired and observed attenuation of the natural instability. The mean-field modes are therefore proposed as the missing component, mediating between the high-frequency actuation and the natural, lower frequency instability. The model is validated and calibrated, using flow data of unsteady Reynolds-averaged Navier-Stokes (URANS) simulations. As will be seen, the mean-field POD model is capable to predict the effect of actuation on both the velocity field and on the associated lift coefficient.

## 4.3 Numerical simulation

In this section, the benchmark simulation of the flow around the high-lift configuration is outlined, including the configuration (§ 4.3.1), the simulation (§ 4.3.2), and the flow properties (§ 4.3.3).

### 4.3.1 Configuration

We study the incompressible two-dimensional flow over the **S**wept **C**onstant **C**hord **H**alf (SCCH) high-lift configuration (see figure 4.1). This configuration is employed in several experimental and numerical studies targeting passive and

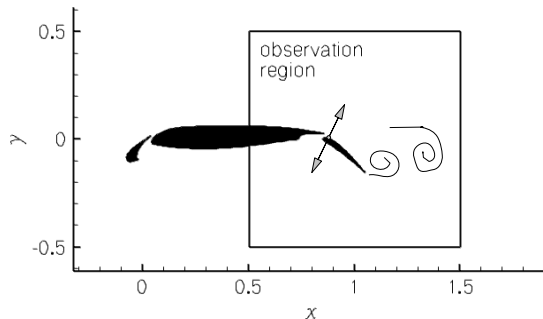


Figure 4.1: A sketch of the three element high-lift configuration and the observation region for the model. Periodic excitation ( $\leftrightarrow$ ) is implemented at the upper part of the trailing edge flap.

active flow control (Günther *et al.*, 2007; Schatz *et al.*, 2006). The control goal in these studies includes lift enhancement as well as noise suppression. The chord length of the configuration, with retracted high-lift devices, is denoted by  $c$ . The three-component setup consists of a main airfoil equipped with a leading edge slat and a trailing edge flap with relative chord lengths of  $c_{sl} = 0.158 c$  and  $c_{fl} = 0.254 c$ , respectively. Henceforth, all physical variables are assumed non-dimensionalized with respect to the chord length  $c$ , the incoming flow velocity  $U_\infty$ , and the constant density  $\rho$ . The flow is considered at the Reynolds number of  $Re = U_\infty c / \nu = 10^6$  ( $\nu$ : kinematic viscosity of the fluid). The slat deflection angle is set to  $26.5^\circ$ , the flap deflection angle to  $37^\circ$  and the angle of attack of the main wing section is  $6^\circ$ . At these conditions, the flow remains attached over the slat and the main wing section, but is fully separated over the flap. Then, the wake is characterized by the periodic generation and alternate shedding of leading and trailing edge vortices.

Periodic actuation is introduced via a zero-net-mass-flux actuator on a small wall section at the upper side of the trailing edge flap. The imposed flow velocity is orthogonal to the wall and is located at  $0.04 c$  behind the leading edge of the flap (see figure 4.1). The actuation velocity is prescribed by

$$b(t) = B \cos(\Omega^a t), \quad (4.1)$$

where  $\Omega^a$  is the angular actuation frequency and  $B$  the amplitude of actuation. This frequency is given by

$$\Omega^a = 2\pi St^a,$$

where  $St^a = f^a c/U_\infty$  represents the Strouhal number with the actuation frequency  $f^a$ . The Strouhal number for natural (un-actuated) vortex-shedding frequency  $f^n$  is analogously defined,  $St^n = f^n c/U_\infty$ . Experimental and computational studies of flows around high-lift configurations often non-dimensionalize the frequencies with the flap length  $c_{\text{fl}}$  as opposed to the cord length  $c$ . Hence, the following notation is introduced  $St_{\text{fl}} = f c_{\text{fl}}/U_\infty = (c_{\text{fl}}/c) St$  with applicable superscripts ‘ $n$ ’ and ‘ $a$ ’ for later reference.

The actuation intensity is characterized by the non-dimensional momentum coefficient

$$C_\mu = \frac{H}{c} \left( \frac{B}{U_\infty} \right)^2,$$

where  $H$  is the slot width ( $H = 0.001238 c_{\text{fl}}$ ).

### 4.3.2 Unsteady Reynolds-averaged Navier-Stokes simulation

The two-dimensional coherent structure dynamics are resolved by the unsteady Reynolds-averaged Navier-Stokes (URANS) equation. Small-scale turbulent fluctuations are incorporated by the LLR  $k$ - $\omega$  model (Rung & Thiele, 1996). The URANS equation is discretized by an incompressible finite-volume scheme of second order accuracy in space and time. The numerical data used here have been obtained with the numerical code *ELAN* developed at the Computational Fluid Dynamics and Aeroacoustics Group (Prof. F. Thiele) at the Berlin Institute of Technology. The computational domain extends  $15c$  upstream, above and below the airfoil and  $25c$  downstream. This domain is discretized on a multi-block structured mesh into 90,000 cells. The non-dimensional wall distance of the first cell center is kept below  $y^+ = 1$  over the entire surface.

### 4.3.3 Natural and periodically forced flow

The unactuated flow field around the trailing edge flap is characterized by massive separation. The left side of figure 4.2 shows a characteristic snapshot and its Reynolds decomposition. The dead-water zone is associated with periodic vortex shedding above the upper surface of the flap. The spectrum of the lift coefficient reveals a dominant Strouhal number of  $St_{\text{fl}}^n = f^n c_{\text{fl}} / U_{\infty} = 0.32$  corresponding to that vortex shedding.

Actuation is switched on starting from natural flow conditions. A parameter study shows that, under periodic actuation, lift is maximized at a momentum coefficient of  $C_{\mu} = 400 \times 10^{-5}$  and an excitation frequency of  $St_{\text{fl}}^a = 0.6$ . In this case, the lift coefficient is increased by 19%. For the modelling task, the actuation frequency is set  $St_{\text{fl}}^a = 0.6$  and  $C_{\mu} = 114 \times 10^{-5}$ . This results in a lift increase of about 15% at an actuation frequency that is 1.88 times larger than the natural shedding frequency, i.e.  $St_{\text{fl}}^a / St_{\text{fl}}^n = 1.88$ . The effect on the flow field is the near complete attenuation of fluctuations at the natural frequency, and the emergence of a new attractor, locked-in on the actuation frequency. The right side of figure 4.2 shows a characteristic snapshot of the actuated flow. Spatially, the natural oscillations are most pronounced in the wake, actuated fluctuations are concentrated above and near the trailing edge flap.

## 4.4 Phenomenological modelling

In this section, the lift-increasing effect of high-frequency forcing is phenomenologically modelled. Simple arguments will lead us to the same form of the dynamical systems as a more elaborate derivation from the Navier-Stokes equation in subsequent sections.

The dynamical system shall describe four aspects of the URANS simulations:

- (i) vortex shedding without actuation;
- (ii) lock-in shear-layer shedding under high-frequency forcing;
- (iii) the transient from state (i) to state (ii) under forcing; and

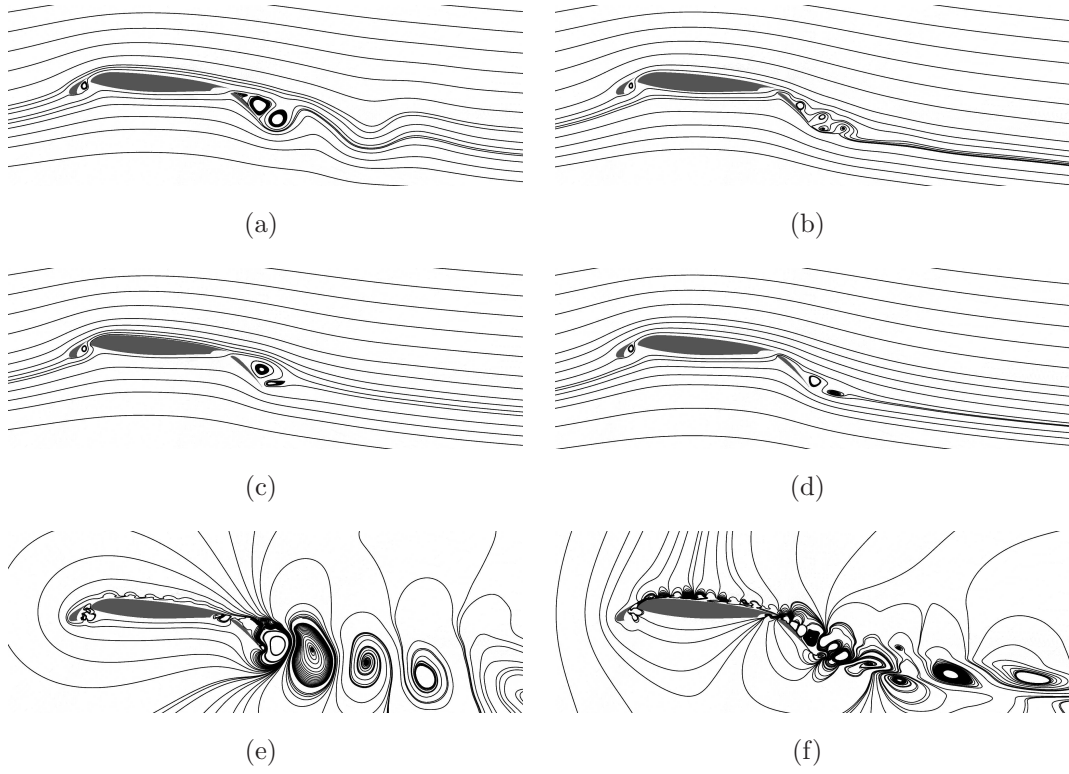


Figure 4.2: Comparison of a natural (a,c,e) and an actuated snapshot (b,d,f). The top row (a,b) shows a characteristic snapshot that is Reynolds decomposed into the respective attractor mean (c,d) and instantaneous fluctuation (e,f). The flow field is visualized by streamlines.

(iv) the transient from (ii) to (i) when forcing is turned off.

Oscillatory flows are characterized by an amplitude  $A$  and phase  $\alpha$ . These quantities can be considered as polar coordinates of the phase space  $(a_1, a_2) = A [\cos \alpha, \sin \alpha]$ . Superscripts ‘ $n$ ’ and ‘ $a$ ’ refer to the natural and actuated state, respectively.

The self-amplified, amplitude-limited behaviour of vortex shedding may be described by the Landau equation (see (2.87))

$$\dot{a}_1^n = \tilde{\sigma}^n a_1^n - \omega^n a_2^n, \quad (4.2a)$$

$$\dot{a}_2^n = \omega^n a_1^n + \tilde{\sigma}^n a_2^n, \quad (4.2b)$$

$$\tilde{\sigma}^n = \sigma^n - \sigma^{n,n} (A^n)^2, \quad (4.2c)$$

where  $\sigma^n$  denotes the positive growth rate,  $\sigma^{n,n}$  the positive Landau constant and as noted above,  $A^n = \sqrt{(a_1^n)^2 + (a_2^n)^2}$  the amplitude. For reasons of simplicity, the frequency  $\omega^n$  is assumed as constant.

The shear-layer dynamics is excited by high-frequency forcing with amplitude  $B$ , phase  $\beta$  and frequency  $\dot{\beta} = \Omega^a = \omega^a$ . The phase difference of the actuation signal with respect to the oscillation of the flow is given by  $\theta$ . This behaviour is most easily represented by a linear damped oscillator with a periodic forcing at the eigenfrequency:

$$\dot{a}_1^a = \sigma^a a_1^a - \omega^a a_2^a + g B \cos(\theta + \beta), \quad (4.3a)$$

$$\dot{a}_2^a = \omega^a a_1^a + \sigma^a a_2^a + g B \sin(\theta + \beta). \quad (4.3b)$$

Here,  $\sigma^a$  denotes a negative growth-rate and  $g$  the gain of actuation.

Both oscillations are comprised in a four-dimensional phase space:

$$[a_1, a_2, a_3, a_4] = [a_1^n, a_2^n, a_1^a, a_2^a]$$

with equations (4.2) and (4.3) governing the joint evolution of these variables. If  $B \equiv 0$ , then  $a_3 = a_4 \equiv 0$ , and the resulting system describes the natural flow, according to (i). By (ii), the oscillation at the natural frequency is suppressed when forcing  $B > 0$  is employed. This can be achieved by decreasing the growth rate of the natural amplitude, eventually leading to damping, with the growth

of the high-frequency amplitude  $A^a = \sqrt{(a_1^a)^2 + (a_2^a)^2}$ . In complete analogy to the damping term of Landau's model, the coefficients  $-\sigma^{n,a} (A^a)^2$  are added to (4.2c) following similar reasoning (see § 2.3.3). The coefficient is chosen to be  $\sigma^{n,a} > \sigma^n / (A^{a,a})^2$ , where  $A^{a,a}$  is the constant value of the amplitude  $A^a$  at the forced state. This choice guarantees  $\tilde{\sigma}^n < 0$  for all  $A^n > 0$  at  $A^a = A^{a,a}$ . Thus, the limit values  $a_1 = a_2 \equiv 0$  are reached at the forced state, according to (ii). In summary, the following system of two coupled oscillators describes the observed behaviour of the natural and actuated states as well as the transients between them, described by properties (i)-(iv).

$$\dot{a}_1 = \tilde{\sigma}^n a_1 - \omega^n a_2, \quad (4.4a)$$

$$\dot{a}_2 = \omega^n a_1 + \tilde{\sigma}^n a_2, \quad (4.4b)$$

$$\dot{a}_3 = \sigma^a a_3 - \omega^a a_4 + g B \cos(\theta + \beta), \quad (4.4c)$$

$$\dot{a}_4 = \omega^a a_3 + \sigma^a a_4 + g B \sin(\theta + \beta), \quad (4.4d)$$

$$\tilde{\sigma}^n = \sigma^n - \sigma^{n,n} (A^n)^2 - \sigma^{n,a} (A^a)^2. \quad (4.4e)$$

The reader is reminded that these equations are analytically justified and derived from the Navier-Stokes equation in § 2.3.3. For a qualitative discussion, the identified parameters of table 4.1 on page 90 are adopted. Figure 4.3 shows a solution of (4.4) for an actuated transient from natural to actuated state with periodic forcing starting at time  $t = 0$ . The qualitative behaviour is as expected, exhibiting a decaying natural oscillation and an excited forced one. The competition between natural and actuated oscillators can be inferred from (4.4e). During a slow transient, the time derivatives of the amplitudes  $A^n$  and  $A^a$  are arbitrarily small and can be neglected, including  $\tilde{\sigma}^n = 0$ . Thus, the dependency between both amplitudes is described by

$$\sigma^n = \sigma^{n,n} (A^n)^2 + \sigma^{n,a} (A^a)^2. \quad (4.5)$$

The associated energies are linearly related. One energy can only increase at the expense of the other. The lift coefficient can be considered as a function of either amplitude, see § 2.4 and in particular (2.101). From URANS data, it is observed to increase with the amplitude of actuation.



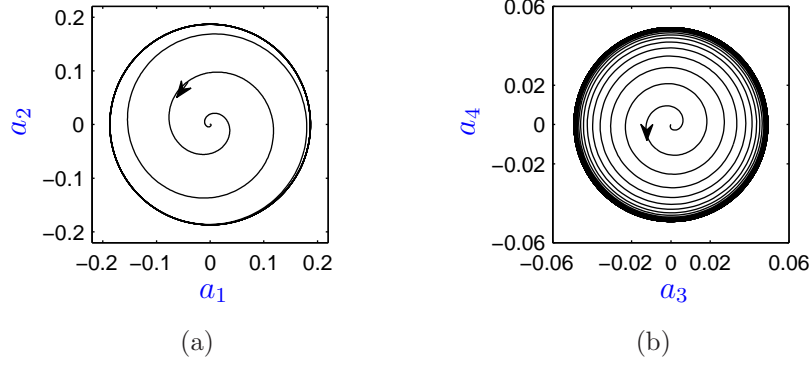


Figure 4.3: Solution of the model problem (4.4) starting from the initial condition  $[a_1, a_2, a_3, a_4] = [0.187, 0, 0, 0]$  with actuation. The left subfigure (a) displays the phase portrait of the natural oscillator  $(a_1, a_2)$ . Likewise, the right subfigure (b) displays the phase portrait  $(a_3, a_4)$  of the actuated oscillator.

Figure 4.4 shows the increase of  $A^a$  under forcing (subfigure a), corroborates approximately (4.5) (see the quarter ellipse in subfigure b) — even for a fast transient — and shows the increase of the lift during the transient (subfigure c).

## 4.5 Mean-field Galerkin model

In this section, the Galerkin mean-field model for two frequencies (see § 2.3.4) is adopted to describe the URANS simulation data.

The Galerkin approximation builds on the assumption NSE 1 in § 2.3.3. Thus, expansion modes are needed which resolve the three flow contributions  $\mathbf{u}^B$ ,  $\mathbf{u}^n$ , and  $\mathbf{u}^a$  in (2.94). Optimal resolution of  $\mathbf{u}^n$  and  $\mathbf{u}^a$  over the natural and the actuated attractors, where these fluctuations are respectively most prominent, is achieved by POD expansions. Let  $\mathbf{u}_i^n$  and  $\mathbf{u}_i^a$ ,  $i = 1, 2$ , be the dominant POD modes of these two attractors. These four modes are comprised in an orthonormal basis  $\{\mathbf{u}_i\}_{i=1}^4$  via Gram-Schmidt normalization, so that  $\mathbf{u}_i = \mathbf{u}_i^n$ ,  $\mathbf{u}_{i+2} = \mathbf{u}_i^a$ ,  $i = 1, 2$ . As seen in figure 4.6, the modes  $\mathbf{u}_i^a$  reach peak fluctuation over and near the airfoil whereas the fluctuations represented by  $\mathbf{u}_i^n$  are concentrated further downstream. This fact, along with the differences in the respective wavelengths imply that the two mode pairs are nearly orthogonal, to begin with, and Gram-

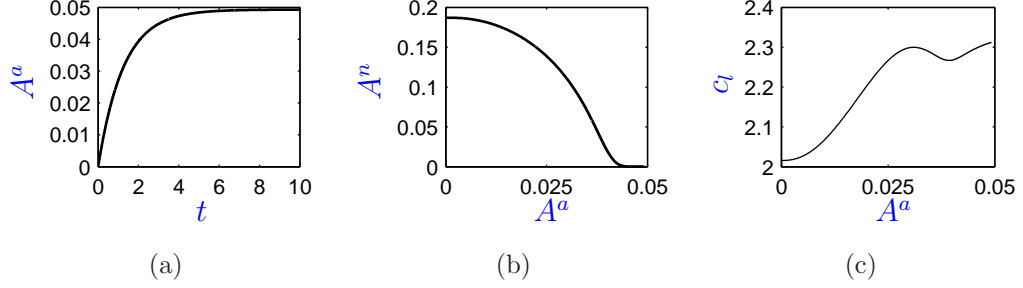


Figure 4.4: Amplitude and lift dynamics for the transient displayed in figure 4.3. Note that (a)  $A^a$  increases with time, (b)  $A^n$  decreases with increasing  $A^a$  and (c)  $c_l$  increases with increasing  $A^a$ . The non-monotonous behaviour of  $c_l(A^a)$  is an overshoot phenomenon related to the fast transient.

Schmidt orthogonalization hardly changes the POD modes. Therefore, as in (2.98), the association of the respective temporal amplitude pairs with the natural and the actuated frequencies is maintained:

$$\mathbf{a}^n = a_1 \mathbf{e}_1 + a_2 \mathbf{e}_2, \quad \mathbf{a}^a = a_3 \mathbf{e}_3 + a_4 \mathbf{e}_4,$$

and the following approximations are used

$$\mathbf{u}^n(\mathbf{x}, t) = \sum_{i=1}^2 a_i(t) \mathbf{u}_i(\mathbf{x}), \quad \mathbf{u}^a(\mathbf{x}, t) = \sum_{i=3}^4 a_i(t) \mathbf{u}_i(\mathbf{x}).$$

The mean of the natural and actuated attractor are denoted by  $\mathbf{u}_0^n$  and  $\mathbf{u}_0^a$  respectively. The time-varying base flow is approximated by two shift-modes corresponding to the two attractors of interest,

$$\mathbf{u}^B(\mathbf{x}, t) = \mathbf{u}_s(\mathbf{x}) + \mathbf{u}^\Delta(\mathbf{x}, t) = \mathbf{u}_s(\mathbf{x}) + a_5(t) \mathbf{u}_5(\mathbf{x}) + a_6(t) \mathbf{u}_6(\mathbf{x}), \quad (4.6)$$

where  $\{\mathbf{u}_i\}_{i=5}^6$  are derived by a Gram-Schmidt orthogonalization from  $\mathbf{u}_\Delta^n \propto \mathbf{u}_0^n - \mathbf{u}^s$  and  $\mathbf{u}_\Delta^a \propto \mathbf{u}_0^a - \mathbf{u}^s$ , removing also any projection over  $\{\mathbf{u}_i\}_{i=1}^4$ . The mode amplitudes of the two shift-modes are also collected in a column vector,

$$\mathbf{a}^B = a_5 \mathbf{e}_5 + a_6 \mathbf{e}_6.$$

The two mean flows  $\mathbf{u}_0^n$  and  $\mathbf{u}_0^a$  are approximated by time-averaging the velocity field of the natural and actuated attractor, respectively. Thus, the relevant linear

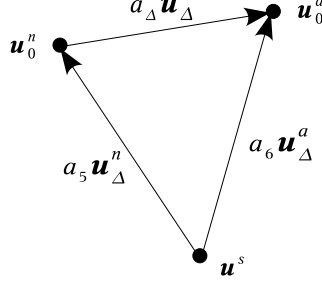


Figure 4.5: The relation between the steady solution and mean flows corresponding to the natural and actuated attractor. The steady solution  $\mathbf{u}^s$ , the mean of the natural flow  $\mathbf{u}_0^n$  and actuated pendant  $\mathbf{u}_0^a$  are depicted as solid circles. The shift-modes  $\mathbf{u}_\Delta^n$ ,  $\mathbf{u}_\Delta^a$  are the vectors pointing from the steady solution to the natural and actuated mean flow, respectively. The normalized difference between the actuated and natural mean flows, denoted by  $\mathbf{u}_\Delta$ , corresponds to the shift-mode in figure 4.6 (b).

approximation of the base flow is

$$\mathbf{u}^B(\mathbf{x}, t) = \mathbf{u}_0^n(\mathbf{x}) + a_\Delta(t) \mathbf{u}_\Delta(\mathbf{x}), \quad (4.7)$$

where  $\mathbf{u}_\Delta = (\mathbf{u}_0^a - \mathbf{u}_0^n) / \|\mathbf{u}_0^a - \mathbf{u}_0^n\|_\Omega$ . Figure 4.5 provides a schematic depiction of the relation between the steady solution and the mean flows corresponding to the natural and actuated attractor.

The actual computation of  $\{\mathbf{u}_i\}_{i=5}^6$  necessitates the difficult extraction of an unstable steady solution. In fact, these modes were not explicitly computed. Invoking (4.7) instead of (4.6), the velocity field of the URANS data is approximated by the expression

$$\mathbf{u}(\mathbf{x}, t) = \mathbf{u}_0^n(\mathbf{x}) + a_\Delta(t) \mathbf{u}_\Delta(\mathbf{x}) + \sum_{i=1}^4 a_i(t) \mathbf{u}_i(\mathbf{x}). \quad (4.8)$$

Although this approximation differs from the formal ansatz (4.6) with both shift modes, the Galerkin approximation (2.94) and corresponding Galerkin system (2.96) are used to describe the URANS data. Since the Galerkin system coefficients will be obtained by a calibration method using empirical data, the main purpose of (2.94) is to understand the implications on simplifying special aspects

of the structure of the Galerkin system, that will be utilized to facilitate system parameter estimation.

The decomposition (4.8) of the velocity field is schematically illustrated in figure 4.6. On the left, the mean of the natural and actuated flow,  $\mathbf{u}_0^n$  and  $\mathbf{u}_0^a$  respectively, along with the connecting (normalized) shift-mode  $\mathbf{u}_\Delta \propto \mathbf{u}_0^n - \mathbf{u}_0^a$  are shown. Modes representing the fluctuations are depicted on the right. Those include the first two POD modes of the natural and actuated attractor,  $\mathbf{u}_{1,2}$  and  $\mathbf{u}_{3,4}$  respectively. The phase portrait of the temporal amplitudes  $a_i$  is shown in the middle. A model based on this approximation accommodates the key physical phenomena of interest, including the natural and actuated limit cycles with their respective base flows, and transients between them. During an actuated transient, the coefficients representing the natural oscillator decay from their natural values to (near) zero at the actuated attractor, whereas the coefficients corresponding to the actuated oscillator grow from zero to their values on the actuated attractor.

The periodic actuation on the upper side of the trailing edge flap can be modelled by an actuation mode, as described in § 2.2.4, that is included in the Galerkin approximation (2.94). For the current case, it is assumed that the equivalent volume force is contained in the POD modes 3 and 4 which resolve the locked-in actuator. The control command of the actuator is oscillatory with slowly varying periodic characteristics. In this case, the effect of forcing on the flow is often modelled by a forcing term  $\mathbf{B} \mathbf{b}$  with actuation command  $\mathbf{b}$ , as e.g. in Rowley & Juttijudata (2005); Samimy *et al.* (2007); Siegel *et al.* (2003). This example is followed and a constant matrix  $\mathbf{B}$  is introduced (see (2.46)). The periodic actuator in (4.1) with velocity  $b = B \cos(\beta)$  satisfies  $d\beta/dt = \Omega^a$  with a slowly varying amplitude  $B$  and phase shift  $\beta = \Omega^a t$ . The acceleration reads  $db/dt = -\Omega^a B \sin(\beta)$ . As in (2.45), the command and its derivative are comprised in a vector

$$\mathbf{b} \stackrel{\text{def}}{=} \begin{bmatrix} b \\ -\frac{db/dt}{\Omega^a} \end{bmatrix} = B \begin{bmatrix} \cos(\beta) \\ \sin(\beta) \end{bmatrix}.$$

This convention allows to identify time and phase shifts in the control vector.

Following the literature, it is assumed that the same form of the mean-field model which was derived for the Navier-Stokes equation in § 2.3.3 and § 2.3.4 can

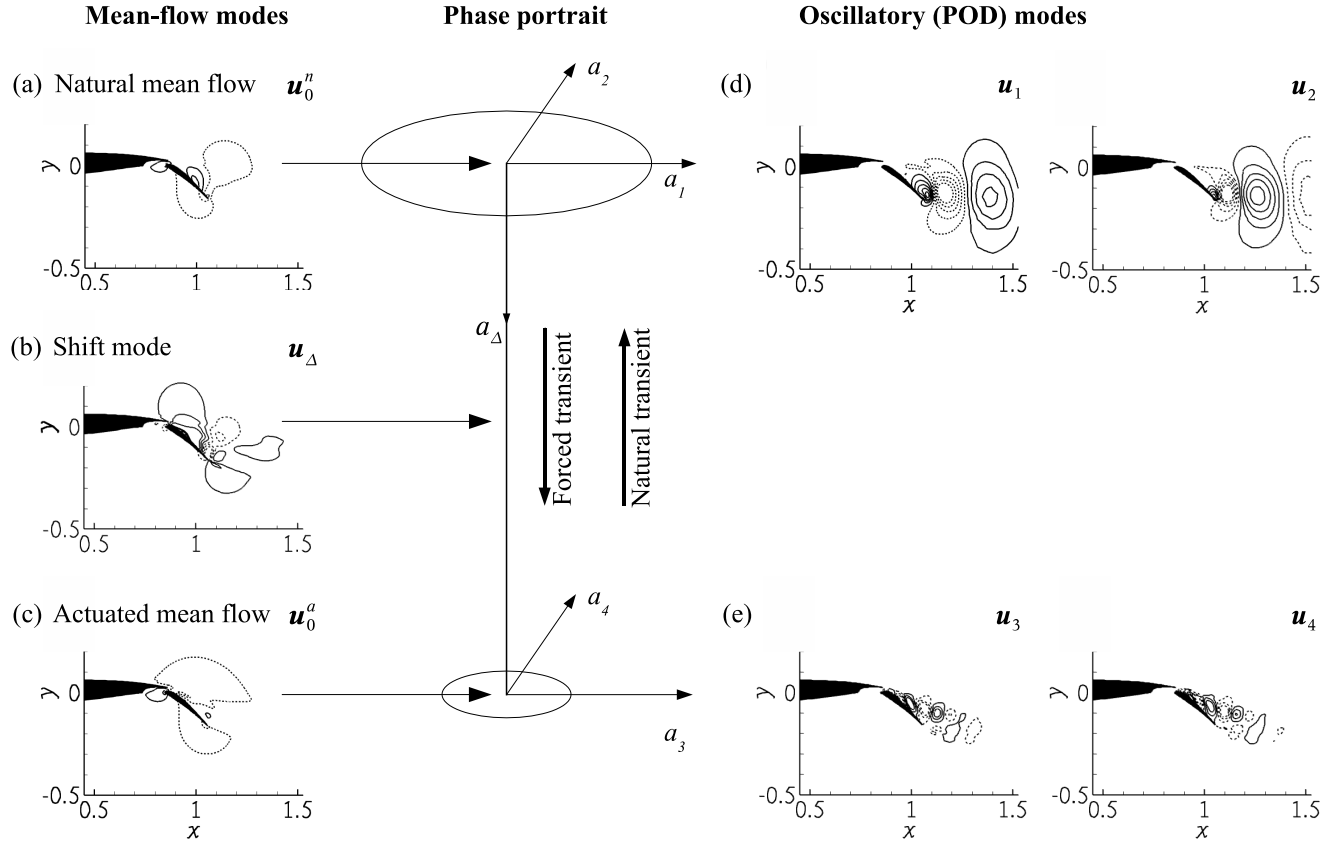


Figure 4.6: Principal sketch of the dynamics of the natural and actuated flow around a high-lift configuration. The flow is visualized by contour lines of the vertical velocity component, where continuous (dashed) lines indicate positive (negative) values. The depicted domain is the observation region indicated in figure 4.1. On the left, the mean fields of the natural (a) and actuated flow (c) are depicted. The shift-mode  $\mathbf{u}_\Delta$  (b) is the normalized difference between them. On the right, the POD modes  $\mathbf{u}_1$ ,  $\mathbf{u}_2$  of the natural- (d) and of the actuated flow  $\mathbf{u}_3$ ,  $\mathbf{u}_4$  (e) are visualized. The middle column shows the phase portrait of the model, where the natural (actuated) attractor is depicted as the limit cycle spanned by  $a_1$ ,  $a_2$  ( $a_3$ ,  $a_4$ ). The actuated transient is from top to bottom and the natural transient vice versa.

also be employed for the URANS equations, i.e. repeating (2.100) and (2.97), we have

$$\frac{dA^n}{dt} = \tilde{\sigma}^n A^n, \quad (4.9a)$$

$$\frac{d\alpha^n}{dt} = \tilde{\omega}^n, \quad (4.9b)$$

$$\frac{dA^a}{dt} = \tilde{\sigma}^a A^a + gB \cos(\beta + \theta - \alpha^a), \quad (4.9c)$$

$$\frac{d\alpha^a}{dt} = \tilde{\omega}^a + \frac{gB}{A^a} \sin(\beta + \theta - \alpha^a), \quad (4.9d)$$

where

$$\begin{aligned} \tilde{\sigma}^n &= \sigma^n - \sigma^{n,n} (A^n)^2 - \sigma^{n,a} (A^a)^2, \\ \tilde{\omega}^n &= \omega^n + \omega^{n,n} (A^n)^2 + \omega^{n,a} (A^a)^2, \\ \tilde{\sigma}^a &= \sigma^a - \sigma^{a,n} (A^n)^2 - \sigma^{a,a} (A^a)^2, \\ \tilde{\omega}^a &= \omega^a + \omega^{a,n} (A^n)^2 + \omega^{a,a} (A^a)^2. \end{aligned} \quad (4.10)$$

Indeed, most POD models follow the URANS turbulence modelling philosophy by incorporating fine-scale fluctuations via one additional eddy viscosity (Aubry *et al.*, 1988; Ukeiley *et al.*, 2001), or via a modal eddy viscosity distribution (Couplet *et al.*, 2003; Rempfer & Fasel, 1994). Some authors, e.g. Galletti *et al.* (2004), add a calibrated linear term. All these auxiliary models affect only the coefficients of the linear term, not the very form of the Galerkin system. The issue of turbulence modelling is re-visited in § 4.8.1.

### 4.5.1 Simplification of the dynamical system

In this section, the dynamical system (4.9) is analyzed in more detail. The assumed phase invariance and lock-in of the actuation response enable a notational simplification of the system. The discussion leads to algebraic constraints of the system parameters.

On the two attractors, the time derivatives of the amplitudes in (4.9a) and (4.9c) must vanish, and the right-hand side terms of (4.9b) and (4.9d) must be equal to the respective steady state shedding frequency and the actuation frequency. The steady state value of  $A^n$  on the natural (respectively actuated) attractor are denoted by  $A^{n,n}$  (respectively  $A^{a,a}$ ). According to assumption NSE

1 in § 2.3.3, the natural harmonic vanishes under forcing and the actuation harmonic vanishes without forcing. Hence, the values of  $A^n$  on the actuated attractor and of  $A^a$  on the natural attractor are set to zero.

The converged amplitudes on the natural and the actuated attractor, i.e.  $dA^n/dt = 0$  and  $dA^a/dt = 0$ , respectively, lead to the following equations

$$0 = \sigma^n - \sigma^{n,n} (A^{n,n})^2, \quad (4.11a)$$

$$0 = (\sigma^a - \sigma^{a,a} (A^{a,a})^2) A^{a,a} + gB \cos(\beta + \theta - \alpha^a). \quad (4.11b)$$

The lock-in property implies  $d\alpha^a/dt = d\beta/dt = \Omega^a$  on the actuated attractor. Thus,  $\beta + \theta - \alpha^a$  is constant in (4.11b) and in (4.12b), below.

The constant frequency conditions yield

$$\Omega^n = \tilde{\omega}^{n,n}, \quad (4.12a)$$

$$\Omega^a = \tilde{\omega}^{a,a} + \frac{gB}{A^{a,a}} \sin(\beta + \theta - \alpha^a), \quad (4.12b)$$

where again, the notation  $\tilde{\omega}^{n,n}$  stands for the steady state value of  $\tilde{\omega}^n$  on the natural attractor and  $\tilde{\omega}^{a,a}$  for the actuated attractor value of  $\tilde{\omega}^a$ .

Equation (4.12b) is simplified by assuming that the oscillation frequencies are independent of  $A^a$  and  $A^n$  and that the flow locks in with the actuation frequency  $\omega^a$ . In other words, the coefficients describing amplitude dependent frequency changes vanish:

$$\omega^{n,n} = \omega^{n,a} = \omega^{a,a} = \omega^{a,n} = 0. \quad (4.13)$$

The approximation  $\omega^{n,n} = \omega^{n,a} = 0$  appears admissible for the vortex-shedding frequency from dead-water zones with well defined transverse extent. Typically, frequency changes are at most of the order of 10%. The equation  $\omega^{a,n} = \omega^{a,a} = 0$  is implied by the assumed lock-in. Thus,

$$\tilde{\omega}^n = \omega^n = \Omega^n, \quad (4.14a)$$

$$\tilde{\omega}^a = \omega^a = \Omega^a, \quad (4.14b)$$

$$\theta = \alpha^a - \beta. \quad (4.14c)$$

In particular,  $\cos(\beta + \theta - \alpha^a) = 1$  on the actuated attractor, hence in (4.11b).

### 4.5.2 Parameter identification

The parameters of the least-order model are identified by calibration with simulation data. For that purpose a data trajectory is used that involves step changes in the actuation, as described in § 4.6, below. That reference was selected as a generic example of open-loop actuation. It is noted that abrupt transients present an inherent challenge for low-order models, due to the fact that they tend to involve far richer dynamics than what can ideally be represented, say, by a mere single mode pair per frequency. In particular, transient data has limited value to the calibration procedure, necessitating some added simplification in the model, as discussed in the previous section (equation (4.13)). In view of this, the success demonstrated in § 4.6 illustrates the robustness of the proposed modelling concept, corroborating its fundamental underpinning in the physics of the system.

The system (4.9), with state dependent coefficients given by (4.10), contains 14 unknown parameters:  $\sigma^n$ ,  $\sigma^{n,n}$ ,  $\sigma^{n,a}$ ,  $\omega^n$ ,  $\omega^{n,n}$ ,  $\omega^{n,a}$ ,  $\sigma^a$ ,  $\sigma^{a,n}$ ,  $\sigma^{a,a}$ ,  $\omega^a$ ,  $\omega^{a,n}$ ,  $\omega^{a,a}$ ,  $g$ , and  $\theta$ . Using the results of the previous section, equations (4.11), (4.13) and (4.14), this number reduces to seven. These remaining degrees of freedom ( $\sigma^n$ ,  $\sigma^{n,n}$ ,  $\sigma^{n,a}$ ,  $\sigma^a$ ,  $\sigma^{a,n}$ ,  $\sigma^{a,a}$ ,  $g$ ) are estimated from (4.9), using transient amplitude data. Specifically, the parameters are selected as the solutions of the following least square problems

$$\min \int_{t_0}^{t_1} \left[ \frac{dA^n}{dt} - \tilde{\sigma}^n A^n \right]^2 dt, \quad (4.15a)$$

$$\min \int_{t_0}^{t_1} \left[ \frac{dA^a}{dt} - \tilde{\sigma}^a A^a - g B \cos(\beta + \theta - \alpha^a) \right]^2 dt, \quad (4.15b)$$

subject to the algebraic constraints (4.11).

In summary, the algorithm for determining the parameters of the least-order Galerkin system is as follows:

- (i) Natural frequency ( $\omega^n$ ,  $\omega^{n,n}$ ,  $\omega^{n,a}$ ): The parameters are algebraically determined by (4.13) and (4.14a).
- (ii) Actuated frequency ( $\omega^a$ ,  $\omega^{a,n}$ ,  $\omega^{a,a}$ ): These parameters are determined by (4.13) and (4.14b).



## 4.6 Comparison of the Galerkin model with the URANS simulation

---

- (iii) Growth-rate of the fluctuation at natural frequency  $(\sigma^n, \sigma^{n,n}, \sigma^{n,a})$ : The coefficients determining the growth rate  $\tilde{\sigma}^n$  are constrained by (4.11a). This constraint is used to express  $\tilde{\sigma}^n$  in terms of  $\sigma^n$  and  $\sigma^{n,a}$ , i.e.  $\tilde{\sigma}^n(\sigma^n, \sigma^{n,a})$ . A transient part of the trajectory is used to determine  $\sigma^n$  and  $\sigma^{n,a}$  by a least square fit (4.15a).
- (iv) Growth-rate of the fluctuation at the actuated frequency  $(\sigma^a, \sigma^{a,n}, \sigma^{a,a})$  and actuation gain  $(g)$ : The coefficients determining the growth rate  $\tilde{\sigma}_a$  and the gain  $g$  are constrained by (4.11b). The expression for the rate is simplified to  $\tilde{\sigma}^a = \sigma^a$ , i.e.  $\sigma^{a,n} = \sigma^{a,a} = 0$ . Note that the lock-in assumption implies a fixed phase difference  $\theta = \alpha^a - \beta$ . Hence, the control term is zero without actuation and  $g B$  under actuation. This means that constraint (4.11b) simplifies to  $0 = \sigma^a A^{a,a} + g B$ . This constraint is used to express  $\tilde{\sigma}^n$  in terms of  $\sigma^a$ . A transient part of the trajectory is used to determine  $\sigma^a$  by a least square fit (4.15b).

## 4.6 Comparison of the Galerkin model with the URANS simulation

The Galerkin model derived in § 2.3.4 is compared with the empirical data from a transient URANS simulation. This comparison includes the Galerkin approximation of the flow field (§ 4.6.1), the Galerkin system for the dynamics (§ 4.6.2), and the lift coefficient (§ 4.6.3).

### 4.6.1 Galerkin approximation of the transient simulation

Here, the transient URANS data are analyzed. The snapshots of the velocity field are Galerkin approximated as in (4.7). The shift-mode amplitude  $a_\Delta$  is shown in figure 4.7. The amplitude indicates how the mean flow changes from the value at the natural attractor. As actuation is turned on, the mean flow changes, and settles at the actuated attractor. At the same time the mode amplitudes  $(a_1, a_2)$ , corresponding to the first oscillator, decrease to near-zero at the actuated attractor, see figure 4.8(a). The coefficients of the second oscillator  $(a_3, a_4)$ , are

## 4.6 Comparison of the Galerkin model with the URANS simulation

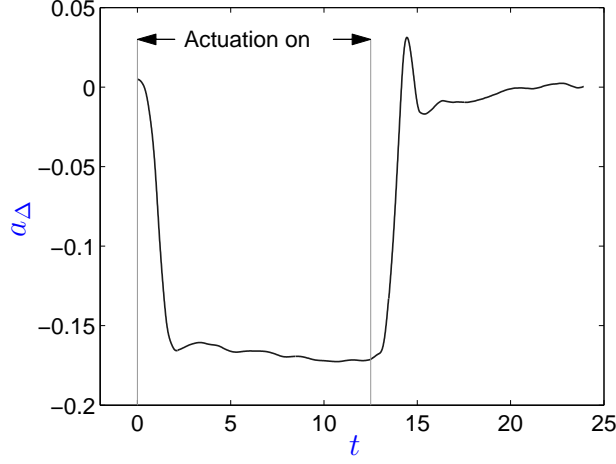


Figure 4.7: The shift-mode amplitude  $a_\Delta$  as obtained from projection of the velocity snapshots onto the modes. Actuation is switched on at  $t = 0$  and is switched off at  $t = 12.5$ .

excited by the periodic actuation, see figures 4.8(a) and 4.8(b). If actuation is turned off, the roles of both coefficient pairs are reversed. This behaviour is also elucidated in the principal sketch in figure 4.6.

### 4.6.2 Least-order Galerkin model of the transient data

In this section, the URANS data are compared with the least-order Galerkin model prediction (4.9). The mode amplitudes that result from projection onto the Galerkin expansion are used as a database for the calibration. The values of the model parameters are given in table 4.1. These parameters yield growth and decay rates in (4.9) that are bounded at  $|\tilde{\sigma}^n| < 10$  and  $|\tilde{\sigma}^a| < 1$ . An order of magnitude estimation using equation (4.9a), which has an exponential solution at a fixed instant in time, shows that the decay rate must be large to describe the steep descent, thus explaining the high values in table 4.1. These values of the rate coefficients in the table are due the fast convection of the structures in the observation region (see figure 4.1) and the short transients.

The phase portraits as predicted by time integration of the least-order Galerkin model are shown in figures 4.8(c) and 4.8(d) and can be compared with the projected values from the URANS simulation in the first row of figure 4.8. A compar-

#### 4.6 Comparison of the Galerkin model with the URANS simulation

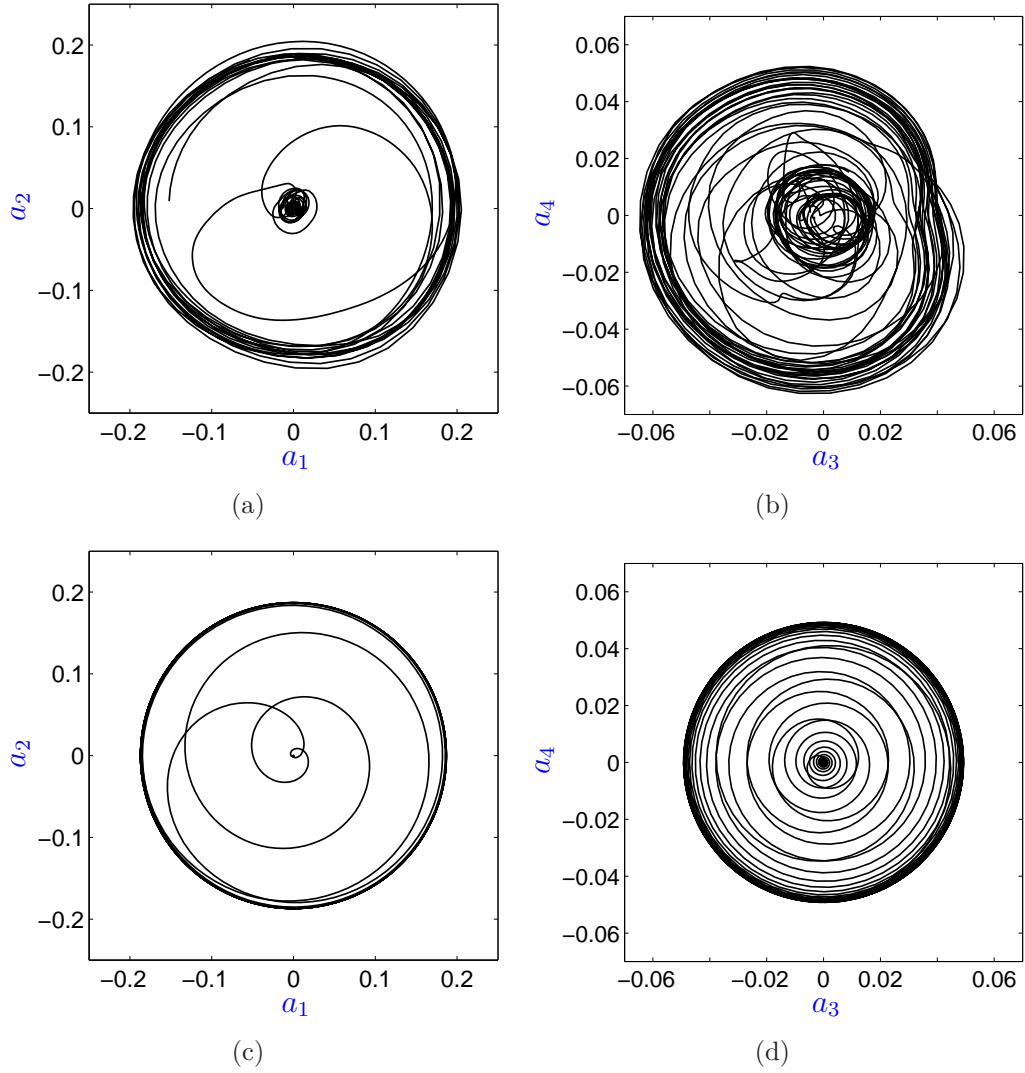


Figure 4.8: Phase portraits of the URANS simulation (a,b) and the least-order Galerkin model (c,d). The left column (a,c) shows the trajectory  $(a_1, a_2)$ , the right (b,d) shows the trajectory  $(a_3, a_4)$  associated with the natural and actuated flow.

## 4.6 Comparison of the Galerkin model with the URANS simulation

---

	parameter	value
linear dynamics	$\omega^n$	7.92
	$\omega^a$	14.85
	$\sigma^n$	10.00
	$\sigma^a$	-0.80
mean-field effects	$\sigma^{n,n}$	286.0
	$\sigma^{n,a}$	8243.0
	$\omega^{n,n}$	0.0
	$\omega^{n,a}$	0.0
	$\sigma^{a,n}$	0.0
	$\sigma^{a,a}$	0.0
	$\omega^{a,n}$	0.0
	$\omega^{a,a}$	0.0
actuation	$g$	$2.06 \cdot 10^{-2}$
	$\theta$	-3.69

Table 4.1: Identified parameters for the generalized mean-field model (see (4.9)). The actuation amplitude  $B = 1.91$  is determined by the URANS configuration.

## 4.6 Comparison of the Galerkin model with the URANS simulation

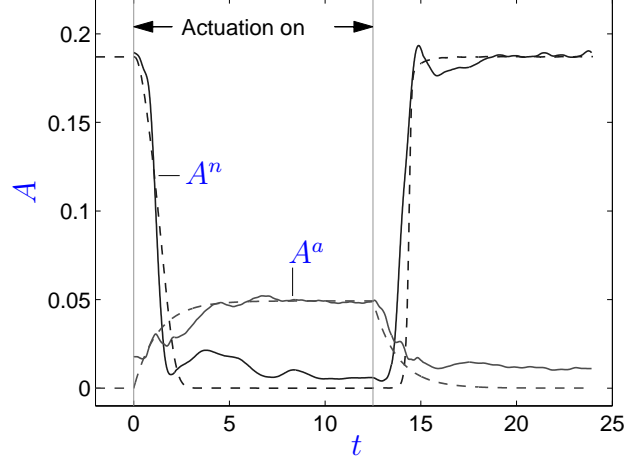


Figure 4.9: The amplitudes  $A^n$  and  $A^a$  of the URANS data (continuous lines) and the predictions by the least-order Galerkin model (dashed lines) in dependency of the time. Actuation is switched on at  $t = 0$  and is switched off at  $t = 12.5$ . The URANS values are low-pass filtered.

ison of the behaviour of the low-pass filtered amplitudes  $A^n$  and  $A^a$  from URANS data and integration of (2.100) are shown in figure 4.9. A good agreement is achieved. However, the natural attractor of the URANS simulation has a small residual level in  $A^a$  relative to  $A^n$ . According to assumption NSE 1, the actuation harmonic vanishes without forcing. Hence, this level vanishes in the model.

From figure 4.6, it can be seen that the dominant natural harmonic is mainly present after the flap in a large separation zone, whereas the actuated mode is active in a smaller region starting at the leading edge of the flap. The modes thus act as rivals, where only one can be fully alive in its own space.

Particularly important for flow control is the phase prediction by the model. The approximate lock-in on the actuated attractor is shown for mode amplitude  $a_3$  in figure 4.10.

### 4.6.3 Estimation of the lift coefficient

The model predictions can be related to quantities of engineering interest. As an example, the prediction of the lift coefficient by the model is shown. The lift coefficient will be inferred from the reduced order model in two ways. Following

## 4.6 Comparison of the Galerkin model with the URANS simulation

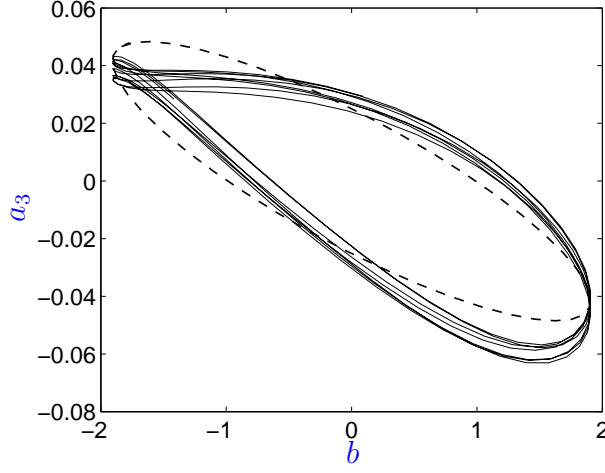


Figure 4.10: A phase portrait of the forced dynamics. Temporal amplitude  $a_3$  versus the actuation command  $b = B \cos(\beta)$ . The URANS data is shown by a continuous line and the least-order Galerkin model prediction by a dashed line. The approximate lock-in of URANS to the forcing frequency is clearly visible.

the overall pattern of this section, a calibrated polynomial expression based on the least-order Galerkin model is provided.

It is assumed that the lift coefficient is a function of the mode amplitudes  $c_l(a_1, \dots, a_4)$ . The oscillatory behaviour of the lift coefficient is modelled by a linear combination of  $a_1$ ,  $a_2$ ,  $a_3$  and  $a_4$ . The influence of the mean-field deformation during transients is taken into account by a Taylor series of second order in  $(A^n)^2$  and  $(A^a)^2$  (see equation (2.95c)).

Thus, the measurement equation for the lift coefficient is assumed to be of the following form

$$c_l(t) = c_{l0} + \sum_{i=1}^4 k_i a_i(t) + k_5 (A^n)^2 + k_6 (A^a)^2 + k_7 (A^n)^4 + k_8 (A^a)^4. \quad (4.16)$$

The first part of the functional form, up to the quadratic terms, follows directly from the Navier-Stokes equation. The two remaining fourth order terms are conjectured to account for unmodelled mode deformations. The parameters  $k_1, \dots, k_8$  obtained from a least squares fit from natural and actuated transients are listed in table 4.2.

## 4.6 Comparison of the Galerkin model with the URANS simulation

	parameter	value
linear dynamics	$c_{L0}$	2.05
	$k_1$	0.15
	$k_2$	-0.55
	$k_3$	-0.47
	$k_4$	0.70
mean-field effects	$k_5$	15.19
	$k_6$	212.31
	$k_7$	-436.00
	$k_8$	$-3.75 \cdot 10^4$

Table 4.2: Identified parameters of the measurement equation for the lift coefficient (see (4.16)).

The result is shown in figure 4.11, where the original lift coefficient is compared with the prediction of the model. The least-order Galerkin model performs surprisingly well. Prediction during fast transients (particularly, the second one) requires a more accurate dynamical model. In the following section, the lift formula is derived from first principles and compared with the identified formula.

### 4.6.4 Lift formula

The lift coefficient comprises a pressure and viscous contribution:

$$c_l = \frac{1}{1/2\rho(U_\infty)^2c} \left( - \int_{\Gamma} p \mathbf{n} dS + \nu \int_{\Gamma} \nabla \mathbf{u} \cdot \mathbf{n} dS \right) \cdot \mathbf{e}_y, \quad (4.17)$$

where  $\Gamma$  is the contour of the high-lift configuration,  $\mathbf{n}$  the outward normal vector and  $\mathbf{e}_y$  defines the direction of the lift.

The viscous contribution can easily be expressed in terms of the mode amplitudes by substituting the Galerkin approximation (2.37) in (4.17). The pressure field  $p$  is expanded into  $N$  modes  $p_i$  which are obtained from the  $M$  pressure snapshots  $p^m$  in complete analogy to the corresponding velocity snapshots  $\mathbf{u}^m$  at the same times. More specifically, let  $\mathbf{u}_i = \sum_{m=1}^M T_i^m \mathbf{u}^m$  be the formula of the POD snapshot method with the transformation matrix  $T_i^m$  of the observation region

## 4.6 Comparison of the Galerkin model with the URANS simulation

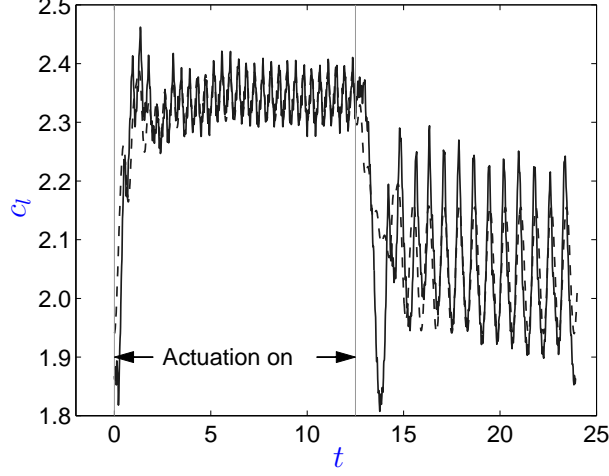


Figure 4.11: The original lift coefficient (continuous line) compared with the reconstructed lift coefficient (dashed line) based on the least-order Galerkin model. Actuation is switched on at  $t = 0$  and is switched off at  $t = 12.5$ .

in figure 4.1. Then the pressure mode is given by  $p_i = \sum_{m=1}^M T_i^m p^m$ . Physically, this corresponds exactly to the empirical pressure model of Noack *et al.* (2005), which is found to be a good approximation for all considered free shear flows, including shear-layers and wakes (Noack, 2006). The resulting expansions of the flow variables read

$$\mathbf{u}(\mathbf{x}, t) = \sum_{i=0}^N a_i(t) \mathbf{u}_i(\mathbf{x}), \quad (4.18a)$$

$$p(\mathbf{x}, t) = \sum_{i=0}^N a_i^p(t) p_i(\mathbf{x}), \quad (4.18b)$$

where  $a_0 \equiv 1$  and  $a_0^p \equiv 1$  by definition. Moving the mean pressure to the left side of (4.18b) and taking the spatial inner product on both sides, we have

$$(p_i(\mathbf{x}), p(\mathbf{x}, t) - p_0(\mathbf{x}, t))_{\Omega} = \sum_{j=1}^N (p_i(\mathbf{x}), p_j(\mathbf{x}))_{\Omega} a_j^p(t), \quad (4.19)$$

which is a matrix equation. This equation can be solved for the modal pressure amplitudes  $a_i^p(t)$  by inversion of the mass matrix  $(p_i(\mathbf{x}), p_j(\mathbf{x}))_{\Omega}$ . Thus, the lift



#### 4.6 Comparison of the Galerkin model with the URANS simulation

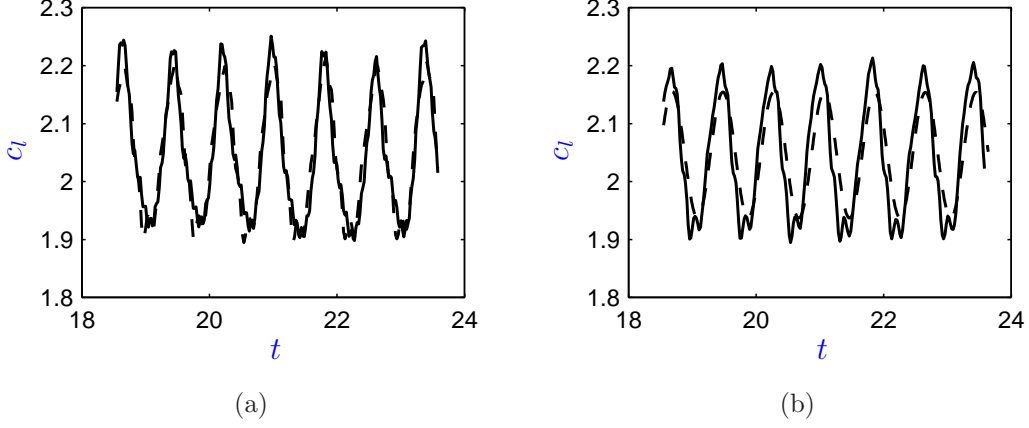


Figure 4.12: Comparison of the actual (URANS), modal (equation (4.20)) and identified lift coefficient (compare figure 4.11 and (4.16)) at the natural attractor: (a) actual (continuous line) and modal lift coefficient (dashed line), (b) modal (continuous line) and identified lift coefficient (dashed line).

coefficient can be written as

$$c_l(t) = \frac{1}{1/2\rho(U_\infty)^2 c} \sum_{i=0}^N \left\{ - \left( \int_{\Gamma} p_i(\mathbf{x}) \mathbf{n} dS \right) a_i^p(t) + \nu \left( \int_{\Gamma} \nabla \mathbf{u}_i(\mathbf{x}) \cdot \mathbf{n} dS \right) a_i(t) \right\} \cdot \mathbf{e}_y. \quad (4.20)$$

The modal lift coefficient is computed for  $N = 2$  at the natural attractor. The comparison of the actual (URANS) and modally decomposed lift coefficient is shown in figure 4.12(a). A good agreement is achieved with only two modes. Figure 4.12(b) shows the comparison of the modal and identified lift coefficient (see also figure 4.11). It can be seen that the identified lift coefficient is smoother than the modal one. This observation directly correlates with the temporal amplitudes of the velocity field, which are much smoother than the amplitudes of the pressure modes. The latter correlate better with the lift coefficient. The identified lift coefficient is in this sense the best approximation given the mode amplitudes of the velocity field. Most important for the purpose of the present discussion, the postulated linear dependence of the lift on the temporal amplitudes of the oscillatory fluctuations is now connected to an analytic derivation from the Navier-Stokes equation.

## 4.7 Set-point tracking of the lift coefficient

The sliding mode controller, described in § 2.4.1, is implemented for set-point tracking of the time-averaged lift coefficient  $c_l$  (see figure 4.13). Here, the time-averaged lift coefficient is written as a linear combination of the energy levels of the natural and actuated oscillators:

$$c_l = c_{l0} + c_1(A^n)^2 + c_2(A^a)^2. \quad (4.21)$$

The simplified dynamic system follows from the simplifications in § 4.5.1 and is slightly different from the one used in § 2.4.1:

$$\frac{dA^n}{dt} = (\sigma^n - \beta^n a_5 - \delta^n a_6) A^n, \quad (4.22a)$$

$$\frac{dA^a}{dt} = \sigma^a A^a + gB, \quad (4.22b)$$

$$\frac{da_5}{dt} = \rho ((A^n)^2 - a_5), \quad (4.22c)$$

$$\frac{da_6}{dt} = \eta ((A^a)^2 - a_6), \quad (4.22d)$$

where  $g$  is the coefficient corresponding to the time-varying actuation input  $B$ . Note from comparison with (4.9) that the last two equations for the base flow are not slaved to the fluctuation amplitudes. The coefficients  $\rho$  and  $\eta$  are chosen large compared to the growth rates  $\sigma^n$  and  $\sigma^a$ . In essence this amounts to slaving the the last two equations to the first two (i.e. set  $\dot{a}_5 = \dot{a}_6 \equiv 0$  and solve for  $a_5$  and  $a_6$ ). Hence the evolution equations (5.2c) and (5.2d) are merely dummy equations. The reason for this decoupling is convenient controller design based on the standard quadratic form of a Galerkin system. The corresponding sliding mode controller (compare with (2.106) and (2.104)) is given by

$$B_{sm} = B_{eq} - K \operatorname{sat} \left( \frac{s}{\psi} \right), \quad (4.23)$$

with the equivalent control law

$$B_{eq} = -\frac{c_1 (\sigma^n + \beta^n a_5 + \delta^n a_6) (A^n)^2}{c_2 A^a g} - \frac{\sigma^a A^a}{g}. \quad (4.24)$$

---

The work presented in § 4.7 was performed in close collaboration with Katarina Aleksić.

## 4.7 Set-point tracking of the lift coefficient

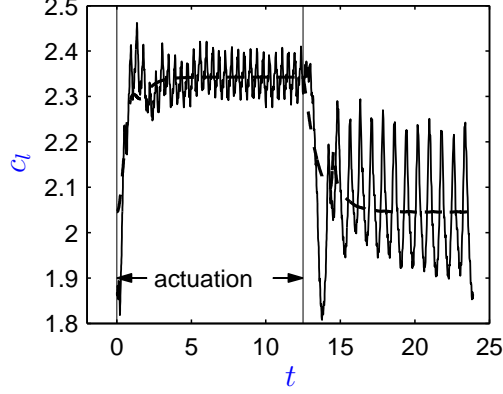


Figure 4.13: Evolution of the time-averaged lift coefficient under temporary high-frequency actuation. The open-loop controller is activated from  $t = 0$  to 12.5. Compare with figure 4.11.

Note that both amplitudes,  $A^n$  and  $A^a$ , are needed for computation of the control law  $B_{sm}$ . Here, it is assumed that only the lift coefficient can be directly measured. An extended Kalman filter (EKF) is used for state estimation.

As above, the flow is simulated using the unsteady Reynolds-averaged Navier-Stokes (URANS) equation. In contrast to the previous simulation, turbulence is now resolved by the  $k - \omega$  model by Wilcox (Wilcox, 1994). In addition, the flow is considered at a higher Reynolds number, namely  $Re = 1.75 \times 10^6$ . All other simulation parameters remain equal. The coefficients of the measurement equation (4.21) and dynamic system (4.22) are calibrated using URANS data from the new simulation. The coefficients are identified in an analogous manner as above in § 4.5.2 and § 4.6.3. The coefficients in equations (5.2c) and (5.2d) are respectively set to  $\rho = 10 \sigma^n$  and  $\eta = -10 \sigma^a$ . The identified parameters are listed in table 4.3. Figure 4.14 shows the closed-loop command tracking performance of the proposed sliding mode controller. The controlled system output  $c_l$  closely follows the step input reference command  $c_{l_{ref}} = 2.23$ . The desired lift coefficient is reached after approximately a half convective time unit. Note that the actuation input to the model  $B$  is simply a scaled version of the momentum coefficient  $c_\mu$  (compare the top and middle row of Fig. 4.14). The clipped control input is due to saturation of the lift coefficient at  $c_\mu = 2.0 \cdot 10^{-3}$ .

The expected robustness of the sliding mode controller for different angles of

	parameter	value
dynamic system	$\sigma^n$	100.00
	$\beta^n$	3086.40
	$\delta^n$	1519.10
	$\sigma^a$	-0.80
	$g$	0.064.00
	$\rho$	1000.00
	$\eta$	8.00
measurement equation	$c_{l0}$	0.6623
	$c_1$	40.3605
	$c_2$	241.5870

Table 4.3: Identified parameters for the dynamic system (4.22) and the measurement equation (4.21).

attack and for Reynolds number variations will be investigated in a future study.

## 4.8 Discussion

In this section, Galerkin modelling aspects are related to the pursued structure and parameter identification for turbulent flows represented by URANS data. In principle, the model should be derivable from the Navier-Stokes equation or from accurate DNS data. In practice, only URANS or PIV data may be available for turbulent flows and the mean-field considerations as well as the parameter identification require a more rigorous explanation. These modelling aspects include effects of turbulence (§ 4.8.1) and of non-equilibrium (§ 4.8.2).

### 4.8.1 Turbulence effects

The rationale of URANS simulations is that large-scale coherent structures are resolved in space and time while turbulent fluctuations at all scales are modelled via an eddy viscosity ansatz. This implies that the generalized Krylov-Bogoliubov

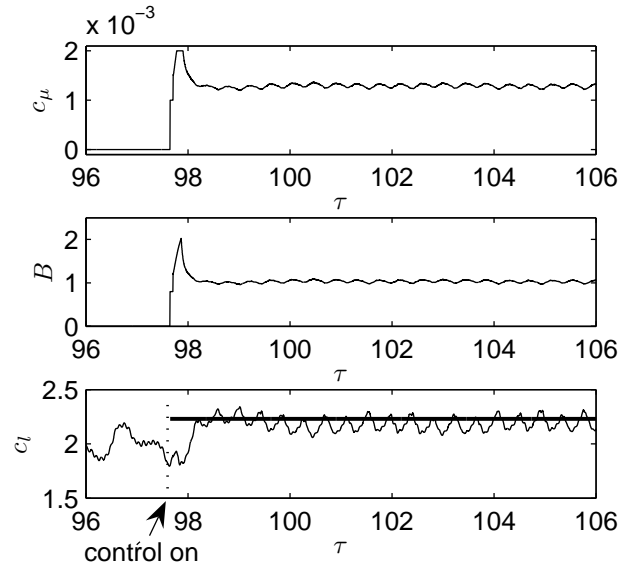


Figure 4.14: Reference tracking test of the lift coefficient using a sliding mode controller. The controller starts at  $t = 97.65$ . The lift coefficient (bottom), the control input to the model  $B$  (middle), and the excitation momentum coefficient  $c_\mu$  (top) are shown.

approximation (2.89) should be augmented with a term  $\mathbf{u}^t$  representing the contribution of small-scale dynamics:

$$\mathbf{u}(\mathbf{x}, t) = \mathbf{u}^B(\mathbf{x}, t) + \mathbf{u}^n(\mathbf{x}, t) + \mathbf{u}^a(\mathbf{x}, t) + \mathbf{u}^t(\mathbf{x}, t). \quad (4.25)$$

Small scale fluctuations are characterized by high-frequency behaviour which can be expected to be uncorrelated with the large-scale coherent structures. Assuming that to be the case,  $\mathbf{u}^t$  and products with it vanish under ensemble averaging and low-pass filtering. In particular, the filtered Navier-Stokes equations (2.92) and its derivations, are not effected by  $\mathbf{u}^t$ . This small-scale fluctuation is the difference between an accurate DNS and ideal URANS simulation.

However,  $\mathbf{u}^t$  acts as an energy sink in the evolution equations. In URANS and LES an eddy viscosity accounts for these losses. In POD Galerkin models, [Rempfer & Fasel \(1994\)](#) proposed modal eddy viscosities  $\nu_{T,i}$  to account for that effect — in analogy to spectral pendants:

$$\dot{a}_i = (\nu + \nu_{T,i}) \sum_{j=0}^N l_{ij} a_j + \sum_{j,k=0}^N q_{ijk} a_j a_k. \quad (4.26)$$

The modal eddy viscosity has a negligible effect on frequencies since  $l_{ij}$  is a diagonal matrix in good approximation.

A comparison of the Galerkin projected system and the identified system shows that the frequencies of both systems are similar at both the natural and actuated attractor. In contrast, the growth rates are not predicted correctly by the Galerkin projection. This is due to the neglected effect of turbulence, as described above.

In summary, neglecting the small-scale fluctuation is standard in reduced order models. This is expected neither to change the mean-field equations nor the derived structure of the least-order Galerkin system. The effect of this simplification is mostly restricted to growth rates, which can be corrected by careful calibration. This seems to be an acceptable price for the level of simplicity and physical insight associated with the reduced order model. In particular, a minimum number of free parameters makes this approach particularly suited for the evaluation of experimental PIV data.

### 4.8.2 Non-equilibrium effects

The steady solution is critical for the derivation of the standard and the presented generalized mean-field model. More specifically, the two shift modes that govern the nonlinear fluctuation growth rates are defined as the unit vectors pointing from the steady solution to the respective mean flows of the natural and the actuated attractors.

Thus, the knowledge of the steady solution is necessary for the derivation of the dynamical model from the Navier-Stokes equation. However, this unstable solution cannot be obtained from the URANS solver. Fortunately, the parameters governing the dynamical model can be estimated from URANS transient data (see § 4.5.2), and the steady solution as well as the shift modes are not needed. In a similar spirit, experimentalists have determined the constants of the Landau equation for the onset of vortex shedding without inquiring the Navier-Stokes equation.

Equation (4.7) serves as an auxiliary model to the mean-field system (2.96), where  $a_\Delta$  could be obtained as a fitted polynomial of the oscillation amplitudes  $A^n$  and  $A^a$ . Similarly, the lift coefficient (4.16) is embedded in the model by a fitted polynomial of the mode amplitudes  $a_1, \dots, a_4$  and the oscillation amplitudes.

## 4.9 Conclusions

A least-order Galerkin model has been applied to the flow around a high-lift configuration. This model provides a least-order representation of periodic fluctuations using a single pair of POD modes per frequency. The novelty in this model lies in the inclusion of modes representing mean-field variations due to natural and actuated fluctuations. These modes are the key enabler for capturing the attenuating effect of high-frequency actuation on the natural instability. Thus, the mean-field model explains the mediation between the fluctuations at the natural and the actuated frequencies.

Dynamics covered by the model include natural vortex shedding, the effect of high-frequency forcing, as well as actuated and un-actuated transients based on URANS data. The model captures the original URANS simulation surprisingly

well considering the very low order. The phase relation of flow and actuation of the URANS and least-order Galerkin model data is in good agreement. This agreement is important for flow control design. Model predictions include the lift coefficient which is also in good agreement with the original data. As can be expected, predictions by this least-order model erode during fast transients, and more accurate representation requires higher-order models. This applies, in particular, to prediction of the lift coefficient during fast transients.

A main advantage of the analytical model is the possibility of a simple and robust calibration of a given data set. Thus, the low-dimensional model can be used as a quick test-bed for explanatory studies in simulation and experiment. It was shown how a sliding mode controller can be used for improvement of open-loop control by closely tracking a prescribed lift coefficient.



# Chapter 5

## Stabilization of a bluff body wake

### 5.1 Abstract

The wake of a bluff body can be significantly influenced by open-loop periodic actuation at about 65% of the dominant natural vortex shedding frequency. The purpose of the current effort is to model these effects with a (simplified) mean-field Galerkin model for two frequencies. Subsequently, this model is employed for feedback control of the flow around a D-shaped body in a wind tunnel. The form of the model follows from the generalized mean-field consideration in § 2.3.3. Pressure measurements are used to identify the model parameters. The model is then used for design of a nonlinear controller. In particular, set-point tracking of the base pressure coefficient is illustrated using a sliding mode controller.

### 5.2 Introduction

The flow around a D-shaped body can serve as a benchmark problem for more complicated geometries like automobiles, ships etc. This flow is dominated by a geometry induced separation and can be characterized as a ‘wake flow’. The separated flow is accompanied by a large pressure loss at the stern of the body. The negative effect of the pressure induced drag can be alleviated by several means. Examples include passive devices like: turbulators, riblets, splitter plates,

---

The work presented in this chapter was performed in close collaboration with Katarina Aleksić.

but also active flow control solutions: base bleed, rotary oscillations, synthetic jets etc. (Choi *et al.*, 2008). A detailed study of the effectiveness of small size tabs for drag reduction is provided by Park *et al.* (2006). Modern flow control solutions typically include feedback, i.e. observations are used to provide feedback about the ‘success’ of the control and update the controller output accordingly. An example is the phase control described in Pastoor *et al.* (2008), which desynchronizes the opposite shear-layer dynamics, leading to postponed vortex formation and hence a drag reduction.

The objective of the current study is to explore the possibility of using a (simplified) mean-field model as a base for controller design for the flow around a D-shaped body in an experiment. This configuration is the same as the one studied by Pastoor *et al.* (2008). The wake of the bluff body exhibits a dominant frequency associated with large scale von Kármán-like vortices. In-phase open-loop forcing at the trailing edges at about 65% of the natural frequency can significantly increase the base pressure and, hence, reduce drag. The modified pressure distribution on the stern is accompanied by a notable change of the flow field. In particular, the mean flow is changed by active flow control. The recirculation region of the mean flow is elongated and the streamlines which curve around the time-averaged recirculation region suggest that the mean effective body which the flow ‘sees’ is more streamlined. The importance of base flow modification for drag reduction is supported by passive flow control methods. A popular method for bluff bodies is the so-called boat-tailed or conical afterbody concept, which is very effective in reducing base drag (Viswanath, 1996).

Based on the phenomenology of the natural and the periodically forced flow behind the D-shaped bluff body, it is assumed that a least-order model should at minimum include the oscillatory fluctuations at the natural and actuation frequency, and the effected base flow changes. In the spirit of the Reynolds-averaged Navier-Stokes equation, these observations lead to a model where the oscillations are nonlinearly coupled with the mean-flow through the Reynolds stresses. Along similar lines, a two-frequency mean-field model was proposed in the previous chapter and in Luchtenburg *et al.* (2009a) for a high-lift configuration, which is also expected to work for the present configuration. Dynamics covered by the model include natural vortex shedding, the effect of forcing, as well as actuated

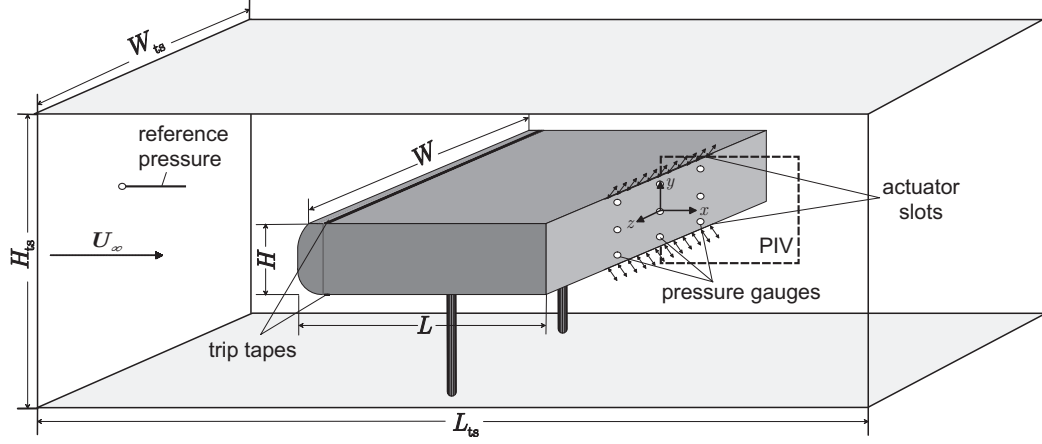


Figure 5.1: A sketch of the experimental setup with the D-shaped body. For details, see text. This figure is taken from [Pastoor \*et al.\* \(2008\)](#).

and un-actuated transients. Here, this model is used for a systematic feedback control design. It is sufficiently simple for feasible real-time implementation, and yet robustly represents the natural and actuated dynamics.

### 5.3 Experimental setup

We study the incompressible flow over a D-shaped bluff body (see figure 5.1). This configuration is employed in several experimental targeting active flow control ([Henning \*et al.\*, 2007](#); [Pastoor \*et al.\*, 2008](#)). The control goal in these studies is to decrease and stabilize drag. A detailed description of the experimental setup and the measurement equipment can be found in [Henning \(2008\)](#). All experiments are conducted in an Eiffel-type wind tunnel. The dimensions of the closed test section are  $L_{ts} = 2500$  mm,  $H_{ts} = 555$  mm and  $W_{ts} = 550$  mm in the streamwise, transverse and spanwise directions, respectively. The D-shaped body has the following dimensions: length  $L = 262$  mm, body height  $H = 72$  mm and spanwise width  $W = 550$  mm. Trip tapes are placed 30 mm downstream of the nose in order to trigger the laminar-turbulent boundary layer transition. The body is mounted on two aluminium rods and is vertically centered in the wind tunnel. The geometric blockage with the model in the wind tunnel is comparatively large at approximately 13%. Therefore, the free stream velocity  $U_\infty$  is adjusted

to  $U_{\infty,c} = U_{\infty} \sqrt{B_c}$ , according to the blockage correction method proposed by Mercker (1980). The Reynolds number and Strouhal number are defined as

$$Re = \frac{U_{\infty,c} H}{\nu} \quad \text{and} \quad St = \frac{f H}{U_{\infty,c}},$$

respectively. The maximum free stream velocity is approximately 20 m/s with a turbulence level of less than 0.5%. This allows Reynolds numbers that range from 23 000 to 70 000.

Flow control is achieved by actuators at the upper and lower trailing edges of the body. The actuators provide a sinusoidal zero-net-mass-flux through spanwise slots, that is effected by loudspeakers. The slot width is  $S = 1$  mm and the slots extend over a half spanwise length of 250 mm. The actuators are operated such that a periodic suction and blowing is achieved. The voltage signal to the loudspeakers is:  $u(t) = \hat{u} \cos(2\pi f^a t)$ , with the actuation amplitude  $\hat{u}$  and actuation frequency  $f^a$ . The actuation intensity is characterized by the nondimensional momentum coefficient

$$c_{\mu} = \frac{2S}{H} \frac{(q^a)^2}{U_{\infty,c}^2},$$

where  $q^a$  is the RMS value of the velocity signal that is effectuated at the exit of a slot.

The base pressure is monitored by  $3 \times 3$  difference pressure gauges mounted in three parallel rows on the stern at  $y = \{-32, 0, 32\}$  mm and  $z = \{-82.5, 0, 82.5\}$  mm. In this study, only values of the three gauges in the vertical symmetry plane at  $z = 0$  mm are reported. The pressure gauges are calibrated and temperature compensated. The free-stream dynamic pressure is monitored by a Prandtl probe upstream of the body. The drag of the body is measured by means of four strain gauges, which are attached to the aluminium rods. The base pressure and drag are described by the non-dimensional coefficients

$$c_p(y, z, t) = \frac{\Delta p}{\rho U_{\infty,c}^2 / 2},$$

$$c_D(t) = \frac{F_x}{\rho U_{\infty,c}^2 H W / 2},$$

where  $\Delta p$  is the instantaneous pressure difference between a stern-mounted pressure gauge and the reference pressure,  $\rho$  denotes the density, and  $F_x$  is the drag

force. Time-averaged base pressure and drag are denoted by  $\bar{c}_p(y, z)$  and  $\bar{c}_d$ , respectively. The spatially averaged base pressure over the stern is defined by  $\langle c_p(t) \rangle$ .

Time resolved PIV measurements<sup>1</sup> are conducted in the vertical symmetry plane ( $x \in [0, 144]$  mm,  $y \in [-58, 58]$  mm and  $z = 0$  mm) at  $Re_H = 46\,000$  with a spatial resolution of  $dx = dy = 1.8$  mm. The sample rate of the measurements is 1 kHz. The PIV-system consists of a Nd:YLF laser, a Photron APX-RS Camera and a synchronization unit. The *VidPiv* software of *ILA corp.* is used for the computation of velocity fields. Data acquisition and the implementation of the controllers is realized by rapid prototyping hardware. The sampling time is  $\Delta t = 1/1000$  s.

## 5.4 Characterization of the flow field

In this section, properties of the natural (§ 5.4.1) and periodically forced wake (§ 5.4.2) of the D-shaped body are highlighted. The flow is considered at a Reynolds number of  $Re = 46\,000$ .

### 5.4.1 Natural flow

The near wake of a two-dimensional bluff body is characterized by an absolute instability (see e.g. [Huerre & Monkewitz, 1990](#)). This instability is associated with the development of a von Kármán-like vortex street with alternating vortices at well defined frequencies. In the current setup, spanwise velocity variations, particularly the phase differences are small ([Pastoor \*et al.\*, 2008](#)). This indicates that the coherent structures in the flow field are primarily two-dimensional: the wake is dominated by an almost parallel vortex street.

Vortices leave typical footprints in pressure sensors: their centers are namely characterized by pressure minima. Therefore, shedding vortices can be clearly observed in pressure sensors at the upper- and lower edge of the bluff body, see figure 5.2. Since the vortices alternate periodically from both edges, the upper

---

<sup>1</sup>We thank Prof. W. Nitsche and M. Hecklau for making this data available and carrying out the measurements.

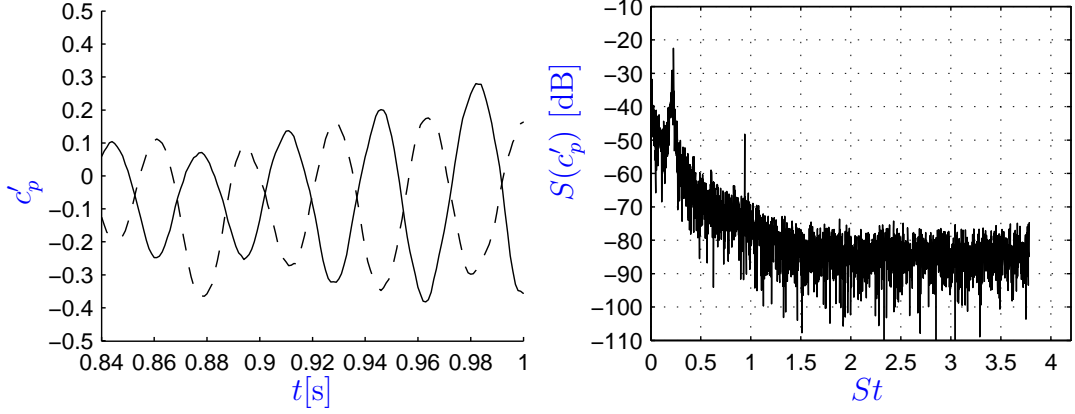


Figure 5.2: Left: fluctuation pressure coefficients of a sensor at the upper- (—) and lower edge (—) of the body; natural flow,  $Re = 46\,000$ . The spectrum of the lower sensor is shown in the right plot.

and lower pressure signal are  $180^\circ$  out of phase. The spectrum of the pressure signal at the lower edge reveals a distinct Strouhal number of  $St = 0.23$  (figure 5.2, right plot). This frequency is also predominant in the velocity field as is confirmed by a DMD analysis of the PIV snapshots. In figure 5.3 (top, left) the magnitudes of the DMD modes at each frequency are shown. The real and imaginary parts of the DMD mode that corresponds to  $St = 0.23$ , and their mode amplitudes are also plotted in figure 5.3. This mode is clearly associated with vortex shedding; the real and imaginary part of the mode are spatially shifted by about a quarter wave length. Together with the mode amplitudes, which are out of phase by a quarter period, they describe the oscillatory fluctuation of the velocity field at the vortex shedding frequency<sup>1</sup>.

The drag on the body is mainly due to the pressure loss associated with the wake and results in a relatively high average drag coefficient of  $\bar{c}_D = 0.90$ . The recirculation length of the mean flow is approximately one body height (figure 5.4). The reported values are in good agreement with literature, see e.g. Hucho (2002); Park *et al.* (2006).

<sup>1</sup>To illustrate this point: consider a traveling wave  $\cos(x - t)$ . This wave can be decomposed as:  $\cos(x - t) = \cos(t) \cos(x) + \sin(t) \sin(x)$ .

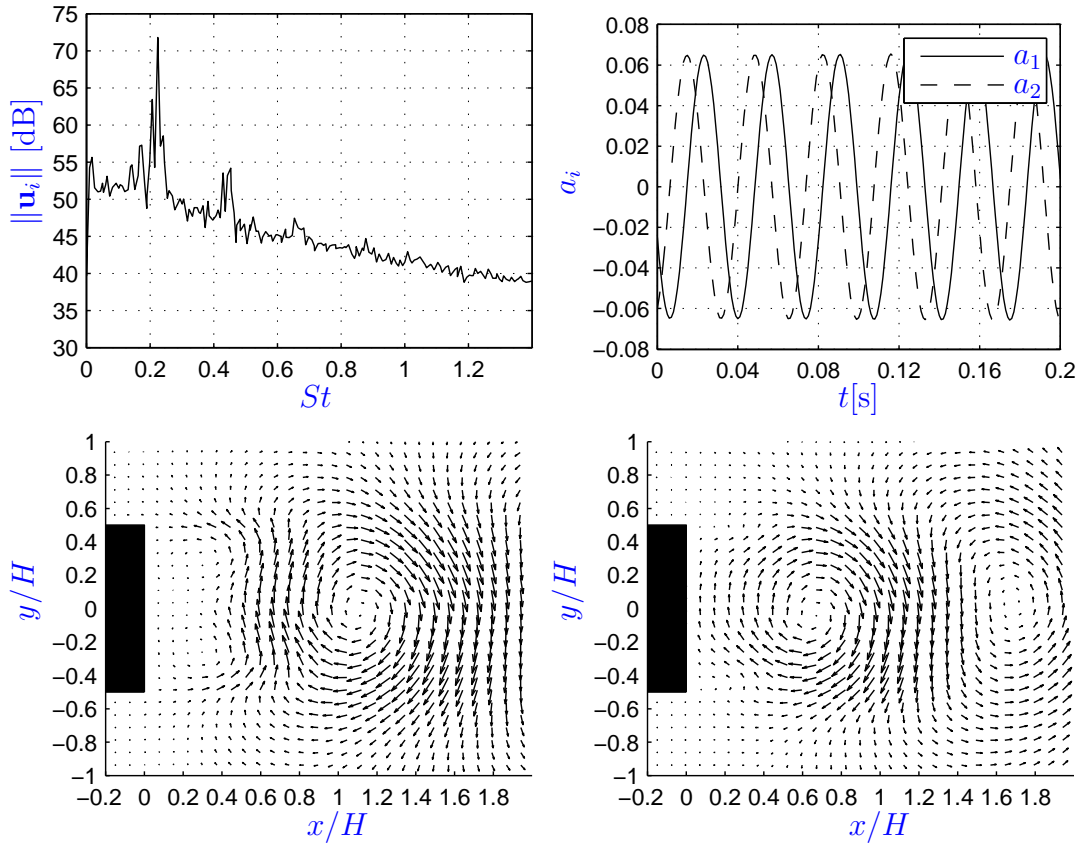


Figure 5.3: A spectral analysis of the natural velocity field at  $Re = 46\,000$ . Top, left: the magnitudes of the DMD modes as a function of their nondimensional frequency; right: the temporal amplitudes of the first DMD mode corresponding to  $St = 0.23$ . The bottom row shows the DMD mode. Left: the real part of the first mode, and right the imaginary part.

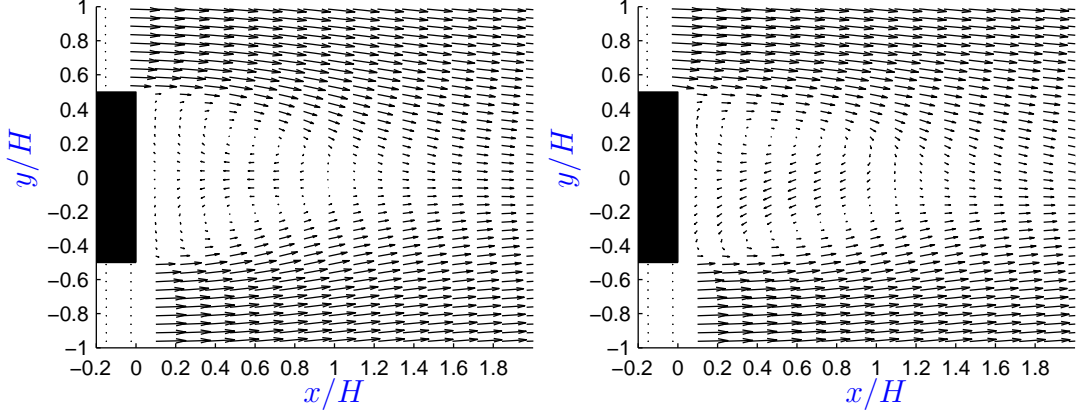


Figure 5.4: The time-averaged natural (left) and in phase actuated (right) flow at  $Re = 46\,000$ ;  $St^a = 0.15$ .

### 5.4.2 Periodically forced flow

In order to suppress the wake instability open-loop flow control is applied. The upper and lower actuators are operated in phase to desynchronize the shear-layer and wake dynamics. This leads to postponed vortex formation and hence reduces drag (Pastoor *et al.*, 2008). The optimal actuation Strouhal number is about  $St^a \approx 0.15$  for the range of Reynolds numbers:  $Re = 23\,000 - 46\,000$ . The maximum drag reduction that can be achieved is almost 15%. In figure 5.5, the pressure signals of an actuated flow with  $St^a \approx 0.15$  are shown. The voltage input to the actuator equals 5 V, which results in a mean drag reduction of about 9%. The actuation almost synchronizes the shedding of vortices at the upper and lower edge as can be inferred from the nearly in phase pressure readings. The spectrum of the pressure sensor at the lower edge reveals the nondimensional actuation frequency  $St^a = 0.15$ , the second harmonic, and a suppressed peak at the natural Strouhal number  $St^n = 0.23$ . As above, a spectral analysis is conducted for the PIV snapshots of the flow field. The result is summarized in figure 5.6. The structure of the DMD modes at the actuation frequency indicates that the actuator introduces two new coherent structures in the flow. These structures approximately scale with the half body height, since they are (nearly) shed in phase. It can also be observed that the upper actuator has a stronger effect on the flow than the lower one, which leads to a slightly asymmetric time-



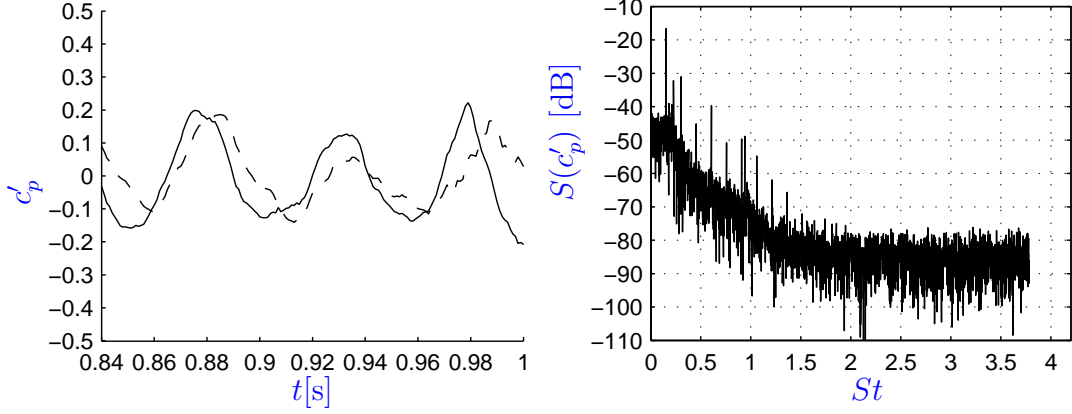


Figure 5.5: Left: fluctuation pressure coefficients of a sensor at the upper- (—) and lower edge (—) of the body; actuated flow at  $St^a = 0.15$ ,  $Re = 46\,000$ . The actuator amplitude of the loudspeaker is set to 5 V. The spectrum of the lower sensor is shown in the right plot.

averaged flow around the centerline, see the right plot of figure 5.4. Nonetheless, because of the in phase actuation, the wake ‘opens up’ since the shear layers roll up more downstream, and pressure drag is decreased. The recirculation length is changed by about 10% through actuation (Henning, 2008).

## 5.5 A mean-field Galerkin model

In this section, a least-order model for the flow field is reviewed. The form of the dynamic system and simplifying assumptions are discussed in § 5.5.1. The identification of the model coefficients is explained in § 5.5.2 and the implementation of actuation –for the current configuration– in § 5.5.3.

### 5.5.1 Amplitude model

Based on the phenomenology of the natural and the periodically forced flow behind the D-shaped bluff body, see § 5.4, a least-order model of the flow field should at minimum include the oscillatory fluctuations at the natural and actuation frequency, and the effected base flow changes. Therefore, the flow is partitioned in a steady base flow  $\mathbf{u}_0$ , two oscillatory modes  $\{\mathbf{u}_1, \mathbf{u}_2\}$  resolving natural shedding at

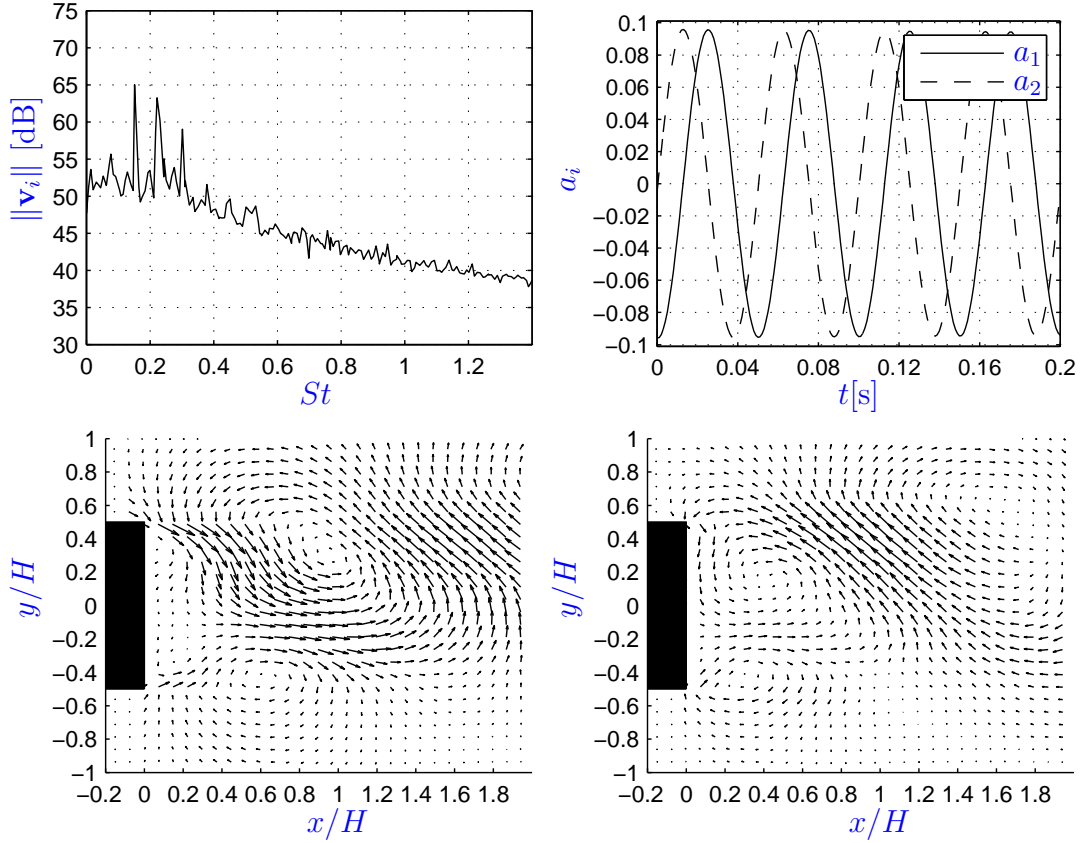


Figure 5.6: A spectral analysis of an actuated velocity field with  $St^a = 0.15$  at  $Re = 46\,000$ . The actuator amplitude of the loudspeaker is set to 5 V. Top, left: the magnitudes of the DMD modes as a function of their nondimensional frequency; right: the temporal amplitudes of the first DMD mode corresponding to  $St = 0.15$ . The bottom row shows the DMD mode. Left: the real part of the first mode, and right the imaginary part.

frequency  $\tilde{\omega}^n$ , two oscillatory modes  $\{\mathbf{u}_3, \mathbf{u}_4\}$  for the actuated state at frequency  $\tilde{\omega}^a$  and two shift modes  $\{\mathbf{u}_5, \mathbf{u}_6\}$  describing mean-field deformations due to both frequencies:

$$\mathbf{u}(\mathbf{x}, t) = \mathbf{u}_0(\mathbf{x}) + \underbrace{\sum_{i=1}^2 a_i(t) \mathbf{u}_i(\mathbf{x})}_{\text{frequency } \tilde{\omega}^n} + \underbrace{\sum_{i=3}^4 a_i(t) \mathbf{u}_i(\mathbf{x})}_{\text{frequency } \tilde{\omega}^a} + \underbrace{\sum_{i=5}^6 a_i(t) \mathbf{u}_i(\mathbf{x})}_{\text{base-flow changes}}. \quad (5.1)$$

The oscillatory motion of the flow at its natural and actuated frequency can for instance be described by DMD modes, as shown in figures 5.3 and 5.6. The two shift modes describing base flow changes cannot be computed from experimental data. A surrogate quantity can be defined as the difference of the natural and actuated time-averaged flow. Here, the focus is not on finding the velocity field decomposition, but on simplifying assumptions for the dynamic system that governs the evolution of the temporal amplitudes  $a_i$ . In particular, we are interested in the amplitudes of the natural and actuated fluctuation:  $A^n = \sqrt{a_1^2 + a_2^2}$  and  $A^a = \sqrt{a_3^2 + a_4^2}$ .

Based on the described phenomenology, we use the generalized mean-field model in polar form (2.100), although in a slightly different form (compare with the simplifications in § 4.5.1):

$$\frac{dA^n}{dt} = (\sigma^n - \beta^n a_5 - \delta^n a_6) A^n, \quad (5.2a)$$

$$\frac{dA^a}{dt} = \sigma^a A^a + gB, \quad (5.2b)$$

$$\frac{da_5}{dt} = \rho ((A^n)^2 - a_5), \quad (5.2c)$$

$$\frac{da_6}{dt} = \eta ((A^a)^2 - a_6). \quad (5.2d)$$

Here  $g$  is the coefficient corresponding to the time-varying actuation input  $B$ . Note from comparison with (4.9) that the last two equations for the base flow are not slaved to the fluctuation amplitudes. The coefficients  $\rho$  and  $\eta$  are chosen large compared to the growth rates  $\sigma^n$  and  $\sigma^a$ . In essence this amounts to slaving the the last two equations to the first two (i.e. set  $\dot{a}_5 = \dot{a}_6 \equiv 0$  and solve for  $a_5$  and  $a_6$ ). Hence the evolution equations (5.2c) and (5.2d) are merely dummy equations. The reason for this decoupling is convenient controller design based on the standard quadratic form of a Galerkin system.

### 5.5.2 Conditions for the model coefficients

The parameters of the amplitude model (5.2) are identified by calibration with experimental data. The amplitudes of the fluctuations at the natural and actuated attractors can be identified by spectral analysis of the PIV snapshots or the pressure readings. The absolute values of  $A^n$  and  $A^a$  are not considered important here, but their relative values with respect to each other.

Consider three reference trajectories: a natural attractor and an actuated attractor, and also the transient that connects the two. The following conditions must be satisfied on the natural attractor (unforced flow): the amplitudes are constant, i.e.  $A^n = A^{n,n}$ ,  $A^a = A^{a,n} = 0$ ,  $a_5^n = a_5^n$ ,  $a_6 = a_6^n$ . Consequently, their time derivatives vanish identically:

$$0 = \sigma^n + \beta^n a_5^n + \delta^n a_6^n, \quad (5.3a)$$

$$0 = (A^{n,n})^2 - a_5^n, \quad (5.3b)$$

$$0 = (A^{a,n})^2 - a_6^n. \quad (5.3c)$$

Similarly, on the actuated attractor (forced locked-in flow);  $A^n = A^{n,a}$ ,  $A^a = A^{a,a}$ ,  $a_5 = a_5^a$ ,  $a_6 = a_6^a$  and:

$$0 = \sigma^n + \beta^n a_5^a + \delta^n a_6^a, \quad (5.4a)$$

$$0 = \sigma^a A^{a,a} + gB, \quad (5.4b)$$

$$0 = (A^{n,a})^2 - a_5^a, \quad (5.4c)$$

$$0 = (A^{a,a})^2 - a_6^a. \quad (5.4d)$$

The coefficient  $\sigma^a$  is negative, since the second oscillator only exists under actuation. The growth rates  $\sigma^n$  and  $\sigma^a$  are determined by the transient times of the system:

$$\frac{1}{T_1} = \sigma^n, \quad \frac{1}{T_2} = -\sigma^a. \quad (5.5)$$

The first transient time  $T_1$  is inferred from the transient of a locked-in actuated flow to a natural flow, i.e. actuation is turned off. The second time constant is determined from the transient of the natural to a locked-in actuated flow, i.e. actuation is turned on.

The parameters  $\rho$  and  $\eta$  are arbitrarily set to:

$$\rho = 10 \sigma^n, \quad \eta = -10 \sigma^a. \quad (5.6)$$

### 5.5.3 Implementation of actuation

The conditions for the model coefficients in the previous section are appropriate for a trajectory that describes the natural flow, a locked-in actuated flow and transients between both states. It is, however, not clear how the actuation input  $B = B(t)$  of the model is related to the physical actuator amplitude, i.e. the voltage input to the loudspeaker  $u$  or the effectuated momentum coefficient  $c_\mu$ . Here, an empirical relationship is established by connecting  $B$  to the spatially averaged pressure coefficient  $\langle c_p(t) \rangle$ .

If the flow is periodically forced at its optimal frequency of  $St^a \approx 0.15$ , the base pressure coefficient steadily increases with actuation power until it saturates at a loudspeaker voltage of about 3.5 V or an effectuated  $c_\mu \approx 0.006$  ( $Re = 46\,000$ ). The relation between the nondimensional excitation coefficient  $c_\mu$  and the amplitude voltage input  $\hat{u}$  to the loudspeaker-actuator is shown in figure 5.7.

In the left plot of figure 5.8 a typical example is shown of a stepwise increment of the actuation amplitude. The corresponding response of the base pressure coefficient  $\langle c_p \rangle$  is shown in the right plot of the same figure, where the white lines indicate the time-averaged attractor values. These attractor averages define a static relationship between  $\hat{u}$  and  $\langle c_p \rangle$ , see figure 5.9. The mapping from the actuation amplitude  $\hat{u}$  to the time-averaged attractor values of the base pressure coefficient is approximated by a tanh function

$$\langle c_p \rangle = a \tanh(b(\hat{u} - c)) + d, \quad (5.7)$$

where  $\{a, b, c, d\}$  are constants that follow from fitting the measurements. Alternatively, the static map can be stored as a look-up table. The static relationship between  $\hat{u}$  and  $\langle c_p \rangle$  can be related to the amplitude model once the measurement equation is defined. Let the measurement equation be defined as a linear combination of the energy levels of both oscillators

$$y = \langle c_p \rangle = c_0 + c_1 (A^n)^2 + c_2 (A^a)^2. \quad (5.8)$$

The relation (5.8) together with (5.4) yields an expression for the actuation input  $B$  to the model (5.2):

$$B = \tilde{c} \sqrt{\langle c_p \rangle - \langle c_{p0} \rangle}, \quad (5.9)$$

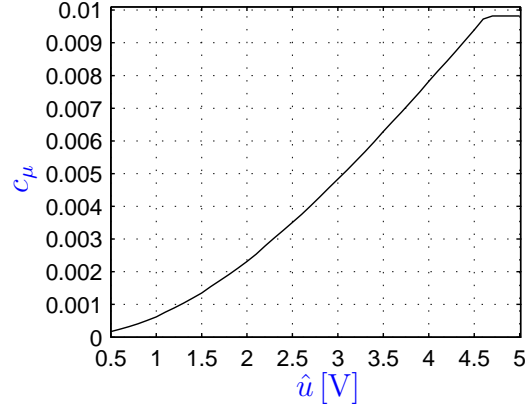


Figure 5.7: The relation between the loudspeaker voltage  $\hat{u}$  and the momentum coefficient  $c_\mu$ ;  $St^a = 0.15$ .

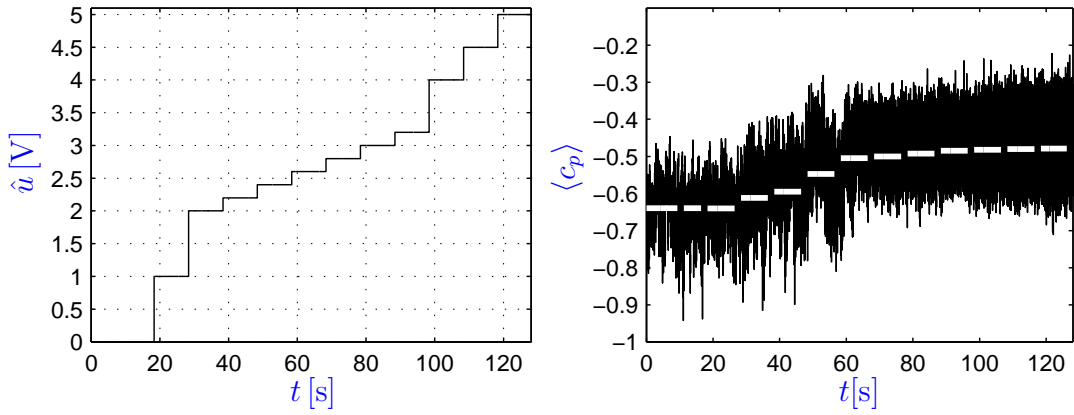


Figure 5.8: Stepwise increments of the actuation amplitude at  $Re = 46\,000$ : Left: loudspeaker voltage  $\hat{u}$ , right: base pressure coefficient  $\langle c_p(t) \rangle$  and its time-averaged attractor values (white lines).

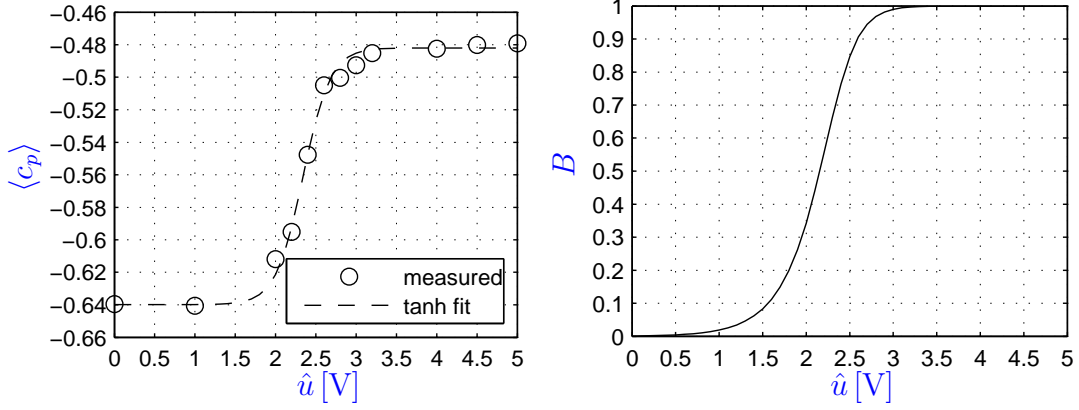


Figure 5.9: Left: the static mapping of the loudspeaker amplitude  $\hat{u}$  to  $\langle c_p(t) \rangle$ ,  $Re = 46\,000$ ,  $St^a = 0.15$ ; right: the implied static relationship between  $\hat{u}$  and the actuation amplitude to the model  $B$  (see (5.7) and (5.10)).

where  $\langle c_{p0} \rangle$  is the value of  $\langle c_p \rangle$  when  $A^a = 0$  and  $\tilde{c}$  is an arbitrary scaling constant. Combining this with (5.7), the input signal to the model  $B$  is related to input-voltage of the actuator  $\hat{u}$  as follows

$$B = \hat{B} \sqrt{a \tanh(b(\hat{u} - c)) + d - \langle c_{p0} \rangle}, \quad (5.10)$$

where  $\hat{B}$  is a scaling constant, such that for  $\hat{u} \rightarrow \infty$ ,  $B = 1$ . This relationship is shown in the right plot of figure 5.9.

## 5.6 Experimental results

The amplitude model, derived from the Galerkin mean-field model (see § 5.5), is used to describe the bluff body wake. The parameter identification of the model is described in § 5.6.1. In § 5.6.2 the calibrated model is employed for set-point tracking of the base pressure coefficient .

### 5.6.1 Model parameter identification

An open-loop reference experiment at  $Re = 46\,000$  is used to identify the parameters of the amplitude model (5.2), the static relationship (5.7) and the measurement equation (5.8). The model is calibrated using the base pressure data from

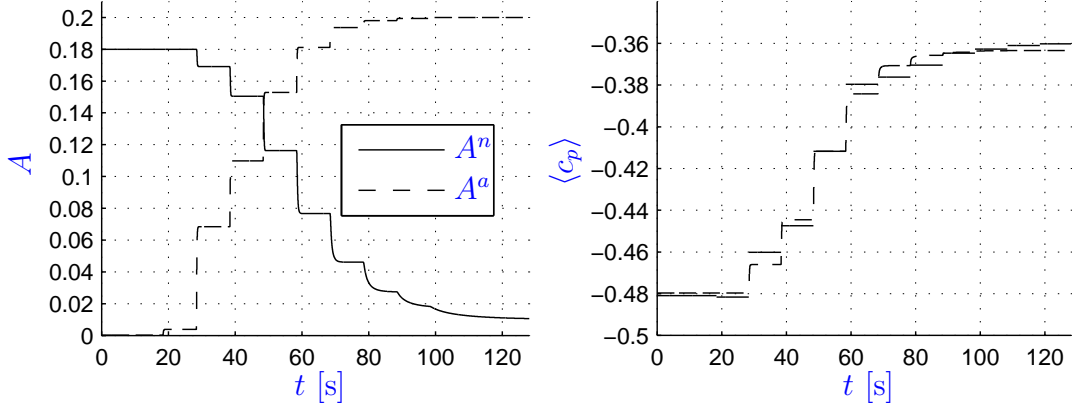


Figure 5.10: Left: the amplitudes  $A^n$  and  $A^a$  of the calibrated model;  $Re = 46\,000$ ,  $St^a = 0.15$ , right: the measured time-averaged base pressure coefficient (—) and the mean base pressure coefficients as predicted by the model (— —).

the sensors. The actuation amplitude is increased stepwise as shown in figure 5.8. The constraints: (5.3), (5.4) and (5.5) are applied to determine the model constants. The conditions at the actuated attractor are applied for the locked-in flow field, where the voltage of the actuator equals 5 V. It is assumed that  $B = 1$  when  $\hat{u} = 5$  V (compare with (5.10) and figure 5.9). After the calibration of the coefficients of the amplitude model, the coefficients for the static relationship (5.7) and the measurement equation (5.8) are determined.

The amplitudes  $A^n$  and  $A^a$  corresponding to the oscillatory fluctuations, obtained by integration of the amplitude model (5.2), are shown in the left plot of figure 5.10. The identified base pressure coefficient follows from the linear combination of the squared amplitudes as defined by (5.8). The comparison of the identified base pressure coefficient with the experimental data is shown in the right plot of figure 5.10.

### 5.6.2 Set-point tracking of base-pressure coefficient

The sliding mode controller, described in § 2.4.1, is implemented for set-point tracking of the time-averaged base pressure coefficient  $\langle c_p \rangle$ . The dynamic system is given by (5.2) and the measurement equation by (5.8). The control goal is the



## 5.6 Experimental results

same as the measured quantity  $y$  and is repeated for sake of convenience:

$$\langle c_p \rangle = c_0 + c_1 (A^n)^2 + c_2 (A^a)^2. \quad (5.11)$$

The corresponding control law for the model amplitude  $B$  is (compare with (2.106) and (2.104))

$$B_{sm} = B_{eq} - K \operatorname{sat} \left( \frac{s}{\psi} \right), \quad (5.12)$$

with the equivalent control law

$$B_{eq} = -\frac{c_1 (\sigma^n + \beta^n a_5 + \delta^n a_6) (A^n)^2}{c_2 A^a g} - \frac{\sigma^a A^a}{g}. \quad (5.13)$$

An extended Kalman filter (EKF) is used to estimate the oscillation amplitudes  $A^n$  and  $A^a$  from the base pressure coefficient.

The model coefficients are calibrated for a (fixed) Reynolds number of  $Re = 46\,000$  as described in the previous section. Figure 5.11 shows the tracking response of the closed-loop system after stepwise changes of the reference command  $\langle c_{p,ref} \rangle$  (the white line in the top right plot). The controlled system output  $\langle c_p \rangle$  follows the prescribed reference command, although there *appears* to be a bias, particularly during the second step that starts at  $t \approx 30$  s. There is, however, no severe bias in the signal: it is only a plotting related issue related to the amount of information.<sup>1</sup> The center right plot shows a comparison of the reference command and the time-averaged base pressure coefficient, where the time-average is taken over the part of the trajectory where the reference command is constant. This figure indeed shows that the controlled system output is in good agreement with the reference command. There is only a slight offset during the first control phase ( $t = 8.3 - 28.3$  s). The corresponding reduction of the (low-pass filtered) drag coefficient  $c_D$  is shown in the bottom right figure. The control input to the model  $B_{sm}$  and the excitation momentum coefficient  $c_\mu$  are shown in the left plots. The clipped control input is due to saturation of the base pressure coefficient at  $c_\mu = 0.009$ . The robustness of the sliding mode controller with respect to changing operating conditions is verified by varying the Reynolds

---

<sup>1</sup>Ten seconds of measurement time, with a sample rate of 1000 [Hz], implies 10 000 measurements contaminated with high-frequency noise.

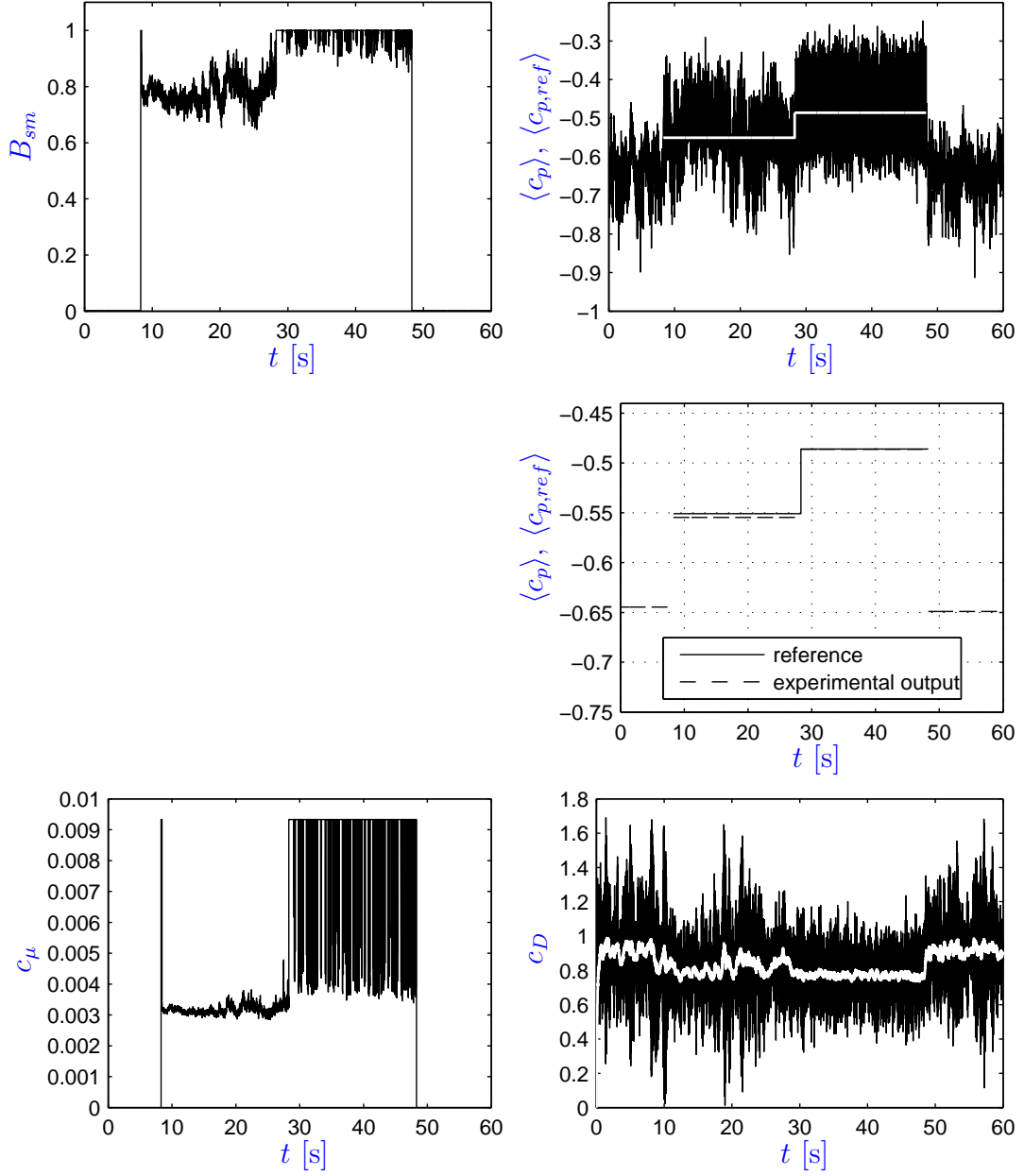


Figure 5.11: Reference tracking test of the sliding mode controller;  $Re = 46\,800$ ,  $St^a = 0.15$ . The controller starts at  $t = 8.3$  s. The reference and experimental base pressure coefficient (top right), the reference and time-averaged experimental base pressure coefficient (center right), the (low-pass filtered) drag coefficient (bottom right), the control input to the model  $B$  (top left), and the excitation momentum coefficient  $c_\mu$  (bottom left) are shown.

number from approximately 42 000 to 46 000 as shown in the bottom panel of figure 5.12, without changing the system derived controller parameters. Note that the model is calibrated for  $Re = 46\,000$ , which explains the offset for the natural flow during the first 8.3 seconds. After the change in Reynolds number at about  $t \approx 25$  s the controller requires more actuation power to keep the base pressure coefficient at the desired level (see the  $c_\mu$  plot). Again, there is a slight bias in the pressure coefficient (see center right plot), which is consistent with the previous reference tracking test in figure 5.11. The drag coefficient remains at about the same level throughout the Reynolds number variation and an acceptable tracking performance is obtained.

## 5.7 Conclusions

The present investigation focuses on drag reduction of the flow around a D-shaped bluff body in a wind tunnel experiment, where the Reynolds number is in the range: 42 000 to 46 000. Analysis of the velocity flow field shows that the natural wake is dominated by a vortex street at a dominant nondimensional frequency of about  $St^n \approx 0.15$ . The goal of active flow control is to reduce the adverse effect of this vortex street by introducing in phase vortices at about 65% of the natural frequency. This actuation mechanism introduces smaller synchronized vortices in the wake, which desynchronize the shear layer dynamics. The effectuated mean flow change leads to a drag reduction.

A generalized mean-field model with two dominant frequencies is postulated for this flow. This model describes coherent structures at the natural frequency, smaller structures that correspond to the actuated frequency, their mutual interaction and the mean-field component. The mean-field model is reduced to evolution equations for the amplitudes, since the control goal, the base pressure coefficient, solely is a function of the amplitudes (see also § 2.4). The amplitude model is used for design of a nonlinear sliding mode controller, with the purpose of set-point tracking of the base pressure coefficient. Reference tracking tests show that the sliding mode controller performs reasonably well and is also robust against slight changes in the Reynolds number.

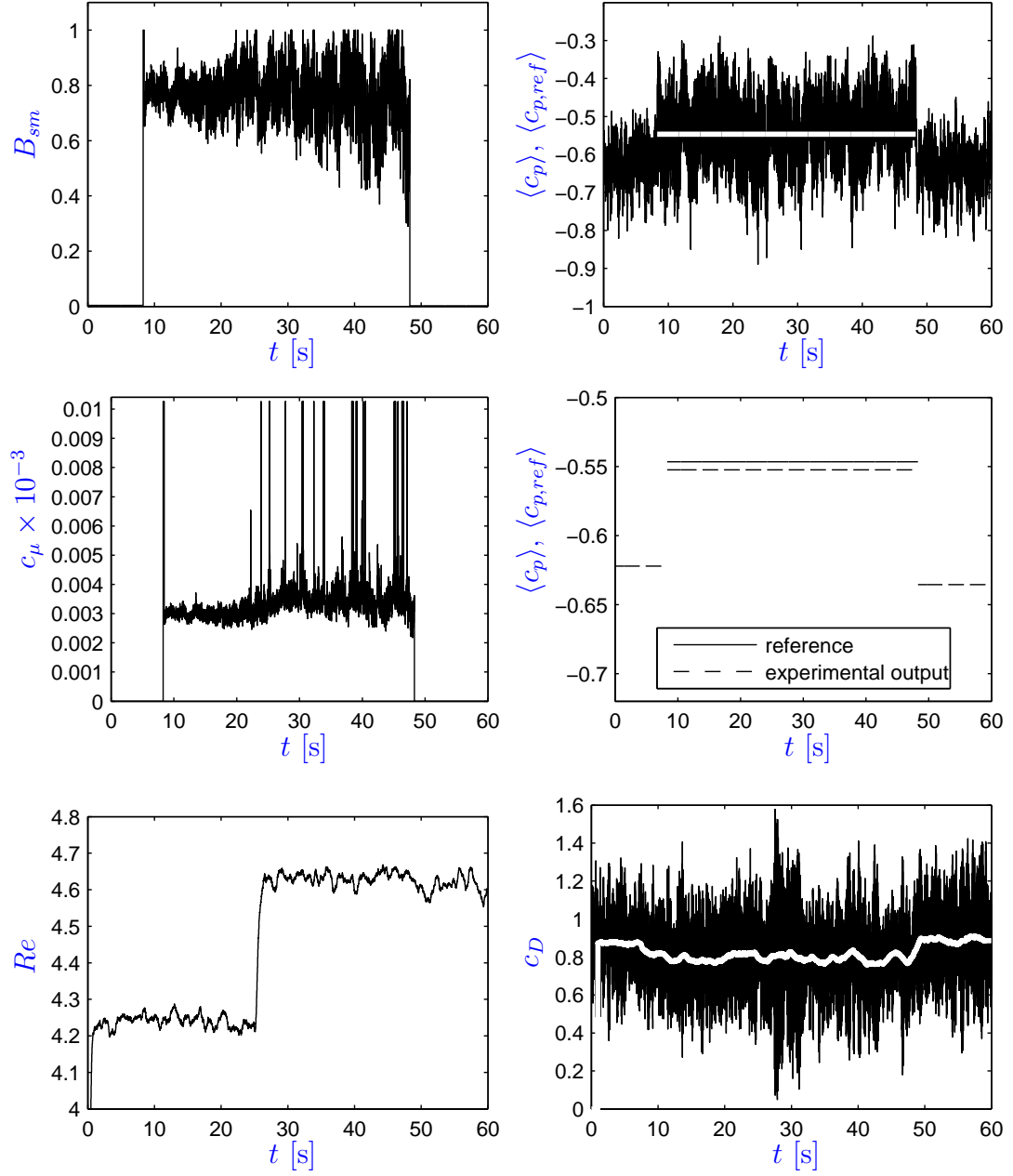


Figure 5.12: Reference tracking test of the sliding mode controller under changing operating conditions. The controller starts at  $t = 8.3$  s and is switched off at  $t = 48.3$  s. The Reynolds number varies from 42 000 to 46 000, while the base pressure coefficient is held constant at  $c_{p,ref} = -0.55$ .

## 5.7 Conclusions

---

The model approach described above allows the application of several non-linear control and state estimation methods and the reader is referred to [Aleksić \*et al.\* \(2010\)](#) for more control examples for a different type of bluff body.

# Chapter 6

## Conclusions

This thesis presented a mean-field based modelling framework for the purpose of understanding of key physical phenomena of separated fluid flows and subsequently for the development of nonlinear controllers based on these models. A (low-dimensional) POD basis of a natural flow does not include any transient information. The mean-field correction (change in mean flow) is added to this basis to make the model more robust, thus a mean-field model (see § 2.3.2) is obtained. The RANS equation hints at this correction (see § 2.1.3). Aerodynamic applications also exemplify the importance of the mean-field: the characteristics of the mean flow, e.g. the time-averaged shape of a wake, determine to a large extent the lift and drag.

In its simplest form the mean-field basis is given by a steady solution, two (dominant) oscillatory POD modes of the natural flow, and a shift mode which describes the mean-field correction. For this case, the shift mode is defined as the difference of the natural mean flow and the steady solution. These modes are used in an expansion for the velocity field. Substitution in the governing equations and Galerkin projection yields a dynamic system for the evolution of the temporal coefficients. This forms the complete reduced-order or mean-field model (see § 2.3.2). This very model forms a least-order representation for the laminar flow around a circular cylinder. In chapter 3 a parameterized POD approach is described for the cylinder wake flow to extend the dynamic range of the least-order mean-field model. The model structure is retained, and a collection of models is obtained for multiple operating conditions. Advantages

---

over standard POD models are manifest by improved ability to suppress vortex shedding. The parameterized POD model is also used to optimize sensor locations over the entire range (of available models). A SISO controller is implemented that uses an optimal sensor position, a dynamic observer and a pPOD based look-up table for suppression of the cylinder wake. Due to intrinsic instabilities it is difficult to fully stabilize the wake using SISO control with interpolated models.

The generalized mean-field model (see § 2.3.3) contains three additional modes in its basis compared to the mean-field model above. It is assumed that periodic actuation leads to a second oscillator in the flow field, that reduces the dominant instability at the natural frequency. This ‘actuated’ oscillator is also accompanied by a shift mode, representing mean-field variations due to the actuated fluctuations. As a consequence, the low-dimensional basis now contains: two shift modes, two mode pairs, corresponding to a ‘natural’ and ‘actuated’ oscillator and the steady solution. This model indeed provides a least order representation for the flow around a high-lift configuration in chapter 4. The high-frequency forcing effectuates changes in the flow by indirect interaction with the natural oscillator via the varying mean flow. The mechanism is phase-independent and hence explains why open-loop forcing can work. The proposed model captures URANS simulation data of the high-lift configuration surprisingly well considering the very low order. Model predictions include the lift coefficient which is in good agreement with the original data. As can be expected, predictions by this least-order model erode during fast transients, and a more accurate representation requires higher-order models. A main advantage of the analytical model is the possibility of a simple and robust calibration of a given data set. It was shown how a sliding mode controller can be used for improvement of open-loop control by closely tracking a prescribed lift coefficient.

The flow around the D-shaped bluff body in chapter 5 is characterized by large vortices in the wake, which lead to a relatively high (pressure) drag. These adverse effects of large coherent structures can be successfully reduced by periodic actuation at about 65% of the natural shedding frequency. This phenomenology motivates the application of a (simplified) mean-field Galerkin model for flow control. The goal in this experimental study is set-point tracking of the base pressure coefficient. The model is tuned in a configuration-specific manner and

---

the model coefficients are identified by calibration from pressure measurements. Subsequently, the tuned model is used for design of a nonlinear sliding mode controller. Reference tracking tests show that the sliding mode controller performs reasonably well and is also robust against slight changes in the Reynolds number.



# Appendix A

## Proper Orthogonal Decomposition

### A.1 POD in the spatial domain

In this section, the derivation of the POD is summarized. First the definitions introduced in §2.2.1 are recapitulated. The velocity field on the spatial domain  $\Omega$  is formally embedded in a mathematical space. Let  $H$  be a Hilbert space with the following inner product between two vector fields  $\mathbf{f}$ ,  $\mathbf{g}$ ,

$$(\mathbf{f}, \mathbf{g})_{\Omega} = \int_{\Omega} \mathbf{f} \cdot \mathbf{g} \, d\mathbf{x}, \quad (\text{A.1})$$

and the induced norm

$$\|\mathbf{f}\| = \sqrt{(\mathbf{f}, \mathbf{f})}. \quad (\text{A.2})$$

Let  $\mathbf{v} = \{\mathbf{v}_j \in H \mid j = 1, \dots, N\}$  be an orthonormal basis for a subspace  $S \subset H$ . Then the orthogonal projection of  $\mathbf{f} \in H$  onto  $S$  is given by

$$P_S \mathbf{f} = \sum_{i=1}^N (\mathbf{f}, \mathbf{v}_i)_{\Omega} \mathbf{v}_i. \quad (\text{A.3})$$

The time-averaging operator of a quantity  $a = a(t)$  is denoted by  $\bar{a}$  and can be approximated by a suitable quadrature rule:

$$\bar{a} = \sum_{i=1}^M w_k a(t_k), \quad (\text{A.4})$$

where  $w_k$  are the quadrature weights such that  $\sum_{k=1}^M w_k = 1$ .

The optimality condition for the POD is: given an ensemble of  $M$  snapshots<sup>1</sup>  $\mathbf{u} = \{\mathbf{u}(\mathbf{x}, t_j) \in H \mid j = 1, \dots, M\}$ , find a subspace  $S$  of fixed dimension  $N < M$  that minimizes the total error

$$\arg \min_{\{\mathbf{v}_i\} \in S} \overline{\|\mathbf{u} - P_S \mathbf{u}\|^2}. \quad (\text{A.5})$$

Using the Pythagorean theorem, it follows that  $\|\mathbf{u} - P_S \mathbf{u}\|^2 = \|\mathbf{u}\|^2 - \|P_S \mathbf{u}\|^2$ , since  $P_S$  is an orthogonal projection. Thus the optimality condition can also be formulated as

$$\arg \max_{\{\mathbf{v}_i\} \in S} \sum_{i=1}^N \overline{(\mathbf{u}, \mathbf{v}_i)_\Omega^2}. \quad (\text{A.6})$$

The first POD mode (or function)  $\mathbf{v}_1$  is the argument for which (A.6) is maximized when  $N = 1$

$$\mathbf{v}_1 = \arg \max_{\mathbf{v}_1 \in S} \overline{(\mathbf{u}, \mathbf{v}_1)_\Omega^2}, \quad (\text{A.7})$$

or with the constraint that  $\|\mathbf{v}_1\| = 1$ ,

$$\mathbf{v}_1 = \arg \max_{\mathbf{v}_1 \in S} \frac{\overline{(\mathbf{u}, \mathbf{v}_1)_\Omega^2}}{\|\mathbf{v}_1\|^2}. \quad (\text{A.8})$$

This problem can be solved by means of a calculus of variations. To this end, the Lagrangian  $J(\lambda_1, \mathbf{v}_1)$  with Lagrange multiplier  $\lambda_1$  is introduced

$$J(\lambda_1, \mathbf{v}_1) = \overline{|(\mathbf{u}, \mathbf{v}_1)_\Omega|^2} - \lambda_1(\|\mathbf{v}_1\|^2 - 1). \quad (\text{A.9})$$

Now define an operator  $C : H \rightarrow H$

$$C(\mathbf{v}) = \overline{(\mathbf{u}, \mathbf{v})_\Omega} \mathbf{u}. \quad (\text{A.10})$$

---

<sup>1</sup>The prime indicating a fluctuating field, as in (2.14), is suppressed in the following.

Then the extremum of (A.9) is given by (Astrid, 2004)

$$C(\mathbf{v}_1) = \lambda_1 \mathbf{v}_1. \quad (\text{A.11})$$

The second POD basis function must be orthogonal to the first one, hence the second Lagrangian is

$$J(\mu, \lambda_2, \mathbf{v}_2) = (\mathbf{v}_2, C(\mathbf{v}_2))_\Omega - \lambda_2 [(\mathbf{v}_2, \mathbf{v}_2)_\Omega - 1] - \mu(\mathbf{v}_1, \mathbf{v}_2)_\Omega. \quad (\text{A.12})$$

Since the operator  $C$  is self-adjoint it follows that all its eigenfunctions are orthogonal and the eigenvalues nonnegative,  $\lambda_i \geq 0$ . The orthogonality implies that the last term of the Lagrangian equals zero, i.e.  $(\mathbf{v}_1, \mathbf{v}_2)_\Omega = 0$ . Thus all POD modes  $\mathbf{u}_i(\mathbf{x}) = \mathbf{v}_i(\mathbf{x})$  are defined as solutions of the eigenproblem

$$\overline{(\mathbf{u}, \mathbf{u}_i)}_\Omega = \lambda_i \mathbf{u}_i. \quad (\text{A.13})$$

Note that  $\mathbf{u} = \mathbf{u}(\mathbf{x}, t)$  denotes the snapshot ensemble and  $\mathbf{u}_i = \mathbf{u}_i(\mathbf{x})$  the (spatially dependent) POD basis function on the domain  $\Omega$ . The eigenproblem can be rewritten as

$$\overline{(\mathbf{u}(\mathbf{y}, t), \mathbf{u}_i(\mathbf{y}))}_\Omega \mathbf{u}(\mathbf{x}, t) = \lambda_i \mathbf{u}_i(\mathbf{x}) \quad (\text{A.14})$$

Using the specific definition of the inner product given by (A.1), the POD modes are defined as the eigenfunctions of the Fredholm equation

$$\int_\Omega \mathbf{R}(\mathbf{x}, \mathbf{y}) \mathbf{u}_i(\mathbf{y}) d\mathbf{y} = \lambda_i \mathbf{u}_i(\mathbf{x}). \quad (\text{A.15})$$

Here,  $\mathbf{R}(\mathbf{x}, \mathbf{y})$  is the two-point autocorrelation tensor for the flow field, defined by

$$\mathbf{R}(\mathbf{x}, \mathbf{y}) = \overline{\mathbf{u}(\mathbf{x}, t) \otimes \mathbf{u}(\mathbf{y}, t)}, \quad (\text{A.16})$$

or in index notation

$$R_{\alpha\beta} = \overline{u_\alpha(\mathbf{x}, t) u_\beta(\mathbf{y}, t)}, \quad (\text{A.17})$$

where the greek symbols refer to the velocity components, i.e. in three dimensions  $\mathbf{u} = [u_1, u_2, u_3]$ . The modes are ordered with respect to the decreasing real non-negative eigenvalues  $\lambda_1 \geq \lambda_2 \geq \lambda_3 \geq \dots \geq 0$ . Note that zero eigenvalues are not

considered since they do not contribute to the velocity. Using the orthonormality of the modes, the time-dependent amplitudes follow from the projection

$$a_i(t) = (\mathbf{u}(\mathbf{x}, t), \mathbf{u}_i(\mathbf{x}))_\Omega. \quad (\text{A.18})$$

In summary, the velocity field is decomposed as

$$\mathbf{u}(\mathbf{x}, t) = \sum_{i=1}^M a_i(t) \mathbf{u}_i(\mathbf{x}), \quad (\text{A.19})$$

where  $\{\mathbf{u}_i\}_{i=1}^M \subset \mathcal{L}_2(\Omega)$  is the POD basis and time dependency is described by the amplitudes  $a_i$ .

Important properties of the POD are highlighted in the following:

- (i) The POD modes are orthonormal

$$(\mathbf{u}_i, \mathbf{u}_j)_\Omega = \delta_{ij}, \quad (\text{A.20})$$

- (ii) The autocorrelation function can be expanded using the POD modes

$$\mathbf{R}(\mathbf{x}, \mathbf{y}) = \sum_{i=1}^M \lambda_i \mathbf{u}_i(\mathbf{x}) \otimes \mathbf{u}_i(\mathbf{y}). \quad (\text{A.21})$$

This is the so called dyadic expansion. Note that the Reynolds stress is a special case of the autocorrelation tensor when  $\mathbf{x} = \mathbf{y}$ . The trace of the Reynolds tensor is twice the turbulent kinetic energy (compare (2.19))

$$q(\mathbf{x}) := \frac{1}{2} \overline{\mathbf{u}'(\mathbf{x}, t) \cdot \mathbf{u}'(\mathbf{x}, t)} = \frac{1}{2} \sum_{\alpha=1}^3 R_{\alpha\alpha}(\mathbf{x}, \mathbf{x}).$$

- (iii) The first and second statistical moments of the temporal coefficients are

$$\overline{a_i} = 0, \quad (\text{A.22a})$$

$$\overline{a_i a_j} = \lambda_i \delta_{ij}. \quad (\text{A.22b})$$

The second statistical moment shows that the modal amplitudes are orthogonal in time (no summation implied).

- (iv) The eigenvalue  $\lambda_i$  in (A.15) represents the average kinetic energy captured by POD mode  $u_i$ . The turbulent kinetic energy in the complete domain is

$$\mathcal{K}_\Omega = \frac{1}{2} \overline{(\mathbf{u}', \mathbf{u}')}_\Omega = \frac{1}{2} \sum_{i=1}^M \lambda_i. \quad (\text{A.23})$$

This equation follows from the bi-orthogonality property of the POD, i.e. (A.20) and (A.22b).

- (v) Finally, it is stipulated that (A.13) is the general definition of a POD mode, where the inner product and the temporal average operator can be freely chosen (see e.g. Rowley *et al.*, 2003; Schlegel *et al.*, 2010).

## A.2 POD in the temporal domain

The decomposition (A.19) can be read as an expansion with spatial modes  $\mathbf{u}_i$  and temporal coefficients  $a_i$  or alternatively as an expansion with temporal modes  $a_i$  and spatial coefficients  $\mathbf{u}_i$ . This symmetry implies that time and space can be interchanged. Integration over space is replaced by integration over the time domain by the quadrature rule (A.4). Thus the orthonormality in space and time, respectively expressed by (A.20) and (A.22b) is analogue.

Similarly the spatial correlation (A.17) is exchanged for the temporal correlation function

$$C(t_i, t_j) = (\mathbf{u}(\mathbf{x}, t_i), \mathbf{u}(\mathbf{x}, t_j))_\Omega. \quad (\text{A.24})$$

The eigenproblem for the eigenfunction  $a_k$  with eigenvalue  $\mu_k$  is

$$\sum_{j=1}^M w_j C(t_i, t_j) a_k(t_j) = \mu_k a_k(t_i). \quad (\text{A.25})$$

As in Appendix A.1, the modes are ordered with respect to the decreasing real nonnegative eigenvalues  $\mu_1 \geq \mu_2 \geq \mu_3 \geq \dots > 0$ . These eigenvalues are identical to the ones obtained from the decomposition in the spatial domain, i.e.  $\mu_i = \lambda_i$ .

The self-adjointness of the temporal autocorrelation function implies the orthogonality of the temporal coefficients. The coefficients are scaled such that

$$\overline{a_i a_j} = \lambda_i \delta_{ij}. \quad (\text{A.26})$$

Now the exact same scaling as before is obtained (compare with (A.22b)). Using this scaling, the POD modes are calculated by the projection

$$\mathbf{u}_i(\mathbf{x}) = \frac{1}{\lambda_i} \overline{a_i(t) \mathbf{u}(\mathbf{x}, t)}. \quad (\text{A.27})$$

The autocorrelation function can be expanded, in complete analogy to (A.21), as follows

$$C(t_i, t_j) = \sum_{k=1}^M a_k(t_i) a_k(t_j). \quad (\text{A.28})$$

In summary, the same information can be obtained in the time domain as in the spatial domain. Note that the POD modes computed from (A.25), (A.24) and (A.27) are in general different from the ones obtained by application of (2.28) and (2.27). The latter are obtained from an equivalent formulation in the spatial domain, whereas the former are directly derived from the formulation in the temporal domain.

### A.3 POD and its connection to SVD

In §2.2.1 the connection of the SVD to the POD was shown. This connection can also be shown by direct application of the general definition (A.13) as is done here.

Assume that a continuous vector field  $\mathbf{u} = \mathbf{u}(\mathbf{x}, t)$  on a domain  $\Omega$  is spatially discretized onto  $K$  gridpoints. Let an ensemble of  $M$  snapshots be given of the discretized field. The data is collected in a snapshot matrix

$$\mathbf{X} = \begin{bmatrix} \mathbf{u}^{(1)}(\mathbf{x}_1) & \mathbf{u}^{(2)}(\mathbf{x}_1) & \dots & \mathbf{u}^{(M)}(\mathbf{x}_1) \\ \mathbf{u}^{(1)}(\mathbf{x}_2) & \mathbf{u}^{(2)}(\mathbf{x}_2) & \dots & \mathbf{u}^{(M)}(\mathbf{x}_2) \\ \vdots & \vdots & & \vdots \\ \mathbf{u}^{(1)}(\mathbf{x}_K) & \mathbf{u}^{(2)}(\mathbf{x}_K) & \dots & \mathbf{u}^{(M)}(\mathbf{x}_K) \end{bmatrix} = [\mathbf{u}^{(1)} \quad \mathbf{u}^{(2)} \quad \dots \quad \mathbf{u}^{(M)}], \quad (\text{A.29})$$

where  $\mathbf{u}^{(i)}(\mathbf{x}_j)$  is the value of the vector field at gridpoint  $\mathbf{x} = \mathbf{x}_j$  and time  $t = t_i$ . The row-direction of  $\mathbf{X}$  corresponds with the discrete spatial domain and the

---

### A.3 POD and its connection to SVD

---

columns contain the snapshots. The spatial correlation matrix can be build by after-multiplying with the transposed snapshot matrix, i.e.

$$\mathbf{C} = \mathbf{X}\mathbf{X}^T. \quad (\text{A.30})$$

This result is now connected to the definition of a POD mode. Recall the definition given by (A.13)

$$\overline{(\mathbf{u}, \mathbf{u}_i)_\Omega} \mathbf{u} = \lambda_i \mathbf{u}_i.$$

The time average is defined as the ensemble average and the spatial inner product is simply the Euclidean product (column  $\times$  row vector). Using these definitions,

$$\overline{(\mathbf{u}, \mathbf{u}_i)_\Omega} \mathbf{u} = \sum_{j=1}^M \frac{1}{M} \left( \mathbf{u}^{(j)} [\mathbf{u}^{(j)}]^T \right) \mathbf{u}_i = \frac{1}{M} (\mathbf{X}\mathbf{X}^T) \mathbf{u}_i = \frac{1}{M} \mathbf{C} \mathbf{u}_i.$$

The POD modes are found as solutions of the eigenproblem

$$\frac{1}{M} (\mathbf{X}\mathbf{X}^T) \mathbf{u}_i = \lambda \mathbf{u}_i. \quad (\text{A.31})$$

The singular value decomposition (Strang, 1988) of a matrix  $\mathbf{A} \in \mathbb{R}^{K \times M}$  with  $\text{rank}(\mathbf{A}) = r$  is a decomposition<sup>1</sup>

$$\mathbf{A} = \frac{1}{\sqrt{M}} \mathbf{U} \mathbf{\Sigma} \mathbf{V}^T, \quad (\text{A.32})$$

with unitary  $\mathbf{U} \in \mathbb{R}^{K \times K}$ , unitary  $\mathbf{V} \in \mathbb{R}^{M \times M}$

$$\mathbf{U}\mathbf{U}^T = \mathbf{I}_K, \quad \mathbf{U}^T\mathbf{U} = \mathbf{I}_K, \quad (\text{A.33})$$

$$\mathbf{V}\mathbf{V}^T = \mathbf{I}_M, \quad \mathbf{V}^T\mathbf{V} = \mathbf{I}_M, \quad (\text{A.34})$$

and diagonal matrix  $\mathbf{\Sigma}$  with  $r$  positive diagonal entries  $\sigma_1 \geq \sigma_2 \geq \dots \geq \sigma_r > 0$

$$\mathbf{\Sigma} = \begin{bmatrix} \sigma_1 & 0 & 0 & 0 & \dots & 0 \\ 0 & \ddots & 0 & 0 & \dots & 0 \\ 0 & \dots & \sigma_r & 0 & \dots & 0 \\ 0 & \dots & 0 & 0 & \dots & 0 \\ \vdots & & \vdots & \vdots & & \vdots \\ 0 & \dots & 0 & 0 & \dots & 0 \end{bmatrix}. \quad (\text{A.35})$$

---

<sup>1</sup>The factor  $1/\sqrt{M}$  is introduced for notational consistency.

### A.3 POD and its connection to SVD

---

The diagonal entries are called singular values. The connection to POD follows simply by decoupling  $\mathbf{A}\mathbf{A}^T$

$$\frac{1}{M} (\mathbf{A}\mathbf{A}^T) \mathbf{U} = \frac{1}{M} \mathbf{U}\mathbf{\Sigma}^2. \quad (\text{A.36})$$

Consider the case with  $\mathbf{A} = \mathbf{X}$ , comparing (A.31) with (A.36), it is clear that the columns of  $\mathbf{U}$  contain the POD modes. The eigenvalues of the POD problem are equal to the scaled squared singular values of the snapshot matrix, i.e.  $\lambda_i = \sigma_i^2/M$ . If the snapshot matrix is transposed, similar reasoning applies; in this case not the spatial POD modes are found, but the temporal coefficients. This is the discrete equivalent of the method of snapshots (see § 2.2.1)

$$\frac{1}{M} (\mathbf{A}^T \mathbf{A}) \mathbf{V} = \frac{1}{M} \mathbf{V}\mathbf{\Sigma}^2. \quad (\text{A.37})$$

Again, let  $\mathbf{A} = \mathbf{X}$ . Then, the columns of  $\mathbf{V}$  contain the temporal coefficients for the POD modes. As before, the scaled squared singular values correspond to the eigenvalues in (A.31).



# Appendix B

## Window filters and structure of the Galerkin system

### B.1 Window filters

Here, a general approach to split up the Navier-Stokes equations into separate equations for each flow contribution in partition (2.89) is described. In the following observation, the standard notation of  $\mathcal{L}_2$  is used. Specifically, given (an implicitly known) Hilbert space  $H$ , the space  $\mathcal{L}_2$  is the linear space of measurable functions  $f : \mathbb{R} \mapsto H$  with the property that  $f|_{[a,b]} \in \mathcal{L}_2[a,b]$  for all finite intervals,  $-\infty < a < b < \infty$ . For example, in the context of the incompressible Navier-Stokes solutions,  $H = \mathcal{L}_2(\Omega)$  is the divergence free, sufficiently smooth space of velocity fields with appropriate boundary conditions.

**Observation B.1.1** *Let  $f(t) \in \mathcal{L}_2$  satisfy assumption NSE 1:*

$$f(t) = f^B(t) + f^n(t) + f^a(t)$$

*where  $f^B$ ,  $f^n$  and  $f^a$  satisfy the counterparts of (2.91). Let  $T > 0$  be a set length of a time window. Then there exist kernels  $K^B(\tau)$ ,  $K^n(\tau)$ ,  $K^a(\tau) \in \mathcal{L}_2\left([-\frac{T}{2}, \frac{T}{2}]\right)$*

such that the following approximation is satisfied to an order  $O(\epsilon)$ :

$$f^B(t) = \int_{-\frac{T}{2}}^{\frac{T}{2}} K^B(\tau) f(t + \tau) d\tau, \quad (\text{B.1a})$$

$$f^n(t) = \int_{-\frac{T}{2}}^{\frac{T}{2}} K^n(\tau) f(t + \tau) d\tau, \quad (\text{B.1b})$$

$$f^a(t) = \int_{-\frac{T}{2}}^{\frac{T}{2}} K^a(\tau) f(t + \tau) d\tau. \quad (\text{B.1c})$$

The significance of Observation B.1.1 in the present discussion is that the window filters in (B.1) commute with time differentiation; when applied to the velocity field  $\mathbf{u}(\mathbf{x}, t)$ , the same holds for spatial derivatives. Hence, this filter has one important property of the Reynolds average, see (2.4d).

**Proof B.1.1** Denote  $\Phi = \{\Phi_i(\tau)\}_{i=1}^5 = \{1, \cos(\omega_n \tau), \sin(\omega_n \tau), \cos(\omega_a \tau), \sin(\omega_a \tau)\}$ , and let  $\mathbf{A} : \Re^5 \mapsto \text{span}(\Phi) \subset \mathcal{L}_2 \left\{ \left[-\frac{T}{2}, \frac{T}{2}\right] \right\}$  be defined as

$$\mathbf{A} \mathbf{d} = \sum_{i=1}^5 d_i \Phi_i(\tau). \quad (\text{B.2})$$

Then, the adjoint  $\mathbf{A}^* : \text{span}(\Phi) \mapsto \Re^5$  is an integral operator and the orthogonal projection of  $\mathcal{L}_2 \left\{ \left[-\frac{T}{2}, \frac{T}{2}\right] \right\}$  onto  $\text{span}(\Phi)$  is  $\Pi = \mathbf{A} (\mathbf{A}^* \mathbf{A})^{-1} \mathbf{A}^*$ . In particular, the linear combination coefficients of the projection  $\Pi \zeta$  are given by integral functionals:

$$\mathbf{d} = (\mathbf{A}^* \mathbf{A})^{-1} \mathbf{A}^* \zeta \Leftrightarrow d_i = \int_{-\frac{T}{2}}^{\frac{T}{2}} K_i(\tau) \zeta(\tau) d\tau, \quad (\text{B.3})$$

where the kernels  $K_i$  are linear combinations of the base functions  $\Phi_i$ . In the simple case where  $T = T_n$  is the natural period and the two frequencies are harmonically related, this formulation reduces to a partial Fourier expansion and  $K_i$  are the standard normalized versions of the trigonometric functions.

Now let  $f(t)$  be a time function satisfying NSE 1. This means that over a window  $[t - \frac{T}{2}, t + \frac{T}{2}]$  the three components of the function  $\zeta(\tau) = f(t + \tau)$  can be approximated to an order  $O(\epsilon)$  in the form

$$\begin{aligned}
 f^B(t + \tau) &= f^B(t), \\
 f^n(t + \tau) &= \eta^n \cos(\omega_n \tau + \theta^n) \\
 &= \eta^n [\cos(\theta^n) \cos(\omega_n \tau) - \sin(\theta^n) \sin(\omega_n \tau)], \\
 f^a(t + \tau) &= \eta^a \cos(\omega_a \tau + \theta^a) \\
 &= \eta^a [\cos(\theta^a) \cos(\omega_a \tau) - \sin(\theta^a) \sin(\omega_a \tau)].
 \end{aligned} \tag{B.4}$$

Each of the functions on the right hand side of (B.4), as well as their sum, is a member of  $\text{span}(\Phi)$ . Thus,  $\zeta(\tau) = f(t + \tau) = \mathbf{A} \mathbf{d}$  can be approximated as in (B.2). The approximation is accurate up to an order  $O(\epsilon)$  (say, relative to the  $\mathcal{L}_2[-\frac{T}{2}, \frac{T}{2}]$  norm). The coefficients  $d_i$  are computed by integral filters, as in (B.3).

Since the three approximate expressions for  $f^B(t + \tau)$ ,  $f^n(t + \tau)$  and  $f^a(t + \tau)$  in (B.4) are all continuously differentiable in  $\tau$ , they can be evaluated at  $\tau = 0$ , leading to evaluation of the coefficients  $d_i$ ,  $i = 1, 2, 4$  as  $f^B(t) = d_1$ ,  $f^n(t) = \eta^n \cos(\theta^n) = d_2$  and  $f^a(t) = \eta^a \cos(\theta^a) = d_4$ . The proof is completed by comparing these expressions with the expressions from (B.3). Notice that the values of  $d_i$ ,  $i = 3, 5$ , are not needed to evaluate  $f^n(t + \tau)$  and  $f^a(t + \tau)$  at  $\tau = 0$ .

It is observed that the proof remains valid when the spanning set  $\Phi$  is enlarged to include a predetermined number of higher and mixed harmonics of the two base frequencies, that are deemed non-negligible in the flow under consideration. This is valid because while  $\Phi$  is implicitly assumed linearly independent, orthogonality of the base functions is not assumed. The significance of this observation is that the projection formulas in (B.1) can be made to filter out additional harmonics

due quadratic terms in the Navier-Stokes equations, as computed in the next section.

## B.2 Structure of the mean-field Galerkin model

Here, the structure of the Galerkin system is derived from equation (2.95), and the hypotheses made heretofore. These assumptions include NSE 1 – NSE 4, in the Navier-Stokes framework and their effect on the Galerkin system through Galerkin projection. Inaccuracies that result from the linearization (2.95c) are partially compensated for by the calibration of system parameters. This linearization leads to the linear dependence of  $\mathbf{a}^B$  on  $(A^n)^2 = \|\mathbf{a}^n\|^2$  and  $(A^a)^2 = \|\mathbf{a}^a\|^2$ , as stated in Observation B.2.1, below. The expression for  $\mathbf{a}^B$  without that assumption includes higher-order terms in  $(A^n)^2$  and  $(A^a)^2$ .

Equations (2.96) and (2.97) can be derived from (2.95a), (2.95b) and (2.95c) in a straight-forward manner by a lengthy calculation exploiting the phase-invariance assumption. Here, a more compact and insightful Hilbert-space consideration is chosen.

**Observation B.2.1** *Under the assumptions above, there exists a  $2 \times 2$  matrix  $A^B$  such that*

$$\mathbf{a}^B = A^B \begin{bmatrix} (A^n)^2 \\ (A^a)^2 \end{bmatrix} \quad (\text{B.5})$$

Note that  $\mathbf{a}^B = 0$  at  $A^a = A^n = 0$  since the steady Navier-Stokes solution serves as base flow.

**Proof B.2.1** *By NSE 1 the base flow satisfies time-independent boundary conditions, whence the mean-flow deformation  $\mathbf{u}^\Delta = \mathbf{u}^B - \mathbf{u}_s$  satisfies homogeneous boundary conditions. The linear mean-field deformation term in (2.93) reads*

$$\nabla \cdot (\mathbf{u}^s \otimes \mathbf{u}^\Delta + \mathbf{u}^\Delta \otimes \mathbf{u}^s) - \nu \Delta \mathbf{u}^\Delta. \quad (\text{B.6})$$

---

## B.2 Structure of the mean-field Galerkin model

This linear operator with homogeneous boundary conditions has the counterpart linear term  $\mathbf{L}(\mathbf{a}^B)$  in (2.95c). It is conjectured that the operator (B.6) and corresponding matrix  $\mathbf{L}$  are non-singular. Inverting that matrix, a linear expression for  $\mathbf{a}^B$  in terms of  $\mathbf{Q}(\mathbf{a}^n, \mathbf{a}^n) + \mathbf{Q}(\mathbf{a}^a, \mathbf{a}^a)$  is obtained.

The phase invariance hypothesis implies that the two quadratic terms  $\mathbf{Q}(\mathbf{a}^n, \mathbf{a}^n)$  and  $\mathbf{Q}(\mathbf{a}^a, \mathbf{a}^a)$  are both phase independent. They are therefore linearly determined by  $(A^n)^2$  and  $(A^a)^2$ , respectively.

**Observation B.2.2** Equation (2.95a) can be written in the form

$$\frac{d}{dt}\mathbf{a}^n = \begin{bmatrix} \tilde{\sigma}^n & -\tilde{\omega}^n \\ \tilde{\omega}^n & \tilde{\sigma}^n \end{bmatrix} \mathbf{a}^n \quad (\text{B.7})$$

where the state dependent coefficients are of the form

$$\begin{aligned} \tilde{\sigma}^n &= \sigma^n - \sigma^{n,n} (A^n)^2 - \sigma^{n,a} (A^a)^2 \\ \tilde{\omega}^n &= \omega^n + \omega^{n,n} (A^n)^2 + \omega^{n,a} (A^a)^2 \end{aligned} \quad (\text{B.8})$$

**Proof B.2.2** Clearly, the right-hand side of (2.95a) is linear in  $\mathbf{a}^n$ . It can therefore be re-written in the form

$$\frac{d}{dt}\mathbf{a}^n = F(\mathbf{a}^B) \mathbf{a}^n \quad (\text{B.9})$$

where the matrix  $F(\mathbf{a}^B)$  depends on  $\mathbf{a}^B$  in an affine manner. Invoking Observation B.2.1, the dependence on  $\mathbf{a}^B$  may be substituted by dependence on  $(A^n)^2$  and  $(A^a)^2$ . The fact that (B.9) is phase invariant means that the matrix  $F$  must commute with any rotation matrix. As such, it must be a scaled rotation matrix. That is,  $F$  must be of the form specified in (B.7). The affine dependence on the parameters implies (B.8).

**Observation B.2.3** Equation (2.95b) can be written in the form

$$\frac{d}{dt}\mathbf{a}^a = \begin{bmatrix} \tilde{\sigma}^a & -\tilde{\omega}^a \\ \tilde{\omega}^a & \tilde{\sigma}^a \end{bmatrix} \mathbf{a}^a + \begin{bmatrix} \kappa & -\lambda \\ \lambda & \kappa \end{bmatrix} \mathbf{b} \quad (\text{B.10})$$

where the state dependent coefficients are of the form

$$\begin{aligned} \tilde{\sigma}^a &= \sigma^a - \sigma^{a,n}(A^n)^2 - \sigma^{a,a}(A^a)^2 \\ \tilde{\omega}^a &= \omega^a + \omega^{a,n}(A^n)^2 + \omega^{a,a}(A^a)^2 \end{aligned} \quad (\text{B.11})$$

The proof of this observation is completely analogous to the proof of Observation B.2.2 and is left out. This completes the derivation of (2.96) - (2.97) from the three equations (2.95a), (2.95b), and (2.95c).

# References

- ALEKSIĆ, K., LUCHTENBURG, D.M., KING, R., NOACK, B.R. & PFEIFFER, J. (2010). Robust nonlinear control versus linear model predictive control of a bluff body wake. *AIAA Paper* 2010-4833.
- AMITAY, M. & GLEZER, A. (2002). Controlled transients of flow reattachment over stalled airfoils. *Int. J. Heat Transfer and Fluid Flow*, **23**, 690–699.
- ANNASWAMY, A., CHOI, J.J., SAHOO, D., , ALVI, F.S. & LOU, H. (2002). In *41st IEEE Conference on Decision and Control*, 3294–3299.
- ASTRID, P. (2004). *Reduction of Process Simulation Models: a proper orthogonal decomposition approach*. Ph.D. thesis, Technische Universiteit Eindhoven.
- AUBRY, N., HOLMES, P., LUMLEY, J. & STONE, E. (1988). The dynamics of coherent structures in the wall region of a turbulent boundary layer. *J. Fluid Mech.*, **192**, 115–173.
- BATCHELOR, G.K. (1967). *An introduction to fluid dynamics*. Cambridge University Press.
- BECKER, R., KING, R., PETZ, R. & NITSCHKE, W. (2007). Adaptive closed-loop separation control on a high-lift configuration using extremum seeking. *AIAA J.*, **45**, 1382–1392.
- BERGMANN, M., CORDIER, L. & BRANCHER, J.P. (2004). Optimal rotary control of the cylinder wake using pod reduced order model. *AIAA Paper* 2004-2323.

## REFERENCES

---

- CAMPHOUSE, R.C., MYATT, J.H., SCHMIT, R.F., , GLAUSER, M.N., AUSSEUR, J.M., ANDINO, M.Y. & WALLACE, R.D. (2008). A snapshot decomposition method for reduced order modeling and boundary feedback control. *AIAA Paper* 2008-4195.
- CHATTERJEE, A. (2000). An introduction to the proper orthogonal decomposition. *Curr. Sci.*, **7**, 808–817.
- CHOI, H., JEON, W.P. & KIM, J. (2008). Control of flow over a bluff body. *Annu. Rev. Fluid Mech.*, **40**, 113–139.
- COLLIS, S.S., JOSLIN, R.D., SEIFERT, A. & THEOFILIS, V. (2004). Issues in active flow control: theory, control, simulation, and experiment. *Prog. Aerosp. Sc.*, **40**, 237–289.
- CORDIER, L. & BERGMANN, M. (1999). Proper orthogonal decomposition: An overview. Tech. rep., Von Kármán Institute for Fluid Dynamics.
- COUPLET, M., SAGAUT, P. & BASDEVANT, C. (2003). Intermodal energy transfers in a proper orthogonal decomposition – Galerkin representation of a turbulent separated flow. *J. Fluid Mech.*, **491**, 275–284.
- DETEMPLE-LAAKE, E. & ECKELMANN, H. (1989). Phenomenology of Kármán vortex streets in oscillatory flow. *Exps. Fluids*, **7**, 217–227.
- DUŠEK, J., GAL, P.L. & FRAUNIÉ, P. (1994). A numerical and theoretical study of the first hopf bifurcation in a cylinder wake. *J. Fluid Mech.*, **264**, 59–80.
- FIEDLER, H.E. & FERNHOLZ, H.H. (1990). A numerical and theoretical study of the first hopf bifurcation in a cylinder wake. *Prog. Aeron. Sc.*, **27**, 305387.
- FLETCHER, C.A.J. (1984). *Computational Galerkin Methods*. Springer.
- GAD-EL-HAK, M. (2000). *Flow Control: Passive, Active and Reactive Flow Management*. Cambridge University Press.



## REFERENCES

---

- GALLETTI, G., BRUNEAU, C.H., ZANNETTI, L. & IOLLO, A. (2004). Low-order modelling of laminar flow regimes past a confined square cylinder. *J. Fluid Mech.*, **503**, 161–170.
- GALMARINI, S. & THUNIS, P. (1999). On the validity of reynolds assumptions for running-mean filters in the absence of a spectral gap. *J. Atm. Sc.*, **56**, 1785–1796.
- GERHARD, J., PASTOOR, M., KING, R., NOACK, B.R., DILLMANN, A., MORZYŃSKI, M. & TADMOR, G. (2003). Model-based control of vortex shedding using low-dimensional Galerkin models. *AIAA Paper* 2003-4262.
- GORDEYEV, S. & THOMAS, F.O. (2010). A temporal proper orthogonal decomposition (tpod) method for closed-loop flow control. *AIAA Paper* 2010-0359.
- GRAHAM, W.R., PERAIRE, J. & TANG, K.Y. (1999). Optimal control of vortex shedding using low-order models. Part I: Open-loop model development. *Int. J. Num. Meth. Eng.*, **44**, 945–972.
- GREENBLATT, D. & WYGNANSKI, I. (2000). The control of flow separation by periodic excitation. *Prog. Aerosp. Sc.*, **36**, 487–545.
- GÜNTHER, B., THIELE, F., PETZ, R., NITSCHKE, W., SAHNER, J., WEINKAUF, T. & HEGE, H.C. (2007). Control of separation on the flap of a three element high-lift configuration. *AIAA Paper* 2007-0265.
- HAKEN, H. (1983). *Synergetics, An Introduction. Nonequilibrium Phase Transitions and Self-Organizations in Physics, Chemistry, and Biology*. Springer, New York, 3rd edn.
- HENNING, L., PASTOOR, M., KING, R., NOACK, B.R. & TADMOR, G. (2007). Feedback control applied to bluff body wake. In R. King, ed., *Active Flow Control*, vol. 95 of *Notes on Numerical Fluid Mechanics and Multidisciplinary Design*, Springer.
- HENNING, L. (2008). *Regelung abgelöster Scherschichten durch aktive Beeinflussung*. Ph.D. thesis, Technische Universität Berlin.

## REFERENCES

---

- HOLMES, P., LUMLEY, J.L. & BERKOOZ, G.D. (1998). *Turbulence, Coherent Structures, Dynamical Systems and Symmetry*. Cambridge University Press.
- HUCHO, W.H. (2002). *Aerodynamik der stumpfen Körper*. Vieweg.
- HUERRE, P. & MONKETWITZ, P.A. (1990). Local and global instabilities in spatially developing flows. *Annual Rev. Fluid Mech.*, **22**, 473–537.
- ILAK, M. & ROWLEY, C.W. (2008). Feedback control of transitional channel flow using balanced proper orthogonal decomposition. *AIAA Paper* 2008-4230.
- JØRGENSEN, B.H., SØRENSEN, J.N. & BRØNS, M. (2003). Low-dimensional modeling of a driven cavity flow with two free parameters. *Theoret. Comput. Fluid Dynamics*, **16**, 299–317.
- KASNAKOGLU, C. (2007). *Reduced order modeling, nonlinear analysis and control methods for flow control problems*. Ph.D. thesis, The Ohio State University.
- KHIBNIK, A.I., NARAYANAN, S., JACOBSON, C.A. & LUST, K. (2000). Analysis of low dimensional dynamics of flow separation. In *Continuation Methods in Fluid Dynamics. Notes on Numerical Fluid Mechanics*, vol. 74, 167–178, Vieweg.
- KING, R. (2007). *Active Flow Control*, vol. 95 of *Notes on Numerical Fluid Mechanics and Multidisciplinary Design*. Springer.
- KRYLOFF, N. & BOGOLIUBOFF, N. (1943). *Introduction to Non-Linear Mechanics*. Princeton University Press.
- LEE, K.H., CORTELEZZI, L., KIM, J. & SPEYER, J. (2001). Application of reduced-order controller to turbulent flows for drag reduction. *Phys. Fluids*, **13**, 1321–1330.
- LEHMANN, O., LUCHTENBURG, D.M., NOACK, B.R., KING, R., MORZYŃSKI, M. & TADMOR, G. (2005). Wake stabilization using pod galerkin models with interpolated modes. In *44th IEEE Conference on Decision and Control and European Control Conference ECC*, invited Paper MoA15.2.

- LIM, K.B. (1992). Method for optimal actuator and sensor placement for large flexible structures. *J. Guidance, Cont. & Dyn.*, **15**, 49–57.
- LU, F.K. (2009). *Fundamentals and Applications of Modern Flow Control*, vol. 231 of *Progress in Astronautics and Aeronautics*. American Institute of Aeronautics and Astronautics, Inc.
- LUCHTENBURG, D.M., TADMOR, G., LEHMANN, O., NOACK, B.R., KING, R. & MORZYŃSKI, M. (2006). Tuned POD Galerkin models for transient feedback regulation of the cylinder wake. *AIAA Paper* 2006-1407.
- LUCHTENBURG, D.M., GÜNTHER, B., NOACK, B.R., KING, R. & TADMOR, G. (2009a). A generalized mean-field model of the natural and high-frequency actuated flow around a high-lift configuration. *J. Fluid Mech.*, **623**, 283–316.
- LUCHTENBURG, D.M., NOACK, B.R. & SCHLEGEL, M. (2009b). An introduction to the POD Galerkin method for fluid flows with analytical examples and MATLAB source codes. Tech. Rep. 01/2009, Berlin Institute of Technology, Department for Fluid Dynamics and Engineering Acoustics, Chair in Reduced-Order Modelling for Flow Control.
- LUCHTENBURG, D.M., ALEKSIĆ, K., SCHLEGEL, M., NOACK, B.R., KING, R., TADMOR, G., GÜNTHER, B. & THIELE, F. (2010). Turbulence control based on reduced-order models and nonlinear control design. In R. King, ed., *Active Flow Control II*, Notes on Numerical Fluid Mechanics and Multidisciplinary Design, Springer, to appear in.
- LUMLEY, J. (1998). The structure of inhomogeneous turbulent flows. In A.M. Yaglom & V.I. Tatarski, eds., *Atmospheric Turbulence & Wave Propagation*, 166–178, Cambridge University Press.
- MAUREL, A., PAGNEUX, V. & WESFREID, J.E. (1995). Mean-flow correction as a non-linear saturation mechanism. *Europhysics Lett.*, **32**, 217–222.
- MERCKER, E. (1980). *Eine Blockierungskorrektur für aerodynamische Messungen in offenen und geschlossenen Unterschallwindkanälen*. Ph.D. thesis, Technische Universität Berlin.

## REFERENCES

---

- MONIN, A.S. & YAGLOM, A.M. (2007). *Statistical Fluid Mechanics, Volume I: Mechanics of Turbulence*. Dover Publications.
- MORZYŃSKI, M. (1987). Numerical solution of navier-stokes equations by the finite element method. In *In Proceedings of SYMKOM 87, Compressor and Turbine Stage Flow Path - Theory and Experiment*, 119–128.
- NAYFEH, A.H. (1973). *Perturbation methods*. John Wiley & Sons.
- NOACK, B.R. & COPELAND, G.S. (2000). On a stability property of ensemble-averaged flow. Tech. Rep. 03/2000, Institute of Fluid Dynamics and Technical Acoustics, Berlin University of Technology.
- NOACK, B.R., AFANASIEV, K., MORZYŃSKI, M., TADMOR, G. & THIELE, F. (2003). A hierarchy of low-dimensional models for the transient and post-transient cylinder wake. *J. Fluid Mech.*, **497**, 335–363.
- NOACK, B.R., TADMOR, G. & MORZYŃSKI, M. (2004). Low-dimensional models for feedback flow control. part i: Empirical galerkin models. In *2nd AIAA Flow Control Conference*, Portland, Oregon, U.S.A., June 28 – July 1, 2004, *AIAA Paper* 2004-2408 (invited contribution).
- NOACK, B.R., PAPAS, P. & MONKEWITZ, P.A. (2005). The need for a pressure-term representation in empirical Galerkin models of incompressible shear flows. *J. Fluid Mech.*, **523**, 339–365.
- NOACK, B.R. (2006). Niederdimensionale Galerkin-Modelle für laminare und transitionelle freie Scherströmungen (transl.: low-dimensional Galerkin models of laminar and transitional free shear flows). Tech. rep., Habilitation thesis, Berlin Institute of Technology, Germany.
- NOACK, B.R., SCHLEGEL, M., AHLBORN, B., MUTSCHKE, G., MORZYŃSKI, M., COMTE, P. & TADMOR, G. (2008). A finite-time thermodynamics of unsteady fluid flows. *J. Non-Equilib. Thermodyn.*, **33**, 103–148.
- PARK, H., LEE, D., JEON, W.P., HAHN, S., KIM, J., CHOI, J. & CHOI, H. (2006). Drag reduction in flow over a two-dimensional bluff body with a blunt trailing edge using a new passive device. *J. Fluid Mech.*, **563**, 389–414.

## REFERENCES

---

- PASTOOR, M., NOACK, B.R., KING, R. & TADMOR, G. (2006). Spatiotemporal waveform observers and feedback in shear layer control. *AIAA Paper* 2006-1402.
- PASTOOR, M., HENNING, L., NOACK, B.R., KING, R. & TADMOR, G. (2008). Feedback shear layer control for bluff body drag reduction. *J. Fluid Mech.*, **608**, 161–196.
- RAJU, R. & MITTAL, R. (2002). Towards physics based strategies for separation control over an airfoil using synthetic jets. *AIAA Paper* 2007-1421.
- REMPFER, D. & FASEL, F.H. (1994). Dynamics of three-dimensional coherent structures in a flat-plate boundary-layer. *J. Fluid Mech.*, **275**, 257–283.
- REYNOLDS, O. (1895). On the dynamical theory of incompressible viscous fluids and the determination of the criterion. *Phil. Trans. A*, **186**, 123–164.
- REYNOLDS, W.C. & HUSSAIN, A.K.M.F. (1972). The mechanics of an organized wave in turbulent shear flow. Part 3. Theoretical model and comparisons with experiments. *J. Fluid Mech.*, **54**, 263–288.
- ROUSSOPOULOS, K. (1993). Feedback control of vortex shedding at low Reynolds numbers. *J. Fluid Mech.*, **248**, 267–296.
- ROWLEY, C.W. (2002). *Modeling, Simulation, and Control of Cavity Flow Oscillations*. Ph.D. thesis, California Institute of Technology.
- ROWLEY, C.W., COLONIUS, T. & MURRAY, R.M. (2003). Model reduction for compressible flows using pod and galerkin projection. *Physica D*, **189**, 115–129.
- ROWLEY, C.W. & JUTTIJUDATA, V. (2005). Model-based control and estimation of cavity flow oscillations. In *Proc. The 44th IEEE Conference on Decision and Control and European Control Conference*, 512–517.
- ROWLEY, C.W. (2005). Model reduction for fluids using balanced proper orthogonal decomposition. *Int. J. Bifurcation and Chaos*, **15**, 997–1013.

## REFERENCES

---

- ROWLEY, C.W. & BATTEN, B.A. (2009). Dynamics and closed-loop control. In R.D. Joslin & D.N. Miller, eds., *Fundamentals and Applications of Modern Flow Control*, vol. 231, Chapter 5, AIAA.
- ROWLEY, C.W., MEZIĆ, I., BAGHERI, S., SCHLATTER, P. & HENNINGSON, D.S. (2009). Spectral analysis of nonlinear flows. *J. Fluid Mech.*, **641**, 115–127.
- RUNG, T. & THIELE, F. (1996). Computational modelling of complex boundary layer flows. In *Proc. The 9th International Symposium on Transport Phenomena in Thermal-Fluids Engineering*, 321–326.
- SAMIMY, M., DEBIASI, M., CARABALLO, E., SERRANI, A., YUAN, X., LITTLE, J. & MYATT, J. (2007). Feedback control of subsonic cavity flows using reduced-order models. *J. Fluid Mech.*, **579**, 315–346.
- SCHATZ, M., GÜNTHER, B. & THIELE, F. (2006). Computational investigation of separation control over high-lift airfoil flows. In R. King, ed., *Active Flow Control*, vol. 95 of *Notes on Numerical Fluid Mechanics and Multidisciplinary Design*, 260–278, Springer.
- SCHLEGEL, M., LEHMANN, O., DILLMANN, A., NOACK, B.R., GRÖSCHEL, E., SCHRÖDER, W., WEI, M., FREUND, J.B. & JORDAN, P. (2010). On least-order flow representations for aerodynamics and aeroacoustics. *J. Fluid Mech.*, submitted.
- SEIFERT, A., DARABI, A. & WYGNANSKI, I. (1996). On the delay of airfoil stall by periodic excitation. *J. Aircraft*, **33**, 691–699.
- SIEGEL, S., COHEN, K. & McLAUGHLIN, T. (2003). Feedback control of a circular cylinder wake in experiment and simulation. *AIAA Paper* 2003-3569.
- SIEGEL, S.G., SEIDEL, J., CASEY, C., LUCHTENBURG, D.M., COHEN, K. & McLAUGHLIN, T. (2008). Low-dimensional modelling of a transient cylinder wake using double proper orthogonal decomposition. *J. Fluid Mech.*, **610**, 1–42.

## REFERENCES

---

- SIPP, D. & LEBEDEV, A. (2007). Global stability of base and mean flows: a general approach and its applications to cylinder and open cavity flows. *J. Fluid Mech.*, **593**, 333–358.
- SIROVICH, L. (1987). Turbulence and the dynamics of coherent structures. part 1 : Coherent structures. *Quarterly of Applied Mathematics*, **45**, 561–571.
- SLOTINE, J. & LI, W. (1991). *Applied nonlinear control*. Pearson Prentice Hall, 1st edn.
- STRANG, G. (1988). *Linear Algebra and Its Applications*. Brooks Cole.
- STROGATZ, S.H. (1994). *NonLinear dynamics and chaos*. Addison Wesley Publishing Company.
- STRYKOWSKI, P.J. & SREENIVASAN, K.R. (1990). On the formation and suppression of vortex ‘shedding’ at low Reynolds numbers. *J. Fluid Mech.*, **218**, 71–107.
- STUART, J.T. (1958). On the non-linear mechanics of hydrodynamic stability. *J. Fluid Mech.*, **4**, 1–21.
- TADMOR, G., NOACK, B., DILLMANN, A., GERHARD, J., PASTOOR, M., KING, R., & MORZYŃSKI, M. (2003). Control, observation and energy regulation of wake flow instabilities. In *42nd IEEE Conference on Decision and Control*, 23342339.
- TADMOR, G., NOACK, B.R., MORZYŃSKI, M. & SIEGEL, S. (2004). Low-dimensional models for feedback flow control. Part II: Controller design and dynamic estimation. *AIAA Paper* 2004-2409.
- TADMOR, G. (2004). Observers and feedback control for a rotating vortex pair. In *IEEE transactions on control systems technology*, vol. 12, 3651.
- TAYLOR, J.A. & GLAUSER, M.N. (2004). Towards practical flow sensing and control via pod and lse based low-dimensional tools. *J. Fluids Eng.*, **126**, 337–345.

## REFERENCES

---

- UKEILEY, L., CORDIER, L., MANCEAU, R., DELVILLE, J., BONNET, J. & GLAUSER, M. (2001). Examination of large-scale structures in a turbulent plane mixing layer. Part 2. Dynamical systems model. *J. Fluid Mech.*, **441**, 61–108.
- UNAL, M.F. & ROCKWELL, D. (1987). On the vortex formation from a cylinder; Part 2: Control by a splitter-plate interference. *J. Fluid Mech.*, **190**, 513–529.
- VISWANATH, P.R. (1996). Flow management techniques for base and afterbody drag reduction. *Prog. Aerospace Sc.*, **32**, 79–129.
- WESSELING, P. (2000). *Principles of computational fluid dynamics*. Springer.
- WILCOX, D.C. (1994). *Turbulence modeling for CFD*. Dcw Industries, Incorporated.
- WU, C.G., LIANG, Y.C., LIN, W.Z., LEE, H.P. & LIM, S.P. (2003). A note on equivalence of proper orthogonal decomposition methods. *J. Sound Vibr.*, **265**, 1103–1110.